

A PHYSICS BASED TIME-FREQUENCY ANALYSIS TO
REDUCE MULTI-BOUNCE AND CLUTTER IN
RADAR IMAGING

by

ANIL KUMAR KOLLIPARA

Presented to the Faculty of the Graduate School of
The University of Texas at Arlington in Partial Fulfillment
of the Requirements
for the Degree of

MASTER OF SCIENCE IN ELECTRICAL ENGINEERING

THE UNIVERSITY OF TEXAS AT ARLINGTON

August 2005

ACKNOWLEDGEMENTS

I would like to express my appreciation and sincere gratitude to Dr. Saibun Tjuatja who has been my mentor, advisor and a guide throughout the duration of this research work. His guidance, encouragement, work ethics, support and patience has helped me to great extent not only in my research but also in my personal life. It has been a great pleasure working with him.

I would like to thank Dr. Jonathan Bredow for his technical guidance, help with my experiments and his valuable comments which have definitely improved the quality of this thesis. I would also like to thank Dr. Soontorn Oraintara for his excellent teaching which has helped me to better understand many signal processing concepts. I wish to sincerely thank Dr. Vasant Prabhu for his valuable suggestions, encouragement and support.

In addition, a special thanks to Suman Kumar Gunnala for his assistance in carrying out some of my imaging experiments. Finally, I would like to thank my father, my mother, my sisters and my friends whose love, encouragement, belief and understanding has helped me a great deal in this thesis study.

May 6, 2005

ABSTRACT

A PHYSICS BASED TIME-FREQUENCY ANALYSIS TO REDUCE MULTI-BOUNCE AND CLUTTER IN RADAR IMAGING

Publication No. _____

Anil Kumar Kollipara, M.S.

The University of Texas at Arlington, 2005

Supervising Professor: Saibun Tjuatja

The concept of time-frequency analysis of the scattered far field data from multiple targets is presented. The scattered data from the target is collected using a mono-static antenna configuration. The hardware system and the data acquisition system used in the process are discussed in detail. The results obtained using the ISAR imaging algorithm are presented and the effect of different non-point and dispersive scattering phenomena on these images are discussed. A physics based time-frequency analysis using wavelets is done on this scattered data to reduce the inter-target interactions and thereby produce cleaner images of the target under consideration. The

results obtained after time-frequency analysis are presented. The effects of different kinds of wavelets and their support length on different targets are discussed.

TABLE OF CONTENTS

ACKNOWLEDGEMENTS.....	ii
ABSTRACT	iii
LIST OF ILLUSTRATIONS.....	viii
LIST OF TABLES.....	xiii
Chapter	
1. INTRODUCTION.....	1
2. RADAR SIGNAL PROCESSING AND IMAGING.....	3
2.1 ISAR Imaging.....	3
2.1.1 The Physical Optics Approximation.....	4
2.1.2 Different Scattering Mechanisms in Radar Imaging	8
2.2 The Concept of Wavelets	8
2.2.1 Rationale for the use of Wavelets in Signal Processing	9
2.2.2 Short-Time Fourier Transform vs Wavelet Transform	10
2.3 Time-Frequency Analysis in Radar Imaging	16
3. LABORATORY EXPERIMENT DESCRIPTION.....	18
3.1 Measurement System.....	18
3.2 Data Acquisition	20
3.2.1 Hardware Description.....	21
3.2.2 Software Description	21

3.3 Experimental Setup.....	23
3.3.1 Setup 1	24
3.3.2 Setup 2	25
3.3.3 Setup 3	27
3.4 Data Analysis.....	28
3.4.1 Back Ground Subtraction	28
3.4.2 Calibration Routines	29
3.4.3 Time Gating.....	33
4. ISAR IMAGING ALGORITHM AND TIME-FREQUENCY ANALYSIS.....	36
4.1 ISAR Imaging Algorithm and Implementation	36
4.1.1 ISAR Imaging Algorithm	36
4.2 Time-Frequency Analysis using Wavelets	41
4.2.1 Wavelet Implementation in Frequency Domain.....	41
4.2.2 Wavelet Implementation Algorithm.....	49
5. RESULTS AND DISCUSSIONS.....	69
5.1 Effect of Wavelet Support Size	69
5.1.1 Results for Test Set 1	70
5.2 Effect of Wavelet Type.....	78
5.3 Analysis of Other Complex Targets	80
6. CONCLUSIONS	90

Appendix

A. MATLAB PROGRAM FOR WAVELET PROCESSING	94
B. MATHEMATICA PROGRAM FOR ISAR IMAGING	100
REFERENCES	104
BIOGRAPHICAL INFORMATION.....	107

LIST OF ILLUSTRATIONS

Figure	Page
2.1 Scattering Geometry of a Target Under Illumination	3
2.2 Time-Frequency Tiling for Short-Time Fourier Transform (a) and Wavelet Transform (b)	12
2.3 Frequency Division: Uniform for Short-Time Fourier Transform (a) and Logarithmic for Wavelet Transform (b).....	16
3.1 Illustration of a Mono-Static Setup used.....	20
3.2 NI GPIB USB-B Connector used for Data Acquisition.....	21
3.3 Snap Shot of the Data Acquisition Software Program.....	23
3.4 Setup 1: A 6 inch and a 3 inch Sphere Used for Imaging	25
3.5 Setup 2: A 3 inch and a 4 inch Sphere Used for Imaging	26
3.6 Setup 3: Three Copper Rods Forming a Triangle Shape before and after Burying in Sand.....	27
3.7 Magnitude Response Comparison between Raw Data and Corrected Data (Background Subtracted Data) for 0 degrees	29
3.8 Calibrated Time-Domain Magnitude Response for 0 degrees	31
3.9 Calibrated Time-Domain Magnitude Response for 205 degrees	32
3.10 Calibrated Time-Domain Magnitude Response for 90 degrees	33
3.11 Flow Chart for Back Ground Subtraction, Calibration and Time Gating.....	35
4.1 Flow Chart for ISAR Imaging.....	38
4.2 Interpolation Process	39

4.3	Generated ISAR Image of Test Set 1(3 and 6 inch spheres).....	39
4.4	Generated ISAR Image of Test Set 2(3 and 4 inch spheres).....	40
4.5	Wavelet Filter Bank	42
4.6	Outputs of a 3-Stage 2 Channel Filter Bank	42
4.7	Frequency Band Split of a 3-Stage 2 Channel Filter Bank	43
4.8	Time-Frequency Diagram of a Wavelet Filter Bank.....	45
4.9	Wavelet Implementation in Frequency Domain	46
4.10	Time-Frequency Representation of Radar Returns for Setup 2 for an Azimuth of 0 degrees Using STFT	48
4.11	Wavelet Implementation Algorithm.....	49
4.12	A Signal in Time Domain	50
4.13	Frequency Response of the Time-Domain Signal.....	51
4.14	Time-Domain Signal obtained by Considering Resolution 1 (H) of the Frequency Domain Signal.....	52
4.15	Time-Domain Signal obtained by Considering Resolution 2 (LH) of the Frequency Domain Signal.....	52
4.16	Time-Domain Signal obtained by Considering Resolution 3 (LLH) of the Frequency Domain Signal.....	53
4.17	Time-Domain Signal obtained by Considering Resolution 4 (LLL) of the Frequency Domain Signal.....	53
4.18	Time-Domain Response (azimuth of 0 degrees) for Test Set 1 after Considering Lower Resolutions (7-9) of Frequency Domain Data using db2.....	55
4.19	Time-Domain Response (azimuth of 50 degrees) for Test Set 1 after Considering Lower Resolutions (7-9) of Frequency Domain Data using db2.....	55

4.20 Time-Domain Response (azimuth of 0 degrees) for Test Set 1 after Considering Higher Resolutions (1-6) of Frequency Domain Data using db2.....	56
4.21 Time-Domain Response (azimuth of 50 degrees) for Test Set 1 after Considering Higher Resolutions (1-6) of Frequency Domain Data using db2.....	56
4.22 Generated ISAR Image of Test Set 1 after Selecting Resolutions (1-6) of the Frequency Domain Data	58
4.23 Generated ISAR Image of Test Set 1 after Selecting Resolutions (7-9) of the Frequency Domain Data	59
4.24 Time-Domain Response (azimuth of 50 degrees) for Test Set 2 after Considering Lower Resolutions (7-8) of Frequency Domain Data using db2.....	61
4.25 Time-Domain Response (azimuth of 70 degrees) for Test Set 2 after Considering Lower Resolutions (7-8) of Frequency Domain Data using db2.....	61
4.26 Time-Domain Response (azimuth of 50 degrees) for Test Set 2 after Considering Higher Resolutions (1-6) of Frequency Domain Data using db2.....	62
4.27 Time-Domain Response (azimuth of 70 degrees) for Test Set 2 after Considering Higher Resolutions (1-6) of Frequency Domain Data using db2.....	62
4.28 Time-Domain Response (azimuth of 50 degrees) for Test Set 2 after Considering Lowest Resolution (9) of Frequency Domain Data using db2.....	63
4.29 Time-Domain Response (azimuth of 70 degrees) for Test Set 2 after Considering Lowest Resolution (9) of Frequency Domain Data using db2.....	63
4.30 Generated ISAR Image of Test Set 2 after Selecting Resolutions (1-6) of the Frequency Domain Data	64
4.31 Generated ISAR Image of Test Set 2 after Selecting Resolutions (7-8) of the Frequency Domain Data	65

4.32	Generated ISAR Image of Test Set 2 after Selecting the Lowest Resolution (9) of the Frequency Domain Data	66
4.33	A Summary of Multi-Resolution Analysis for Test Set 1	67
4.34	A Summary of Multi-Resolution Analysis for Test Set 2	68
5.1	Time-Domain Response Comparison using db1	70
5.2	Time-Domain Response Comparison using db3	71
5.3	Time-Domain Response Comparison using db6	72
5.4	Time-Domain Response Comparison of different Wavelet Support Lengths for Daubechies Wavelets	73
5.5	Time-Domain Response Comparison using Coif 1	74
5.6	Time-Domain Response Comparison using Coif 2	75
5.7	Time-Domain response comparison of different Wavelet Support Lengths for Coiflets	76
5.8	Variation of Side Lobe Suppression (SP) as a Function of Filter Length	78
5.9	Comparison of Time-Domain Response of Daubechies (db3) and Coiflets (Coif 1)	79
5.10	Comparison of Time-Domain Response of Daubechies (db6) and Coiflets (Coif 2)	80
5.11	Range Profile (Time-Domain response) of Target in Setup 3 for an Azimuth of 50 degrees	81
5.12	Generated ISAR Image of the Buried Target in Test Set 3 (3 rods arranged as triangle)	82
5.13	Time-Domain Response (azimuth of 50 degrees) for Test Set 3 after Considering Higher Resolutions (1-6) of Frequency Domain Data using db12	84
5.14	Generated ISAR Image of the Buried Target in Test Set 3 after Considering Considering Resolutions 1-6 of the	

Frequency Domain Data (using db12)	85
5.15 Time-Domain Response (azimuth of 50 degrees) for Test Set 3 after Considering Lower Resolutions(7-9) of Frequency Domain Data using db12.....	86
5.16 Generated ISAR Image of the Buried Target in Test Set 3 after Considering Resolutions 7-9 of the Frequency Domain Data (using db12)	87
5.17 Time-Domain Response (azimuth of 50 degrees) for Test Set 3 after Considering Lower Resolutions(8-9) of Frequency Domain Data using db12.....	88
5.18 Time-Domain Response (azimuth of 50 degrees) for Test Set 3 after Considering Resolution 7 of Frequency Domain Data using db12.....	88
5.19 Generated ISAR Image of the Buried Target in Test Set 3 after Considering Resolution 7 of Frequency Domain Data (using db12)	89

LIST OF TABLES

Table	Page
3.1 Hardware and Test Equipment Used in Mono-Static Measurements	19
3.2 Test Parameters Used for Setup 1	24
3.3 Test Parameters Used for Setup 2	26
3.4 Test Parameters Used for Setup 3	27
4.1 Relation between Resolution and Time Gate width (for 2048 length data)	47
5.1 Side Lobe Suppression (SP) Variation with Filter Length.....	77

CHAPTER 1

INTRODUCTION

Inverse synthetic aperture radar (ISAR) imaging is being used in many fields like remote sensing, medical imaging, etc. The main objective of ISAR imaging is to obtain specific properties of the target like shape, orientation, speed, scattering properties and so on. It is well known in the radar imaging community that ISAR imaging algorithm does not account for certain inter target interactions. It is very important to understand the physics behind the phenomena of backscattering from multiple targets, inter-target interactions.

The focus of this thesis is to understand the physics behind the phenomena of electromagnetic scattering from multiple targets. Time Frequency analysis of the backscattered data can provide an insight to these different interactions. We discuss the time-frequency phenomena and multi-resolution by using wavelets. We explore the meaning of multi-resolution of the frequency domain data and its relation to the arrival time of the backscattered signal. An experimental approach is used to prove the hypothesis of separating different interactions in time.

Chapter 2 gives an introduction to ISAR imaging and wavelets. Chapter 3 gives a detailed description of the experimental procedure and the hardware and software systems used to carry out the imaging experiments. Different test sets used to support the hypothesis are discussed. A detailed analysis of the data or signal is done in the

following sections. These different sections describe the process of obtaining the backscattered signal, performing background subtraction and calibration to increase the signal quality of the obtained data. ISAR imaging algorithm is explained in the next subsection. Finally chapter 3 ends with results obtained from the ISAR imaging algorithm. These generated images show the effects of inter-target interactions like multi bounce effect and other non-point scattering features.

In chapter 4, we introduce the approach of separating different interactions by time-frequency analysis using multi-resolution applied to the frequency domain data. This approach combines the ISAR processing with joint time-frequency signal representation. The results obtained after this approach are presented. These images are compared to those obtained in chapter 3 to support the hypothesis. The results show that the phenomena of multi-bounce and non-point scatterings can be separated from the original ISAR images and cleaner images can be obtained. Chapter 5 discusses the results obtained for various cases and the effect of different parameters like wavelet type, its support size, on the images obtained for the test cases mentioned in chapter 3.

CHAPTER 2

RADAR SIGNAL PROCESSING AND IMAGING

2.1 ISAR Imaging

The main purpose of this chapter is to introduce the concept of ISAR imaging and its applications. ISAR imaging has been widely used for imaging purposes.

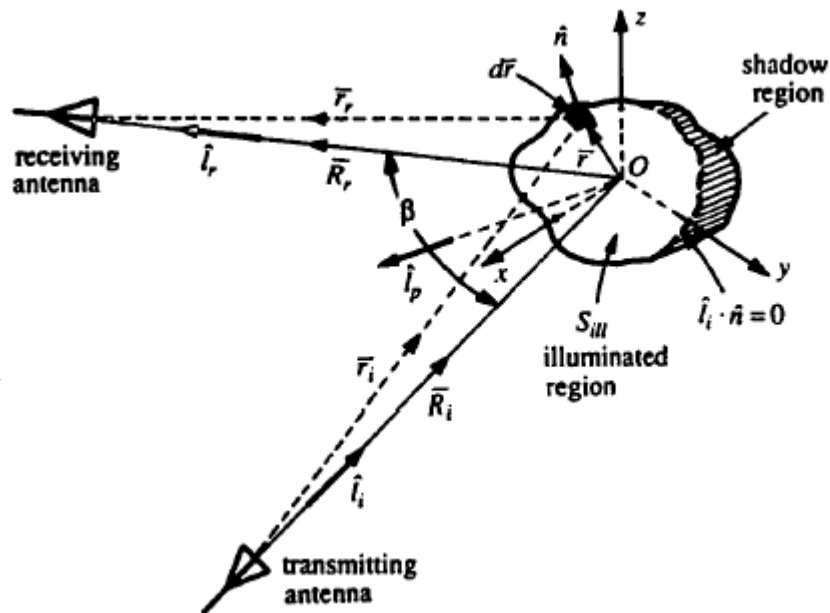


Figure 2.1 Scattering Geometry of a Target Under Illumination (source: [7])

Figure 2.1 shows an object or target illuminated by an electromagnetic field from a transmitter antenna. The receiver antenna observes the scattered electromagnetic field. The total electric and magnetic fields on the closed surface of the target can be expressed using Stratton-Chu integral equations [1][2]:

$$\overline{E}^s(\overline{R}_r) = \frac{1}{4\pi} \int_s [(\hat{n} \times \overline{E}^l) \times \nabla \psi_o - j\omega\mu(\hat{n} \times \overline{H}^l)\psi_o + (\hat{n} \times \overline{E}^l) \nabla \psi_o] ds \quad (2.1)$$

$$\overline{H}^s(\overline{R}_r) = \frac{1}{4\pi} \int_s [(\hat{n} \times \overline{H}^l) \times \nabla \psi_o - j\omega\varepsilon(\hat{n} \times \overline{E}^l)\psi_o + (\hat{n} \times \overline{H}^l) \nabla \psi_o] ds \quad (2.2)$$

In the above equations S is the closed surface encompassing the object under consideration and \hat{n} is the normal vector whose direction is outward from the object.

Assuming that the object is a perfect conductor, the equations (2.1) and (2.2) can be simplified as $\hat{n} \times \overline{E}^l = 0$ and $\hat{n} \cdot \overline{H}^l = 0$. Thus the above two equations will be reduced to the following:

$$\overline{E}^s(\overline{R}_r) = \frac{1}{4\pi} \int_s [-j\omega\mu(\hat{n} \times \overline{H}^l)\psi_o + (\hat{n} \times \overline{E}^l) \nabla \psi_o] ds \quad (2.3)$$

$$\overline{H}^s(\overline{R}_r) = \frac{1}{4\pi} \int_s [(\hat{n} \times \overline{H}^l) \times \nabla \psi_o] ds \quad (2.4)$$

2.1.1 The Physical Optics Approximation

The physical optics approximation considers three assumptions which simplify equations (2.3) and (2.4). The first assumption is that the total fields on the shadowed side are set to zero and the discontinuity at the boundary of the illuminated side the shadowed side needs to be taken into account to satisfy Maxwell's equations [1]. The second approximation is that the scattering fields are being observed at the far-field region and hence

$$\psi_o \approx \frac{e^{-jkR_r} e^{jk\hat{l}_r \cdot \hat{r}}}{R_r}, \quad (2.5)$$

where ψ_o is called the free space Green's function, \hat{l}_r is the observation direction as shown in Figure 2.1. Approximating the local surface surrounding any point by an infinite plane tangent to that point, Snell's law on perfectly conducting plane can be used,

$$\hat{n} \times \overline{E}^t = 0; \quad \hat{n} \times \overline{H}^t = 2 \hat{n} \times \overline{H}^i \quad (2.6)$$

These assumptions reduce equations (2.3) and (2.4) to

$$\overline{E}^s(\overline{R}_r) = \frac{-j\omega\mu}{2\pi R_r} e^{-jkR_r} \int_{S_{ill}} [(\hat{n} \times \overline{H}^i) - (\hat{l}_r \cdot (\hat{n} \times \overline{H}^i)) \hat{l}_r] e^{jk\hat{l}_r \cdot \overline{r}} ds \quad (2.7)$$

$$\overline{H}^s(\overline{R}_r) = \frac{jk}{2\pi R_r} e^{-jkR_r} \int_{S_{ill}} [(\hat{n} \times \overline{H}^i) \times \hat{l}_r] e^{jk\hat{l}_r \cdot \overline{r}} ds \quad (2.8)$$

The incident field on the surface of the object under consideration can be expressed by a spherical wave as

$$\overline{E}^i = \overline{E} \frac{e^{-jkr_i}}{r_i}; \quad \overline{H}^i = \overline{H} \frac{e^{-jkr_i}}{r_i}, \quad (2.9)$$

Assuming that the object being illuminated is not too large, equation (2.9) can be approximated by a local plane wave, i.e.,

$$\overline{E}^i \approx \overline{E} \frac{e^{-jkR_i} e^{-jk\hat{l}_i \cdot \overline{r}}}{R_i}; \quad \overline{H}^i \approx \overline{H} \frac{e^{-jkR_i} e^{-jk\hat{l}_i \cdot \overline{r}}}{R_i}; \quad (2.10)$$

Substituting (2.10) into (2.7) and (2.8) we obtain

$$\overline{E}^s(\overline{R}_r) = \frac{-j\omega\mu}{2\pi R_r R_i} e^{-jk(R_r+R_o)} \int_{S_{ill}} [(\hat{n} \times \overline{H}^i) - (\hat{l}_r \cdot (\hat{n} \times \overline{H}^i)) \hat{l}_r] e^{jk(\hat{l}_r - \hat{l}_i) \cdot \overline{r}} ds \quad (2.11)$$

$$\overline{H^s}(\overline{R}_r) = \frac{-jk}{2\pi R_r R_i} e^{-jk(R_r+R_o)} \int_{Sill} [(\hat{n} \times \overline{H}) \cdot \hat{i}_r] e^{jk(l_r - \hat{l}_i)} ds \quad (2.12)$$

Using the Lorentz condition, the vector potential \overline{A} can be expressed in terms of the surface current, i.e.,

$$\overline{A}(\overline{R}_r) = \frac{\mu}{4\pi} \int_V \overline{J}(\overline{r}) \psi_o dv, \quad (2.13)$$

where V is the volume enclosing the current source. Since it is known that the currents exist only on the object surface, the volume integral can be regarded as surface integral.

The magnetic field can be obtained as

$$\overline{H} = \frac{1}{\mu} \nabla \times \overline{A}, \quad (2.14)$$

and the surface current \overline{J} is expressed by

$$\overline{J} = 2 \hat{n} \times \overline{H}^i, \quad (2.15)$$

Now in addition to equation (2.15), the total surface current consists of a corrective current which accounts for the influence of currents induced at other points and can be expressed by an integral in terms of the total current [4,5,7]. This means that by neglecting the corrective current, the influence of currents from other points are ignored. Thus these currents which may be due to multiple scatterings and creeping waves are ignored.

Considering the above mentioned approximations and considering mono-static case, equation (2.12) can be reduced to

$$\overline{H^s}(\overline{R}_r) = \frac{-j}{2\pi R_r R_i} e^{-jk(R_r+R_i)} \int_{Sill} \overline{H}(\overline{k} \cdot \hat{n}) e^{j2\overline{k} \cdot \overline{r}} ds \quad (2.16)$$

Considering the amplitude of the fields the scattering amplitude can be represented as

$$\begin{aligned}\Gamma_1(\bar{k}) &= 2\pi R_r R_i e^{jk(R_r+R_i)} \frac{H^S}{H} \\ &= j \int_{S_1} e^{j2\bar{k}\cdot\bar{r}} \bar{k} \cdot d\bar{s},\end{aligned}\quad (2.17)$$

Also by using Gauss's divergence theorem, it can be shown [7] that

$$\begin{aligned}\Gamma_1(\bar{k}) + \Gamma_2^*(-\bar{k}) &= j \int_{S_1+S_2} e^{j\bar{k}\cdot\bar{r}} \bar{k} \cdot d\bar{s} \\ &= j \int_S e^{j2\bar{k}\cdot\bar{r}} \bar{k} \cdot d\bar{s} = j \int_V \nabla \cdot (e^{j2\bar{k}\cdot\bar{r}} \bar{k}) dv,\end{aligned}\quad (2.18)$$

Carrying out the divergence operation in (2.18),

$$\frac{-[\Gamma_1(\bar{k}) + \Gamma_2^*(-\bar{k})]}{2k^2} = \int_V e^{j2\bar{k}\cdot\bar{r}} dv. \quad (2.19)$$

We can write

$$\Gamma(\bar{p}) = \int_{-\infty}^{\infty} \gamma(\bar{r}) e^{j\bar{p}\cdot\bar{r}} d\bar{r}, \quad (2.20)$$

where Γ is the right hand side of (2.19), $\bar{p} = 2\bar{k}$ and γ is the characteristic function of the scatterers which describe the target geometrical shape. The well known Bojarski's identity [6] is the Fourier inversion of Γ to obtain γ as

$$\gamma(\bar{r}) = \frac{1}{(2\pi)^3} \int_{-\infty}^{\infty} \Gamma(\bar{p}) e^{-j\bar{p}\cdot\bar{r}} d\bar{p} \quad (2.21)$$

The above equation gives the relation between the scattered electromagnetic field and the object geometry which is the basis of ISAR imaging.

2.1.2 Different Scattering Mechanisms in Radar Imaging

Scattering from targets especially complex targets can be classified into the following types [1,8]:

- 1) Specular scattering points
- 2) Multiple scattering points
- 3) Scattering from discontinuities (edges)
- 4) Scattering from surface derivative discontinuities
- 5) Creeping waves
- 6) Traveling wave scattering

The ISAR imaging algorithm does not account for above mentioned scattering phenomena. Thus, such scattering centers can add unwanted artifacts in the images generated. To obtain better images which are free from the above mentioned scattering phenomena, ISAR imaging algorithm with joint time frequency analysis is used.

2.2 The Concept of Wavelets

Time-frequency representation of non-stationary signals is an issue which has been increasingly discussed in the general signal processing literature. It has become a powerful alternative for the analysis of the non-stationary signals since the classical Fourier transform gives the frequency contents of the signals without providing information about the time localization of the observed frequency components. This

section gives an introduction to some of the methods used to perform time-frequency analysis, their merits and limitations.

2.2.1 Rationale for the use of Wavelets in Signal Processing

Several techniques have been proposed such as Short-Time Fourier Transform (STFT), Wigner-Ville Transform and Wavelet Transform (WT) to obtain time-frequency representation of signals. In STFT (which is also called the windowed Fourier transform or the Gabor transform), the signal is multiplied by a smooth window function (typically Gaussian) and the Fourier integral is applied to the windowed signal. Thus, choosing a short analysis window may cause a poor frequency resolution, while a long analysis window introduces a poor time (space) resolution and a high risk to violate the assumption of stationarity within the window. The Wigner-Ville Transform offers the best simultaneous resolution in time and frequency. However, its main drawback is that it generates some ghost frequencies which do not exist in the analyzed signal. The WT is characterized by a frequency response logarithmically scaled along the frequency axis, as opposed to the STFT, which uses a fixed window in time domain. Thus, it provides a good time resolution at high frequencies and a good frequency resolution at low frequencies, being appropriate to discriminate transient high-frequency components closely located in time and long duration components closely spaced in frequency. Despite the fact that the time-varying spectrum of the non-stationary signals was a starting point for the development of different time-frequency representation techniques, it did not remain a singular objective of wavelet transform based analysis. The joint time-frequency analysis affected by the WT provides also natural settings for

well defined statistical applications, which include estimation, detection, classification, filtering and compression. Consequently, the use of wavelets as a tool for signal processing has rapidly increased in recent years for both 1-D and 2-D signals. The WT is presently applied mainly in two different ways: as a pseudo-continuous transformation (used for spectro-temporal analysis of 1-D medical signals), and as multi-resolution orthogonal signal decomposition (with specific applications in feature extraction, pattern recognition, filtering and compression of both 1-D and 2-D signals). Other important properties of the WT that make it suitable for signal and image processing applications are:

- Multi-resolution - the WT offers a scale invariant representation
- Sparsity - the wavelet coefficients distribution of images is sparse
- Fast algorithms - efficient decomposition and reconstruction algorithms exist for implementing the WT
- Edge detection - small wavelet coefficients correspond to homogenous areas, while large wavelet coefficients correspond to image edges.

2.2.2 Short-Time Fourier Transform vs Wavelet Transform

The Short Time Fourier Transform assumes that the signal $x(t)$ is stationary within a window $g(t)$ of limited extent, centered at time location t . Consequently, it maps the signal $x(t)$ into a two-dimensional function in a time-frequency plane (τ, ω) :

$$STFT(\tau, \omega) = \int_{-\infty}^{+\infty} x(t).g^*(t - \tau).e^{-j\omega t} dt \quad (2.22)$$

The analysis here depends critically on the choice of the window $g(t)$. The resulting time-varying spectrum is displayed as a three-dimensional plot of energy versus time and frequency. Figure 2.2 shows vertical stripes in the time-frequency plane illustrating this “windowing of the signal” view of the STFT. Given a version of the signal windowed around time t , one computes all “frequencies” of the STFT. An alternative view is based on a filter bank interpretation of the same process. At a given frequency ω , the whole signal is filtered using a band-pass filter, which has an impulse response the window function modulated to that frequency (this is shown as the horizontal stripes in figure 2.2). In this way, the STFT may be also seen as a modulated filter bank. From this dual interpretation, a possible drawback related to the time and frequency resolution can be shown. Consider the ability of the STFT to discriminate between two pure sinusoids. Given a window function $g(t)$ and its Fourier transform $G(\omega)$, define the bandwidth $\Delta\omega$ of the filter as:

$$\Delta\omega^2 = \frac{\int \omega^2 |G(\omega)|^2 d\omega}{\int |G(\omega)|^2 d\omega} \quad (2.23)$$

where the denominator is the energy of $g(t)$. Two sinusoids will be discriminated only if they are more than $\Delta\omega$ apart (the resolution in frequency of the STFT analysis is given by $\Delta\omega$).

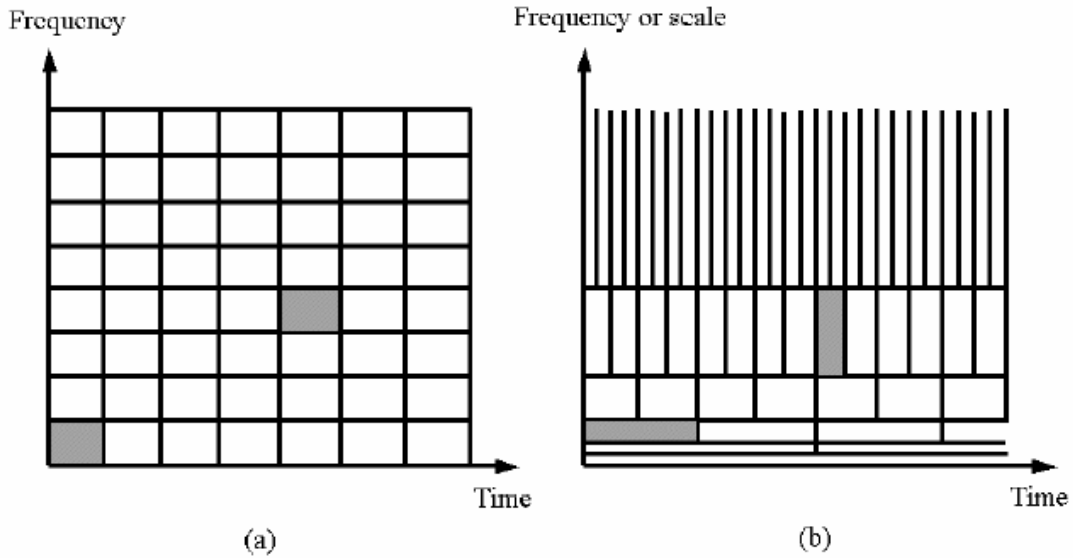


Figure 2.2 Time-Frequency Tiling for Short-Time Fourier Transform (a) and Wavelet Transform (b)

Similarly, the spread in time is given by Δt as:

$$\Delta t^2 = \frac{\int t^2 |g(t)|^2 dt}{\int |g(t)|^2 dt} \quad (2.24)$$

where the denominator is again the energy of $g(t)$. Two pulses in time can be discriminated only if they are more than Δt apart.

The Wavelet Transform provides an interesting and useful alternative to the classical STFT briefly presented before. The basic difference consists on the fact that the WT performs a multi-resolution analysis of the signals, by making use of short windows at high frequencies and long windows at low frequencies. Formally, the definition of the WT is given by:

$$CWT_x(\tau, r) = \frac{1}{\sqrt{r}} \int x(t) h^* \left(\frac{t - \tau}{r} \right) dt \quad (2.25)$$

The analysis is made now in the spirit of constant relative bandwidth. The straightforward interpretation of (2.25) is that as the scale parameter r increases, the filter impulse response becomes spread out in time, and takes only longtime behavior (low frequencies) into consideration (see the lowest horizontal stripes of figure 2.2 (b)). Similarly, when the scale r decreases, only transient features of the signal are seen through the analysis window (see the highest vertical stripes of figure 2.2 (b)). The time resolution becomes arbitrarily good at high frequencies, while the frequency resolution becomes arbitrarily good at low frequencies. Consequently, two very close short bursts can always be separated in the analysis by going up to higher analysis frequencies in order to increase the corresponding time resolution. The resolution in time and frequency cannot be arbitrarily small, because their product is lower bounded as given by the well-known Heisenberg inequality:

$$\Delta\omega\Delta t \geq \frac{1}{2} \quad (2.26)$$

It implies that one can only trade time resolution for frequency resolution or vice versa. To overcome the resolution limitation of the STFT, one can let the resolution $\Delta\omega$ and Δt to vary in the time-frequency plane in order to obtain a multi-resolution analysis. When the analysis is viewed as a filter bank, the time resolution must increase with the central frequency of the analysis filters. By imposing that $\Delta\omega$ is proportional to ω or:

$$\frac{\Delta\omega}{\omega} = c \quad (2.27)$$

where c is a constant, the analysis filter bank is then composed of band-pass filters with constant relative bandwidth. Consequently, instead of the frequency responses of the analysis filter being regularly spaced over the frequency axis (as for the STFT case), they are regularly spread in a logarithmic scale. The time and frequency resolutions still satisfy the Heisenberg inequality, but now the time resolution becomes arbitrarily good at high frequencies, while the frequency resolution becomes arbitrarily good at low frequencies.

The Continuous Wavelet Transform (CWT) exactly follows the above ideas and furthermore, all impulse responses of the filter bank are defined as scaled versions of the same prototype $h(t)$:

$$h_r(t) = \frac{1}{\sqrt{|r|}} h\left(\frac{t}{r}\right) \quad (2.28)$$

where r is a scale factor and the constant $\frac{1}{\sqrt{|r|}}$ is used for energy normalization. Since

the same prototype $h(t)$, called the basic wavelet, is used for all the filter impulse responses, no specific scale is privileged, i.e. the wavelet analysis is self-similar at all scales. For comparison purposes, the basic wavelet $h(t)$ could be chosen as a modulated window:

$$h(t) = g(t).e^{-j\omega_o t} \quad (2.29)$$

Then, the frequency responses of the analysis filters indeed satisfy 2.28 with the identification

$$r = \frac{\omega_o}{\omega}$$

It should be mentioned that the local frequency of $\omega = r\omega_o$, whose definition depends on the basic wavelet, is no longer linked to frequency modulation (as was the case for the STFT) but is now related to time-scaling. The scale is defined as in the geographical maps: since the filter bank impulse responses are dilated as the scale increases, large scales correspond to contracted signals, while small scales correspond to dilated signals in the transform domain. Once a window has been chosen for the STFT, then the time-frequency resolution is fixed over the entire time-frequency plane (since the same window is used at all frequencies) as shown in figure 2.3 (a). Alternatively, in the case of Wavelet Transform, $\Delta\omega$ and Δt change with the center frequency of the analysis filter. They still satisfy the Heisenberg inequality, but now, the time resolution becomes arbitrarily good at high frequencies, while the frequency resolution becomes arbitrarily good at low frequencies as shown in figure 2.2 (b).

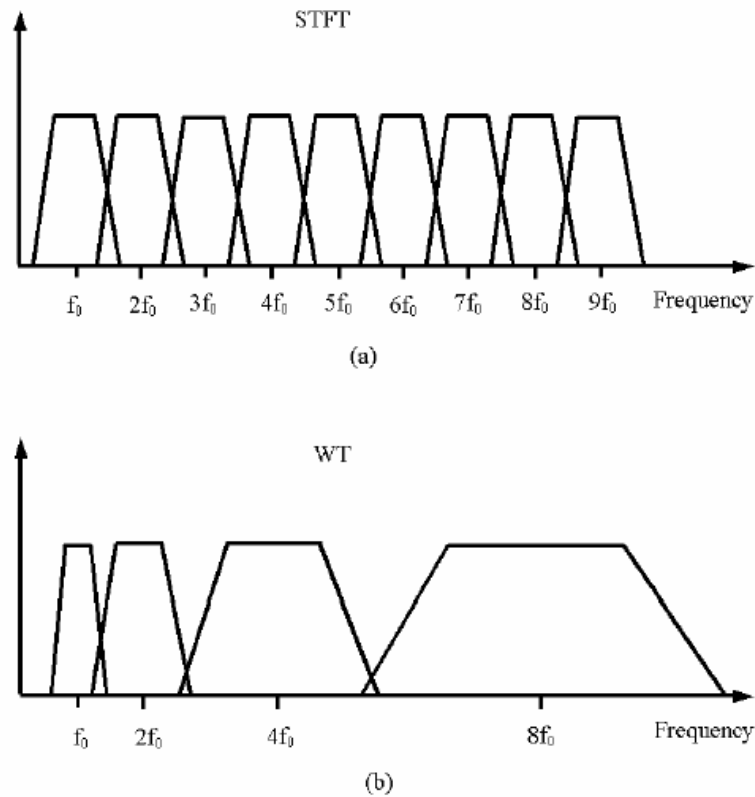


Figure 2.3 Frequency Division: Uniform for Short-Time Fourier Transform (a) and Logarithmic for Wavelet Transform (b)

2.3 Time-Frequency Analysis in Radar Imaging

Time-frequency analysis can be used to display features like discrete time events due to scattering centers, discrete frequency events like resonances and dispersive mechanisms due to higher order scattering or modes [12]. Time-Frequency analysis is being used in many radar imaging applications. The joint time-frequency representation of a signal is a 2 dimensional phase space that facilitates the visualization and interpretation of complex electromagnetic wave phenomenology.

As discussed in section 2.1, the current problem in radar imaging is that the ISAR imaging algorithm does not account for phenomena like multi-bounce effect,

creeping waves, etc. The ISAR imaging algorithm assumes the signals or returns due to above mentioned phenomena to be a part of the target scattering centers. As a result of this, artifacts can be seen in the reproduced images. It is known from physics that the early time response corresponds to the scattering from the targets and the late time response is due to the multi-bounce and other dispersive scatterings. By carefully selecting these early time responses, the effect of multi-bounce can be reduced. This approach has been implemented in this thesis and experimental results have been presented to support the hypothesis.

CHAPTER 3

LABORATORY EXPERIMENT DESCRIPTION

This chapter basically gives a detailed description of the radar cross-section (RCS) measurement facility at the Wave Scattering Research Center of the University of Texas at Arlington (UTA), involved hardware system, data acquisition hardware, software and different measurement setups used. This chapter also provides a detailed discussion on the data obtained and its analysis. It should be noted that monostatic measurements were carried out during the course of this thesis study. This chapter is organized into four sections. Section 3.1 gives a physical description of the measurement chamber and the test equipment used. Section 3.2 gives a detailed description of the data acquisition hardware setup and software programs. Section 3.3 describes the different target setups used for the imaging experiments. Finally, a detailed analysis of the obtained data is discussed in Section 3.4

3.1 Measurement System

Monostatic RCS measurements were carried out in an anechoic chamber at the Wave Scattering Research Center, UTA. The anechoic chamber is fully capable of making bi-static measurements and has a large set of possible transmit and receive antenna configurations. A detailed physical description of this anechoic chamber can be found in [9]. The equipment used in the measurement process is listed in Table 3.1.

Table 3.1 Hardware and Test Equipment Used in Mono Static Measurements

INSTRUMENT NUMBER	NAME	FREQUENCY RANGE
HP 8510C	Network Analyzer	45.0MHz – 26.5GHz
HP 8341A	Synthesized Sweeper	10.0MHz – 20.0GHz
HP 8511A	Frequency Converter	45.0MHz – 26.5GHz
HP 8349B	Microwave Amplifier	2.0GHz – 20.0 GHz
HP 8494B	Attenuator / 11dB	DC – 20.0GHz
HP 11692D	Dual Directional Coupler	2.0GHz – 18.0 GHz
Flam & Russell 8502	Positioner Programmer/ Controller	NA
NI 488.2 USB-B	USB Data Acquisition	NA

The Network Analyzer HP 8510C is capable of performing RCS measurements from 45MHz up to 26.5GHz. Two conical horn dual-polarization antennas were used as transmit and receive antennas. These two antennas mounted on a tripod stand were used to carry out monostatic measurements. Figure 3.1 shows set up used for RCS measurements. The target is placed on the pedestal which can be rotated through 0-360° using the position controller.



Figure 3.1 Illustration of a Mono-Static Setup used

3.2 Data Acquisition

The data from the Network Analyzer is transferred to a local computer/laptop using data acquisition hardware and software. It should be noted that the data transferred to the local computer is only in frequency domain with real and imaginary components. This chapter describes the hardware and software involved in the data acquisition process.

3.2.1 Hardware Description

The data acquisition hardware consists of NI-488.2 USB-B which connects the USB port of the local computer to the GPIB port of the Network Analyzer. The NI-488.2 USB-B allows data to be collected automatically. More information about this USB connector can be found at www.ni.com. Figure 3.2 shows a snap shot of this connector. As shown in the figure one end of this connector is connected to the GPIB port using a GPIB bus of the instruments being controlled.



Figure 3.2 NI GPIB USB-B Connector used for Data Acquisition

3.2.2 Software Description

The data acquisition process consists of a LabVIEW® software program developed by Dr. Jonathan Bredow, a faculty member at the WSRC, UTA. This program “FiveNewHP8510C Output Raw Data.vi” on the local computer is used to acquire data from the Network Analyzer through NI 488.2 USB-B connector. Figure 3.3 shows a snapshot of this program. As shown in the figure, the program has many input fields. The fields “VISA session NA” and “dup VISA session NA” are related to the

GPIB address of the Network Analyzer. The fields “VISA session PED” and “dup VISA session PED” correspond to the physical GPIB address of the position controller. The other inputs like “Number of Points”, “Start Frequency” and “Stop Frequency” have their usual meaning. The input field “Number of files” depends on the azimuth spacing in degrees. The measurements carried out in this study had an azimuth spacing of 5 degrees corresponding to 72 different angles or files.

Once all these input fields are set, the user has to run the program. The program obtains the data from the Network Analyzer for one angle at a time. Once the Network Analyzer sweeps all the frequencies for a particular azimuth angle, the data is displayed on the Network Analyzer and this data is also transferred to the local computer. The program controls the position controller and increments the azimuth angle by 5 degrees. The Network Analyzer sweeps again for all the frequencies and the process continues until all the angles have been finished.

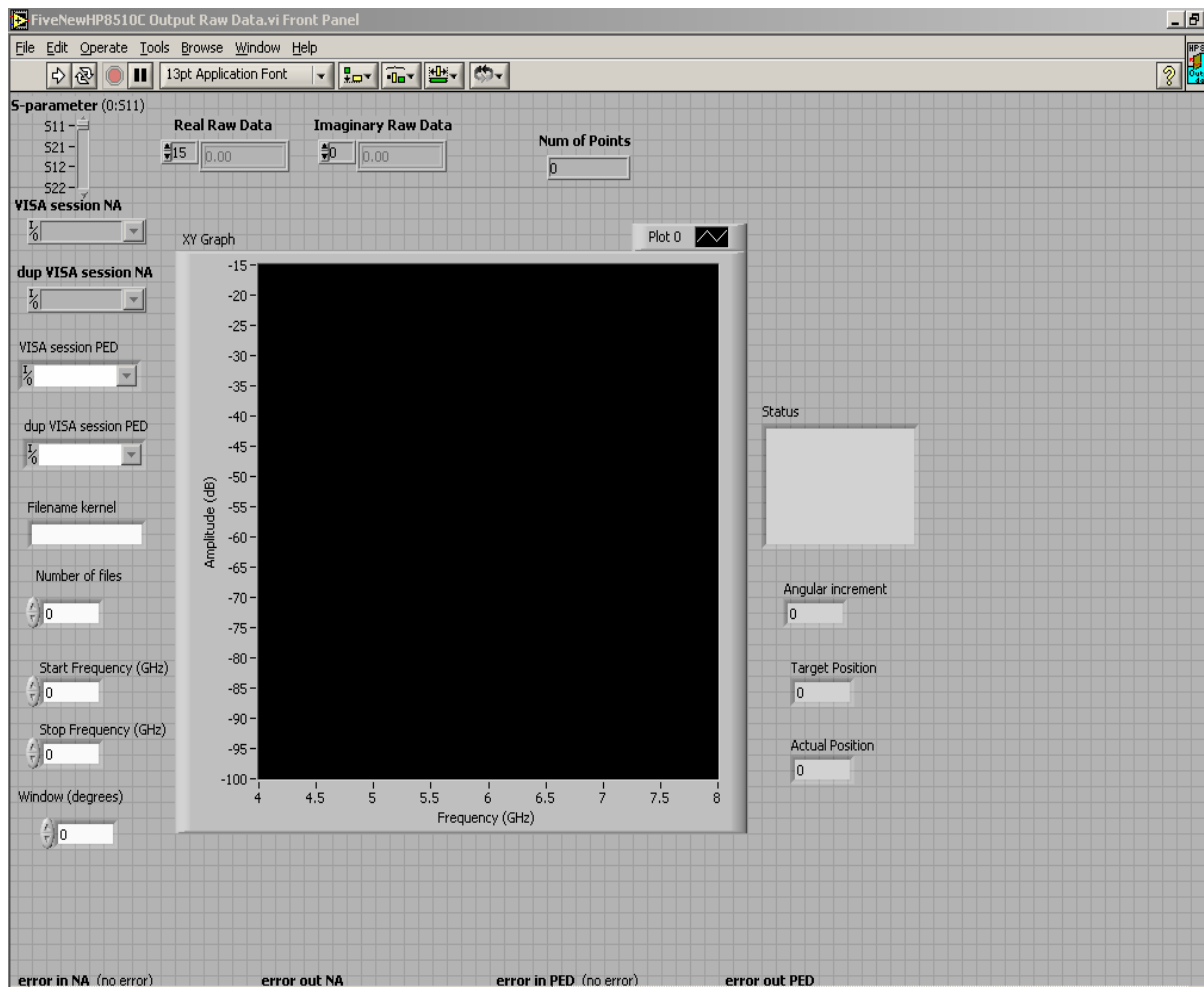


Figure 3.3 Snap Shot of the Data Acquisition Software Program

3.3 Experimental Setup

This section describes the experimental setup used to address the problem under consideration. Since the motivation for this thesis was to reduce the impact of interactions between the objects on the resulting image when they are placed near each other, the following setups shown in Figures 3.4 – 3.6 have been used.

3.3.1 Setup 1

Two spheres with 3 and 6 inch diameters were used as shown in the Figure 3.4 below. The measurement scale shown in the figure is only to show the distance between the objects and is not a part of the target setup. It can be seen from the above figure that the distance between the centers of the two spheres is just approximately 15 inches.

Other information related to this setup is shown below in Table 3.2:

Table 3.2 Test Parameters Used for Setup 1

Parameter	Value
Frequency Range	4 – 8 GHz
Number of Points	801
Frequency Spacing	5 MHz

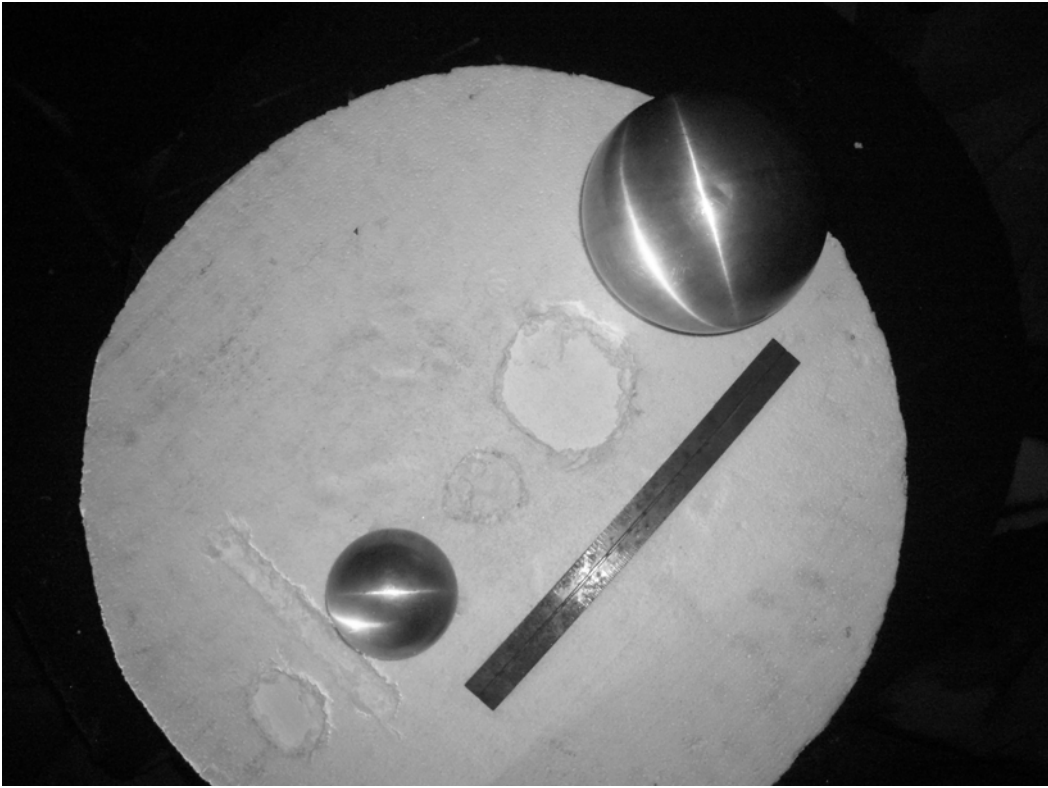


Figure 3.4 Setup 1: A 6 inch and a 3 inch Sphere Used for Imaging

3.3.2 Setup 2

Two spheres with 3 and 4 inch diameters were used as shown in the Figure 3.5 below. Again, the measurement scale shown in the above figure is only to show the distance between the targets and is not a part of the target setup. It can be seen that the distance between the centers of the two spheres is just approximately 15 inches. Other information related to this setup is shown below in Table 3.3:

Table 3.3 Test Parameters Used for Setup 2

Parameter	Value
Frequency Range	4 – 8 GHz
Number of Points	801
Frequency Spacing	5 MHz



Figure 3.5 Setup 2: A 3 inch and a 4 inch Sphere Used for Imaging

3.3.3 Setup 3

Three rods each of length of 6 inches and diameter of 0.8 inch were arranged to form a triangle shape as shown in the Figure 3.6. These rods, in this arrangement, were then buried in sand (about 3 centimeters deep) in the plastic tub as shown below. Other information related to this setup is shown below in Table 3.4:

Table 3.4 Test Parameters Used for Setup 3

Parameter	Value
Frequency Range	4 – 8 GHz
Number of Points	801
Frequency Spacing	5 MHz

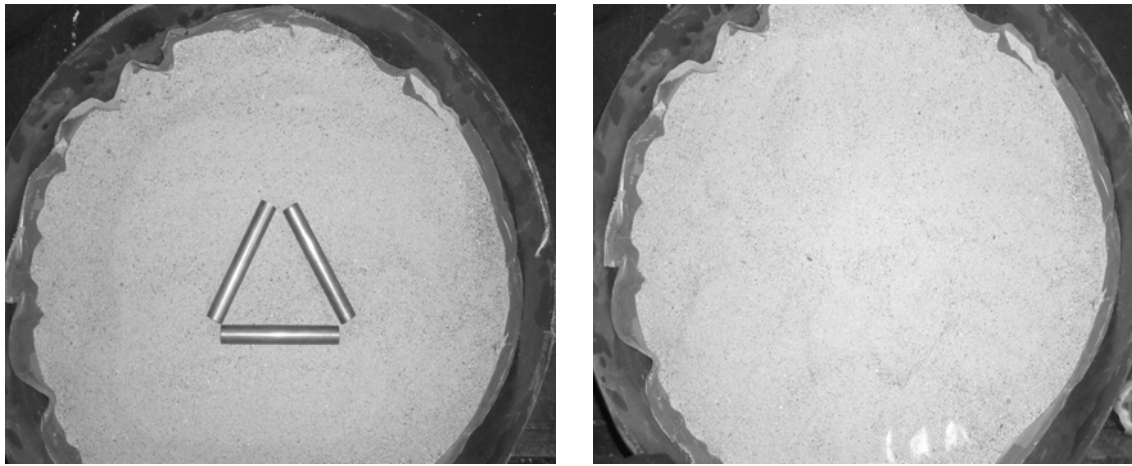


Figure 3.6 Setup 3: Three Copper Rods Forming a Triangle Shape before and after Burying in Sand

3.4 Data Analysis

This section describes the different processing that is done on the raw or uncorrected data (measured by the network analyzer) to increase its signal quality and reduce the effects of background noise and other system effects. The two main processes discussed in the subsequent sections are Back Ground Subtraction and Calibration.

3.4.1 Back Ground Subtraction

The data which is obtained from the Network Analyzer is uncorrected data in the form of real and imaginary components. This data which is stored on the local computer is read by a Matlab® program. The first processing which has to be done on this data is back ground subtraction. This process removes the effect of reflections from back ground and other unwanted returns due to the coupling between the transmitter and receiver antennas. Figure 3.7 shows the time-domain signal before and after back ground subtraction for setup 1 at an azimuth of 0 degrees.

The effect of antenna coupling is seen at around 87 ns. The sphere responses occur at around 91 and 93 ns. The response at 97 ns is due to the pedestal i.e. the target positioner. From Figure 3.7, it can be seen that the effect of coupling, pedestal and other background interference is greatly reduced after back ground subtraction. This response is now mainly from the target (two spheres). It is also observed that back ground subtraction does not remove the effect of coupling completely but it reduces the magnitude by approximately 30 db. This remaining effect of coupling can be easily removed by the process of time gating as discussed later. Back ground subtraction does

not account for phenomenon like shadowing which is caused due the interaction between background and the target. Also other effects like cabling losses, instrument errors, etc cannot be alleviated by background subtraction. For compensating these kinds of losses, calibration has to be done on the measured data

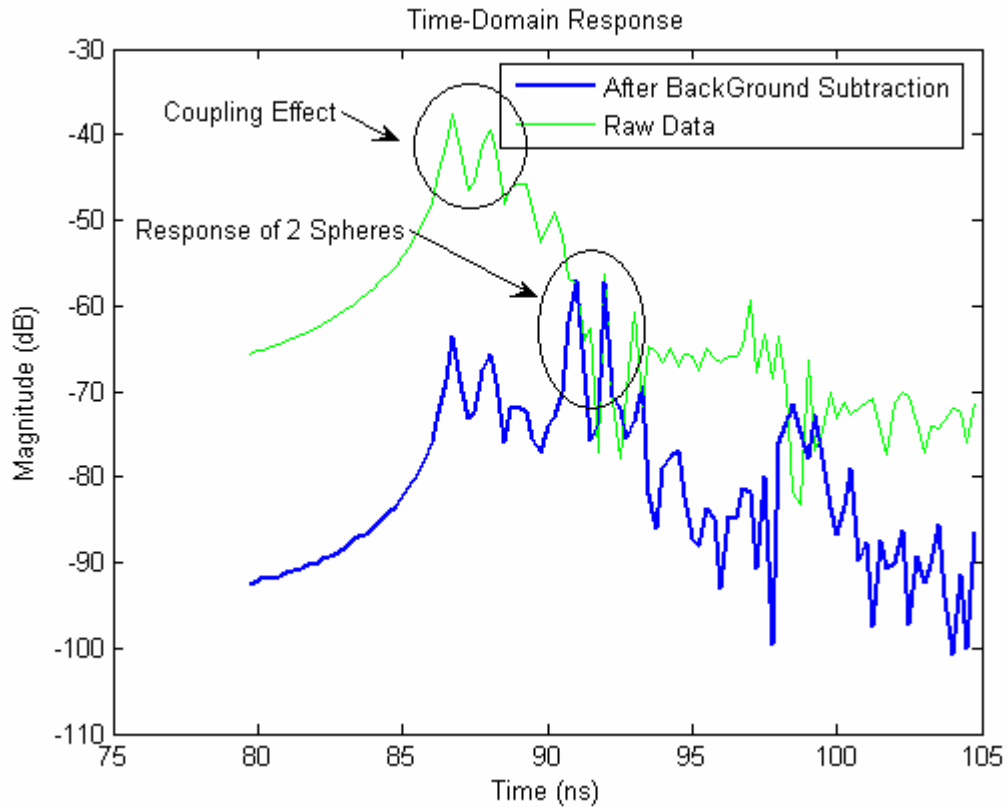


Figure 3.7 Magnitude Response Comparison between Raw Data and Corrected Data (Back Ground Subtracted Data) for 0 degrees

3.4.2 Calibration Routines

A detailed description of different calibration techniques can be found in [10].

In this thesis study the sphere calibration technique is used. This technique is a good

compromise between accuracy and complexity. A 6 inch sphere is used for the purpose of calibration. The sphere calibration process is shown below:

$$Data_{Calibrated} = \frac{(Data_{Raw} - Data_{BackGround}) * Data_{TheoreticalSphere}}{(Data_{ReferenceSphere} - Data_{BackGround})} \quad (4.1)$$

The following variables are used in the above equation:

$Data_{Raw}$	Raw data with unknown target
$Data_{Calibrated}$	Calibrated data
$Data_{BackGround}$	Back ground data (Response with no target)
$Data_{ReferenceSphere}$	Raw data with reference sphere as target
$Data_{TheoreticalSphere}$	Theoretical Response of the reference sphere

In the above equation, $Data_{TheoreticalSphere}$ is the theoretical response of the calibrating sphere. This theoretical response is generated by a FORTRAN program written by B.D Jersak called “sphere.for”, and is listed in reference [9]. After calibration, the frequency domain data is zero padded to 2048 points. It has to be noted that this operation is performed merely to increase the number of data points in the generated time-domain data. This process of zero padding will not increase the period of the time-domain data. Figure 3.8 shows the time-domain data for setup 1 after background subtraction, calibration and zero-padding for an azimuth of 0 degrees. The figure shows truncated data for better visibility. The figure shows the response of the two spheres at around 0 ns. The reason of this time shift is due to the calibration process. After the calibration process, the reference target is set to 0 ns. The effect of

coupling is seen at -5 ns. The 6 inch target is located at -1 ns and the 3 inch target is located 1 ns. It has to be noted that the time is with respect to this reference. It can also be seen that response of the 6 inch sphere has a higher magnitude as compared to that of the 3 inch target which is intuitive.

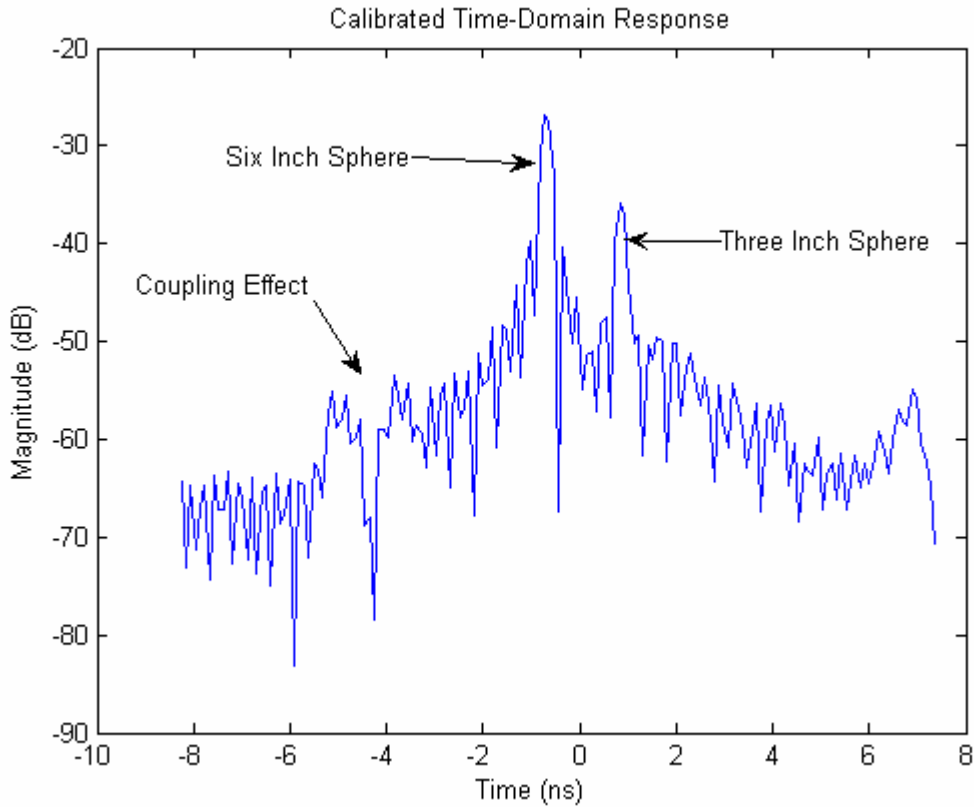


Figure 3.8 Calibrated Time-Domain Magnitude Response for 0 degrees

It can also be observed that the peak of the response after calibration has a magnitude of around -27 dB as compared to that with only background subtraction which is around -58 dB. Thus the calibration process compensates for the losses which occur due to cabling, system errors, etc.

Figure 3.9 shows the calibrated time domain data for an azimuth angle of 205 degrees which is again truncated for better visibility. At this azimuth, the distance

between the antenna and the six inch sphere is more than that of the distance between the antenna and the 3 inch sphere. This fact can be observed from the figure below. It can be seen that at this angle the response of the 3 inch sphere occurs at around -1 ns and that of the 6 inch sphere occurs at around 0 ns. The effect of coupling between the transmitter and the receiver antennas can still be seen at -5 ns.

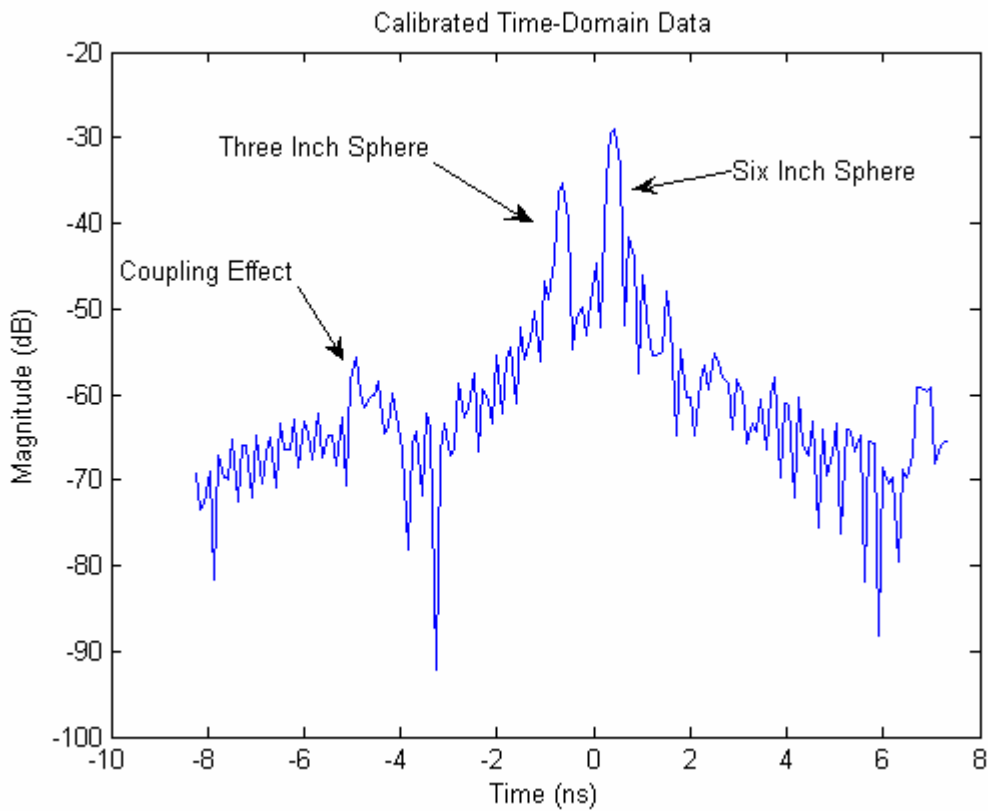


Figure 3.9 Calibrated Time-Domain Magnitude Response for 205 degrees

Figure 3.9 shows the calibrated time domain data for an azimuth angle of 90 degrees. At this azimuth, the 3 inch sphere is totally shadowed by the 6 inch sphere. As a result the transmitter antenna is not able to see the 3 inch sphere. This can be verified

from the figure below. The figure shows the response of the 6 inch target only which is at 0 ns.

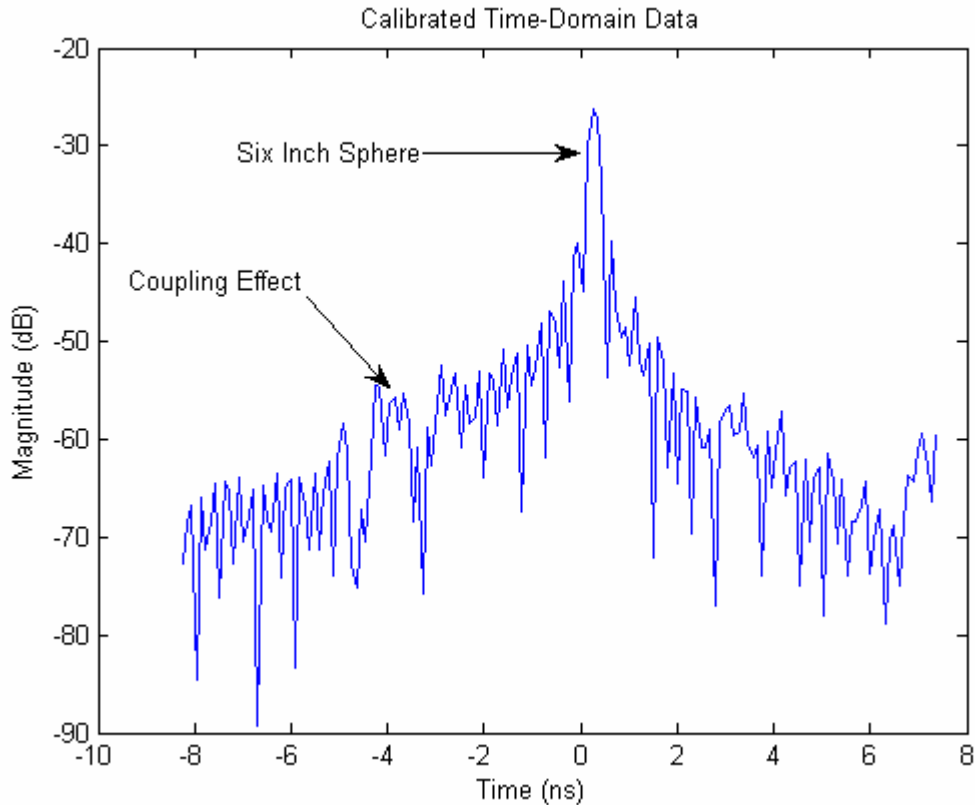


Figure 3.10 Calibrated time-domain magnitude response for 90 degrees

3.4.3 Time Gating

In section 3.4.1, it is explained how back ground subtraction technique can be used to reduce the effect of back ground noise, coupling effect from the antennas and back scattering from other objects in the chamber which can add significant contribution to the total response of the target. The back ground subtraction which is done in the spectrum domain cannot remove these different noises or clutter completely. This can be verified from figures 3.8 to 3.10. The back ground subtraction technique

reduces the magnitude of such back ground noise but not completely eliminate it. As a result, there is still some clutter present in the time domain data as can be seen from the above figures. To avoid this problem, time gating technique which is form of spatial filtering is used. This is achieved by windowing the time-domain response with different gating functions. The HP 8510C has a built in time gating function. It uses three kinds of windowing functions, Rectangular, Hanning, Hamming and Blackman windows, Rectangular being the minimum width and Blackman being the maximum width windows. The data which is obtained from the data acquisition process is in the spectrum domain and the time-domain data generated by HP 8510C cannot not transferred onto the local computer. Thus time gating routines are generally developed externally which allows flexibility to change to different windowing functions and different widths depending upon the need. For setup1, a time gate of around 2-3 nanoseconds can be used to select the response due to the two spheres. As can be seen from figures 3.8-3.10, the distance between the two peaks is not constant for all the angles due to which the width of the time gate needs to be adapted accordingly. This increases the complexity of the time-gating routine. Interested users can refer to B.D Jersak [9] for a detailed explanation of time gating functions and their implementations in external software programs

Figure 3.11 shows a flow chart for generating a calibrated frequency domain data which is free from different kinds of noises as compared to the raw or uncorrected data obtained from HP 8510C.

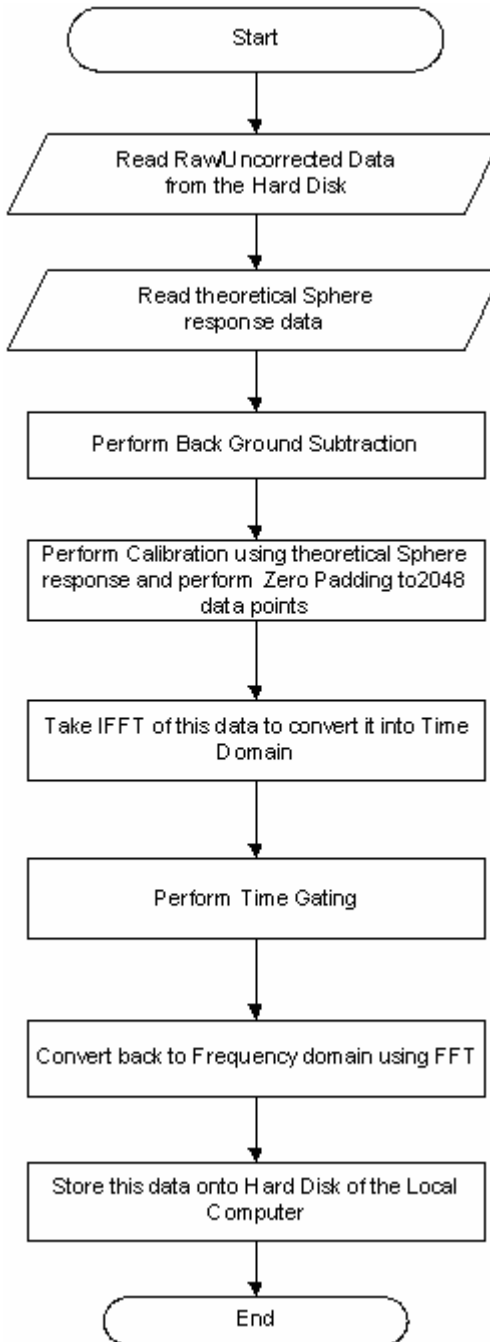


Figure 3.11 Flow Chart for Back Ground Subtraction, Calibration and Time Gating

CHAPTER 4

ISAR IMAGING ALGORITHM AND TIME-FREQUENCY ANALYSIS

This chapter gives a good description of the algorithm used for generating ISAR images of the targets under consideration. The first part of this chapter describes the ISAR algorithm used. The second part of this chapter describes the time-frequency analysis of this calibrated data to improve target identification by separating different interactions.

4.1 ISAR Imaging Algorithm and Implementation

The next step after time gating is to convert this time gated, calibrated data back into the frequency domain. This frequency domain data is then used by the ISAR imaging program to produce an image of the target under consideration. This section describes the ISAR imaging algorithm used to produce the images of the target under consideration.

4.1.1 ISAR Imaging Algorithm

Figure 4.1 shows a flowchart of the algorithm used to generate ISAR images of the targets. The ISAR imaging program reads the time-gated, calibrated data which is in the spectrum domain and generates ISAR images of the target under consideration. Since the number of points used is 801(frequency spacing of 5MHz) and the azimuth separation is 5 degrees, the data obtained by the Network Analyzer is an array of 72x801 real and imaginary numbers. Now this data which is in spectrum domain is in

polar form since the measurements are taken by varying the value of phi (azimuth) from 0 to 360 degrees. As discussed in chapter 2, this data obtained in the spectrum domain is related to the shape of the target under consideration by Fourier Transform. Thus, to obtain the image of the target, an Inverse Fourier Transform has to be applied on the spectrum domain data. Now, for computing IFFT, this data (obtained in polar form) has to be converted to rectangular form. Interpolation is used to convert this polar (radial) data to rectangular data. Figure 4.2 shows how the interpolation function converts this radial data into rectangular data. The nearest neighbor technique is used to perform interpolation. Care has to be taken that the interpolated data in the region of uncertainty as shown in the figure 4.2 is zero. After interpolation, the ISAR image is generated by taking a 2 dimensional IFFT of this data. Note that the resolution of the generated ISAR image is given by [18]:

$$dx = dy = \frac{2\pi}{dk * nfft} \sin \theta \quad (4.1)$$

where, dk is the resolution of the interpolated k-space data, $nfft$ is IFFT order used to obtain the image and θ is the elevation which is around 45 degrees in all the test setups used for this thesis. Also, it has to be noted that the scale in all the figures showing generated ISAR images is in meters.

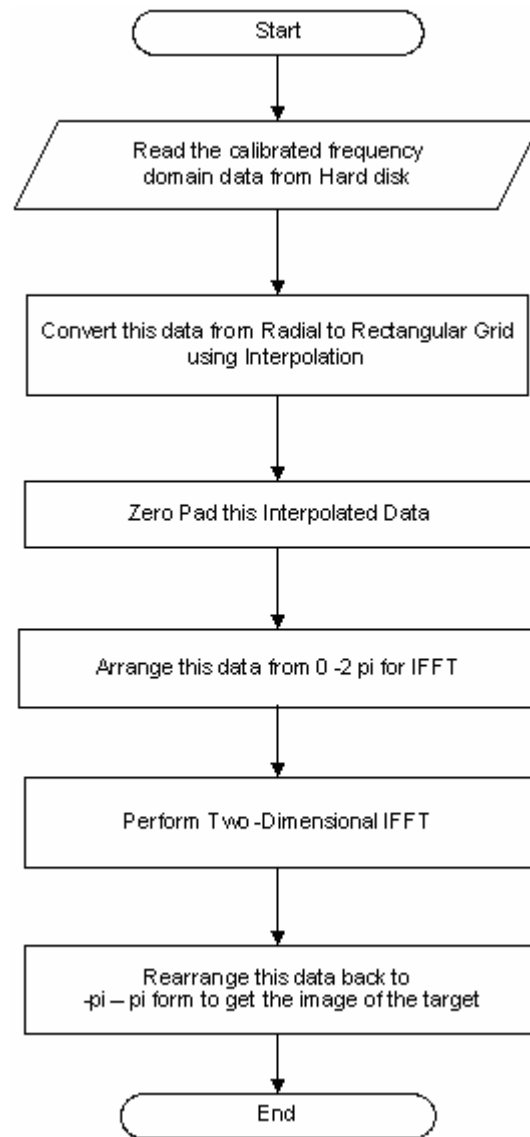


Figure 4.1 Flow chart for ISAR Imaging

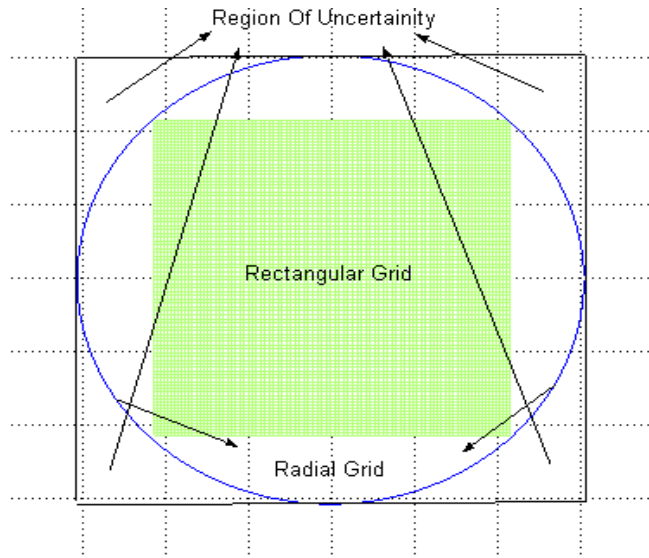


Figure 4.2 Interpolation Process

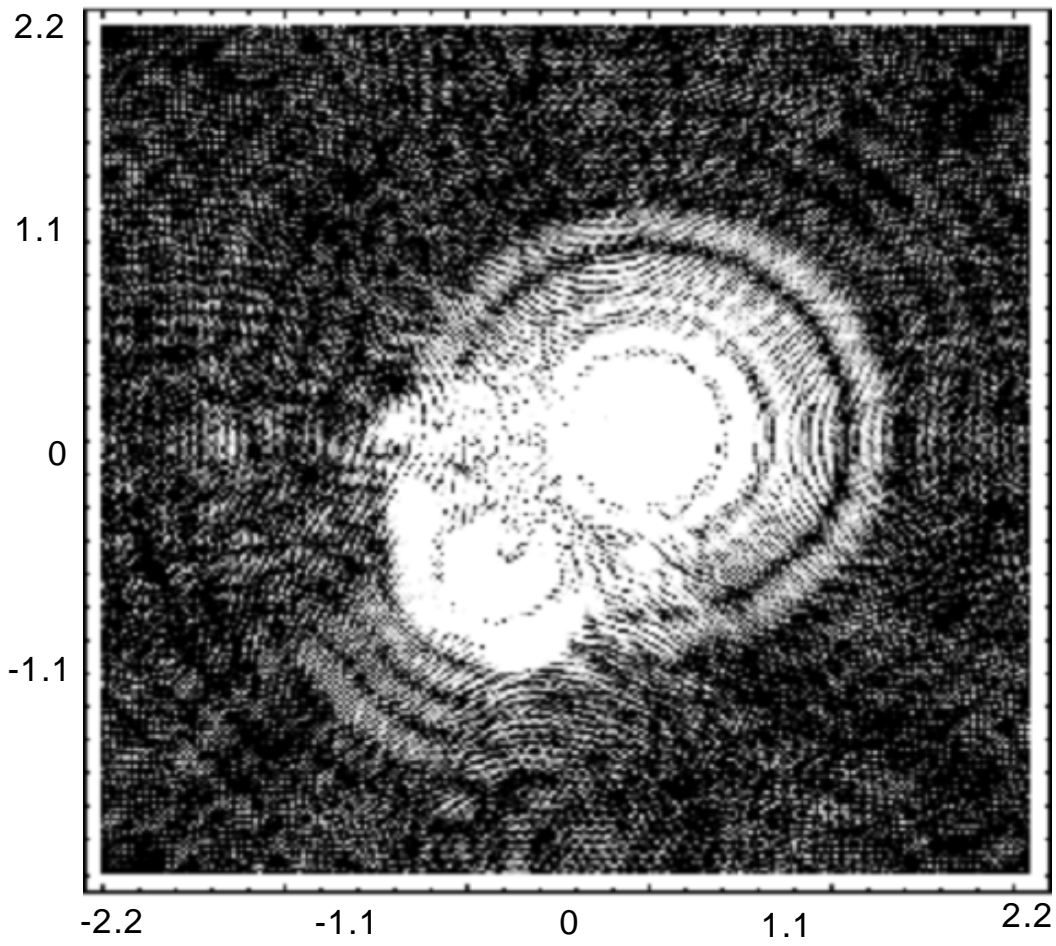


Figure 4.3 Generated ISAR Image of Test Set 1 (3 and 6 inch spheres)

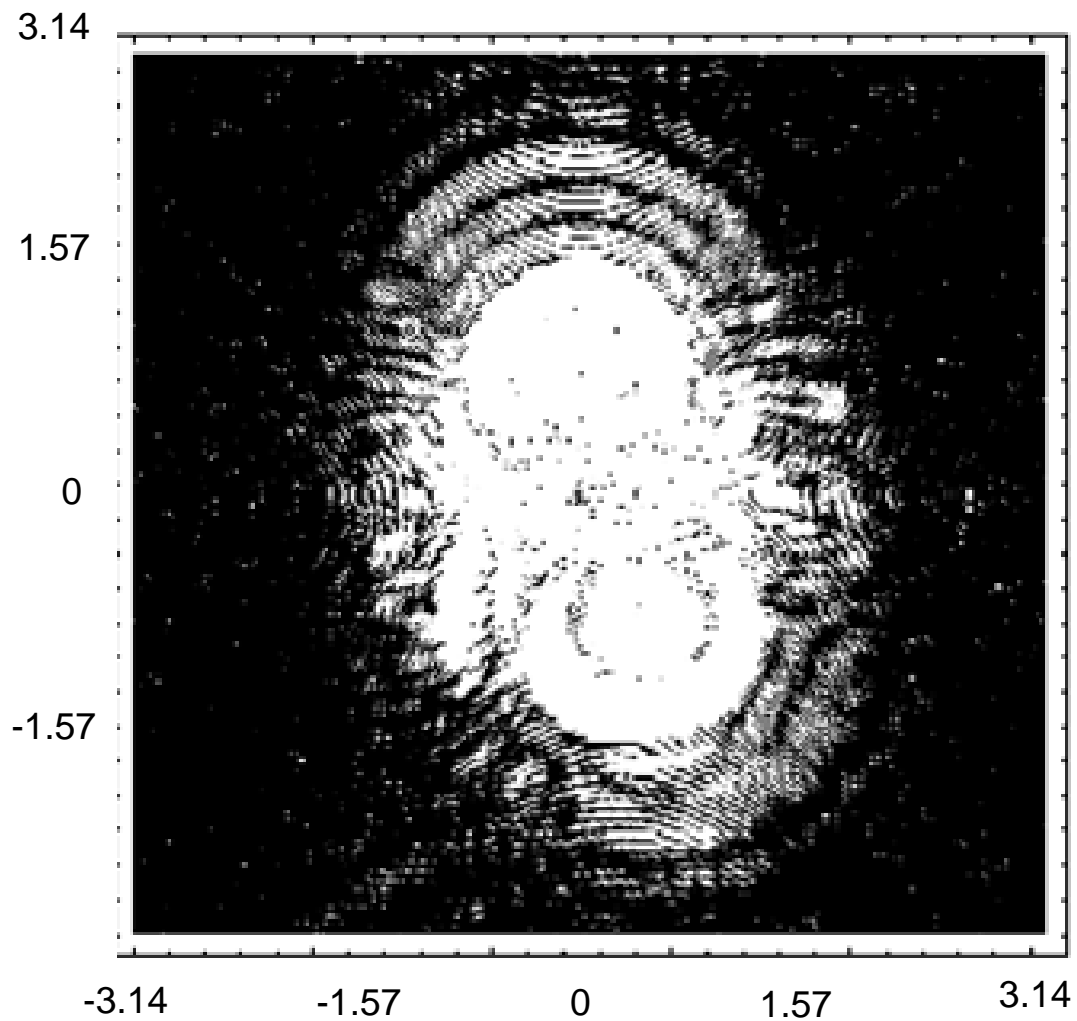


Figure 4.4 Generated ISAR Image of Test Set 2 (3 and 4 inch spheres)

Figures 4.3, 4.4 show the generated images of the targets in test sets 1-2 respectively. From these images, the effect of different artifacts can be clearly seen. This is mainly due to the interaction between the targets and other non-point scattering phenomenon. Section 4.2 describes this phenomenon in detail and ways to reduce this problem in order to improve the quality of the generated image.

4.2 Time-Frequency Analysis using Wavelets

As seen above from Figures 4.3- 4.4, the ISAR images show the effects of multi-bounce and interactions between the targets, background, etc. The ISAR algorithm does not account for this phenomenon. This section describes a physics based approach to reduce these effects by performing a time-frequency analysis on these radar return signals.

4.2.1 Wavelet Implementation in Frequency Domain

Wavelets can be used to obtain multi-resolution [15-17]. The hypothesis of this thesis is that wavelets can be applied to radar return signals (in spectrum domain) to obtain multi-resolution. This multi-resolution obtained in the spectrum domain can then be related to different slices in the time domain. To explain this concept better, consider figure 4.5 which shows a filter bank approach to obtain multi-resolution. The blocks H_0 and H_1 in the figure are low-pass and high-pass analysis filters respectively. This figure shows how the data (in time or frequency domain) can be decomposed into different sub-bands each stage. Now from figure 4.5 we can say that there are 4 branches or outputs to be considered. Considering the fact that a decimator ($\downarrow 2$) followed by the filter ($H(z)$) is same as the filter ($H(z^2)$) followed by the decimator ($\downarrow 2$) (Noble Identities [19]), we can have the following four outputs as shown in figure 4.6 as follows:

$$H_1^{(1)}(z) = H_1(z) \quad (4.2)$$

$$H_1^{(2)}(z) = H_0(z) H_1(z^2) \quad (4.3)$$

$$H_1^{(3)}(z) = H_0(z) H_0(z^2) H_1(z^4) \quad (4.4)$$

$$H_0^{(3)}(z) = H_0(z) H_0(z^2) H_0(z^4) \quad (4.5)$$

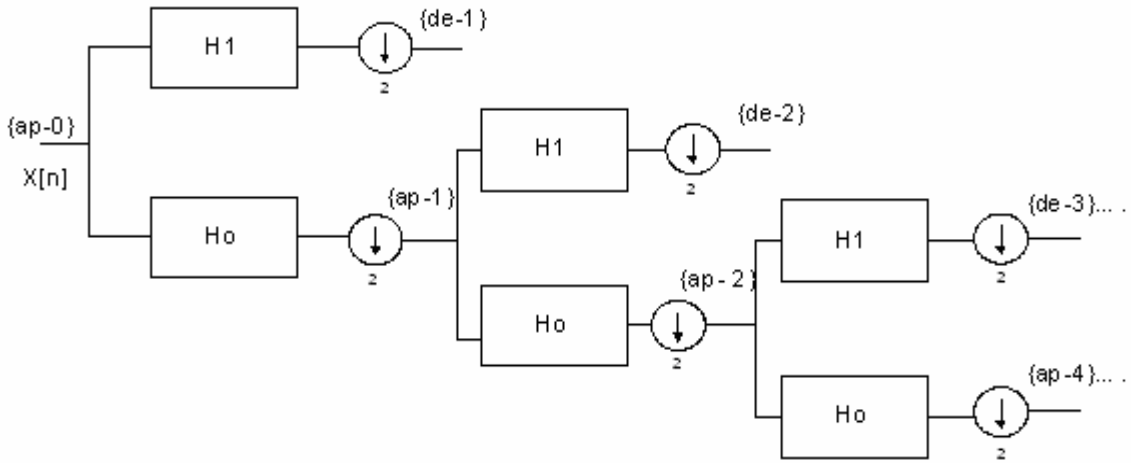


Figure 4.5 Wavelet Filter Bank

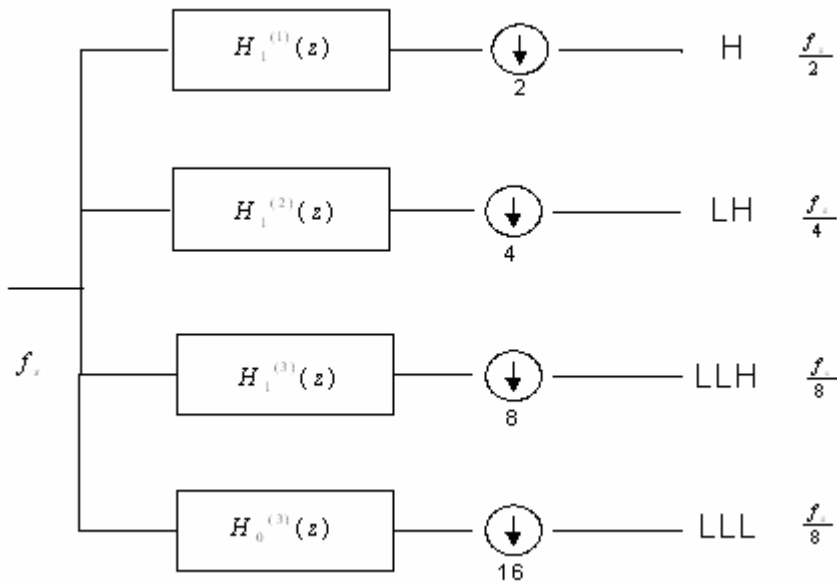


Figure 4.6 Outputs of a 3-Stage 2 Channel Filter Bank

Thus for a 3 stage 2 channel filter bank, we have [19-21]

$$H_0^{(3)}(z) = H_0(z^{2^2}) H_0^{(2)}(z) = \prod_{k=0}^2 H_0(z^{2^k}) \quad (4.6)$$

$$H_1^{(3)}(z) = H_1(z^{2^2}) H_0^{(2)}(z) = H_1(z^{2^2}) \prod_{k=0}^1 H_0(z^{2^k}) \quad (4.7)$$

It can be seen from figure 4.6 that the outputs at each of the branches span different bands in the transform domain or the frequency domain in this case. If we have a an input $x[n]$ which has a rate of f_s then the rates at the output branches will be $\frac{f_s}{2}$, $\frac{f_s}{4}$, $\frac{f_s}{8}$ and $\frac{f_s}{8}$. Thus it can be seen that the input band of frequencies are decomposed into dyadic sub-bands (which correspond to different output branches or resolutions) as shown in figure 4.7. Figure 4.7 shows the frequency split which can be obtained by for the filter bank shown in figure 4.5.

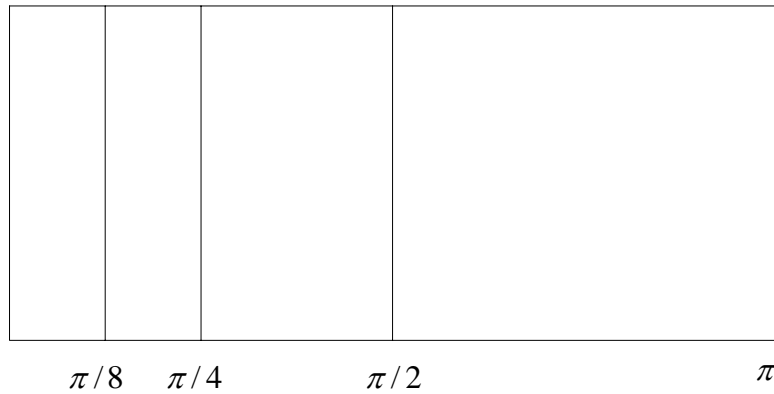


Figure 4.7 Frequency Band Split of a 3-Stage 2 Channel Filter Bank

Generalizing the above discussion for a J stage 2 channel filter bank, we have the following output branches or resolutions:

$$H_0^{(J)}(z) = \prod_{k=0}^{J-1} H_0(z^{2^k}) \quad (4.8)$$

$$H_1^{(j)} = H_1(z^{2^{j-1}}) \prod_{k=0}^{j-2} H_0(z^{2^k}), \quad j = 1, 2, \dots, J \quad (4.9)$$

Equations 4.8 and 4.9 show how a J stage 2 channel filter bank splits the spectrum of the transform domain in a dyadic fashion.

In the above discussion, the input signal $x[n]$ was split into different frequency bands using filter bank approach. Now consider a signal $X(\omega)$ which is the frequency domain. Without loss of generality, we can say that the above mentioned filter bank when applied to this frequency domain signal will split the transform domain (which is time domain in this case) in a dyadic fashion. Thus the concept of time-frequency analysis comes in to picture where in different resolution/branches of the filter bank are related to different time slices (sub-bands).

Figure 4.8 shows the relation between these resolutions in each domain. The x-axis corresponds to frequency and y-axis corresponds to the arrival times. It can be seen that higher resolutions in frequency domain correspond to longer arrival times. Thus, multi-resolution applied to frequency domain data can be related to different arrival times in the transform domain or time domain. Thus, these orthogonal resolutions in frequency domain (obtained by using wavelets) can be related orthogonal arrival times in time domain. This is illustrated in figure 4.9 The exact relation between each resolution and corresponding time slice or gate is given in Table 4.1. In this table,

resolution 1 corresponds to the highest resolution while resolution 10 corresponds to the lowest resolution. It has to be noted that these time gates are strictly with respect to the data used in this thesis (since time-domain data has a period of 200 ns with 2048 points).

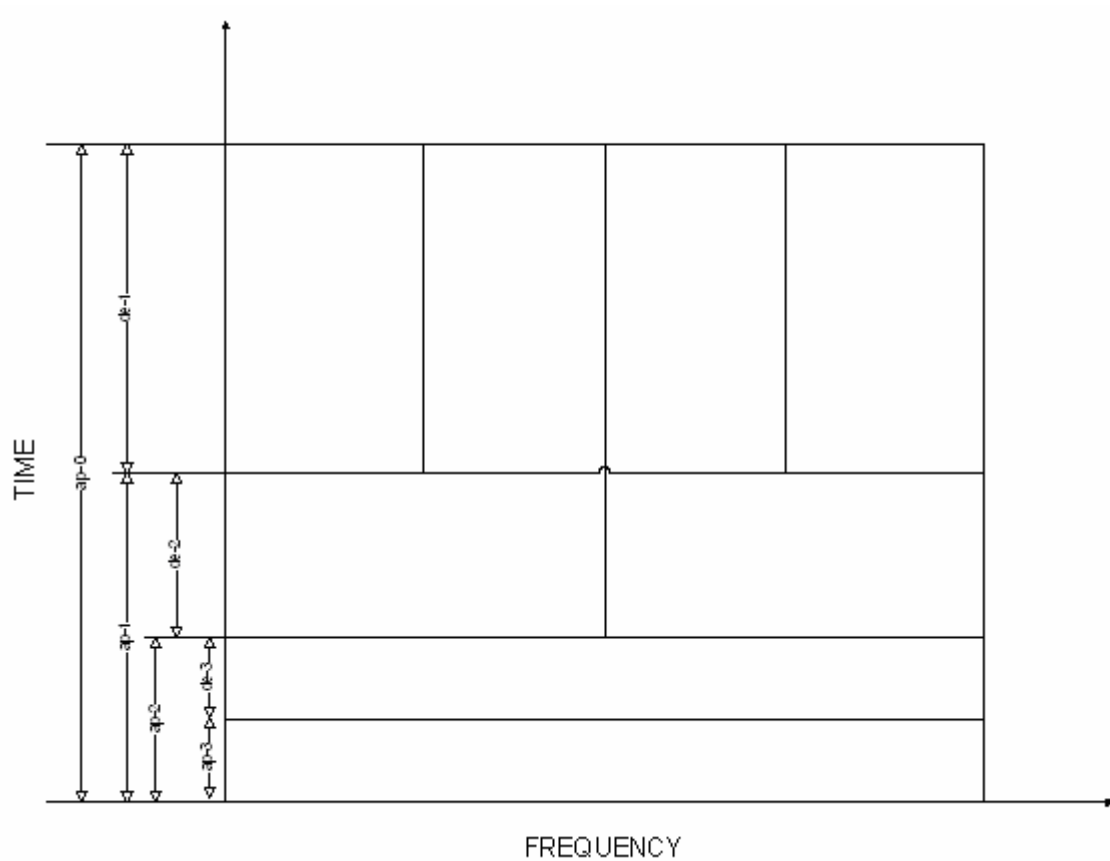


Figure 4.8 Time-Frequency Diagram of a Wavelet Filter Bank

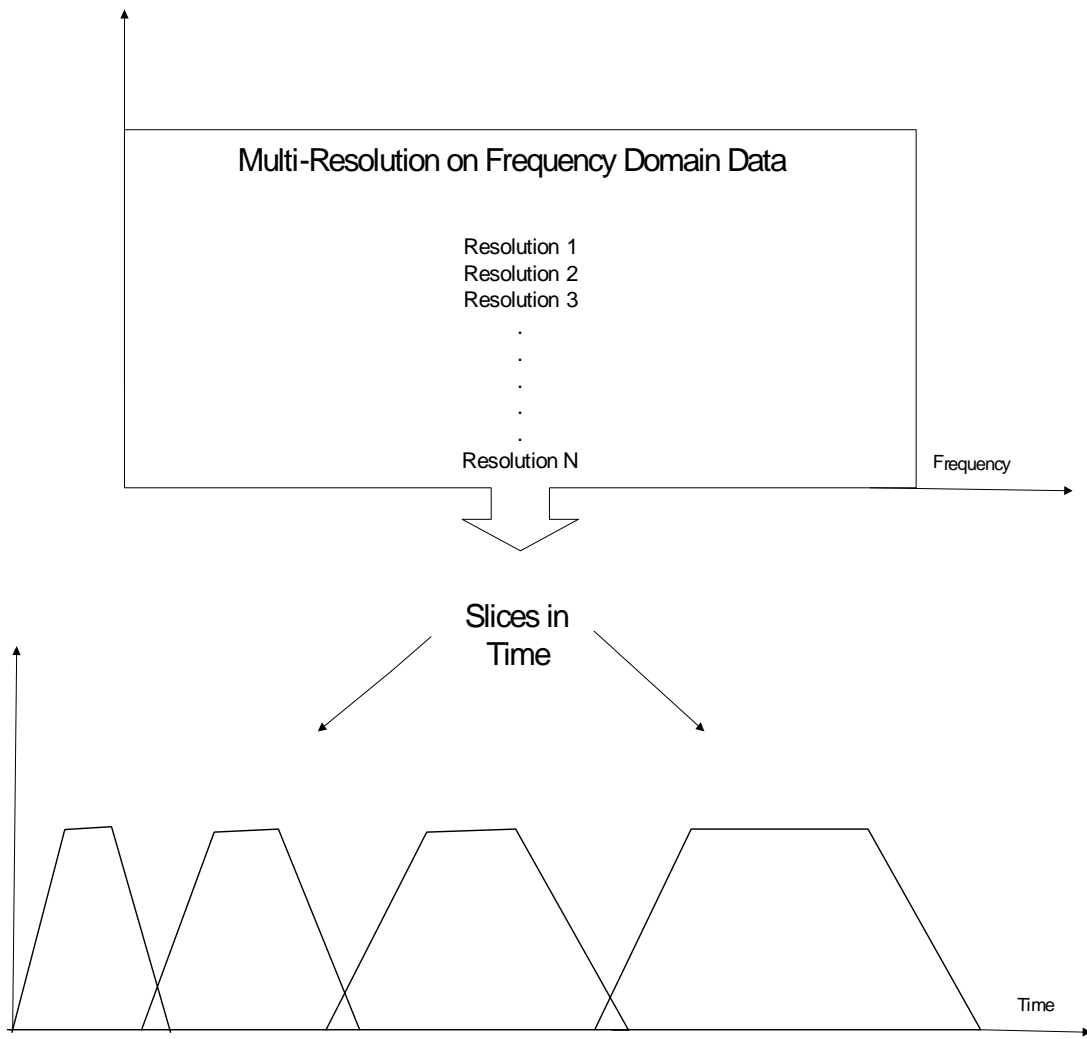


Figure 4.9 Wavelet Implementation in Frequency Domain

Table 4.1 Relation between Resolution and Time Gate width (for 2048 length data)

Resolution	Gate Width (points)	Gate width (ns)	Location of gate in time (ns)
1	1024	100	-100 to -50 & 50 to 100
2	524	50	-50 to -25 & 25 to 50
3	256	25	-25 to 12.25 & 12.25 to 25
4	128	12.25	-12.25 to -6.12 & 6.125 to 12.25
5	64	6.125	-6.125 to -3.063 & 3.063 to 6.125
6	32	3.063	-3.063 to -1.531 & 1.531 to 3.063
7	16	1.531	-1.531 to -0.765 & 0.765 to 1.531
8	8	0.765	-0.765 to -0.383 & 0.383 to 0.765
9	4	0.383	-0.383 to -0.191 & 0.191 to 0.383
10	2	0.191	-0.191 to 0.191

From physics, it is known that signals from direct bounce correspond to early time arrivals and the signals from multi-bounce and other interactions which are dispersive in nature correspond to later arrival times. As discussed above, lower resolutions of the frequency domain data can be related to early time arrivals in time-domain. So by choosing only some of these lower resolutions, the direct path signals arriving at the antenna can be separated from the late arrivals which correspond to different interactions, multi-bounce, etc. Figure 4.10 shows the time-frequency representation of the radar returns for setup 2 at an azimuth of 0 degrees using Short

Time Fourier Transform (STFT). From this figure, it can be seen that the two bright lines correspond to the two spheres. The direct returns from spheres are discrete events in time since ideally each sphere can be considered as a single scattering center. Thus the two discrete time events as shown in the figure below are due to the two spheres. The less bright regions occurring later in the time can be attributed to other non-point interactions like multi-bounce between the targets and creeping waves which are dispersive in nature.

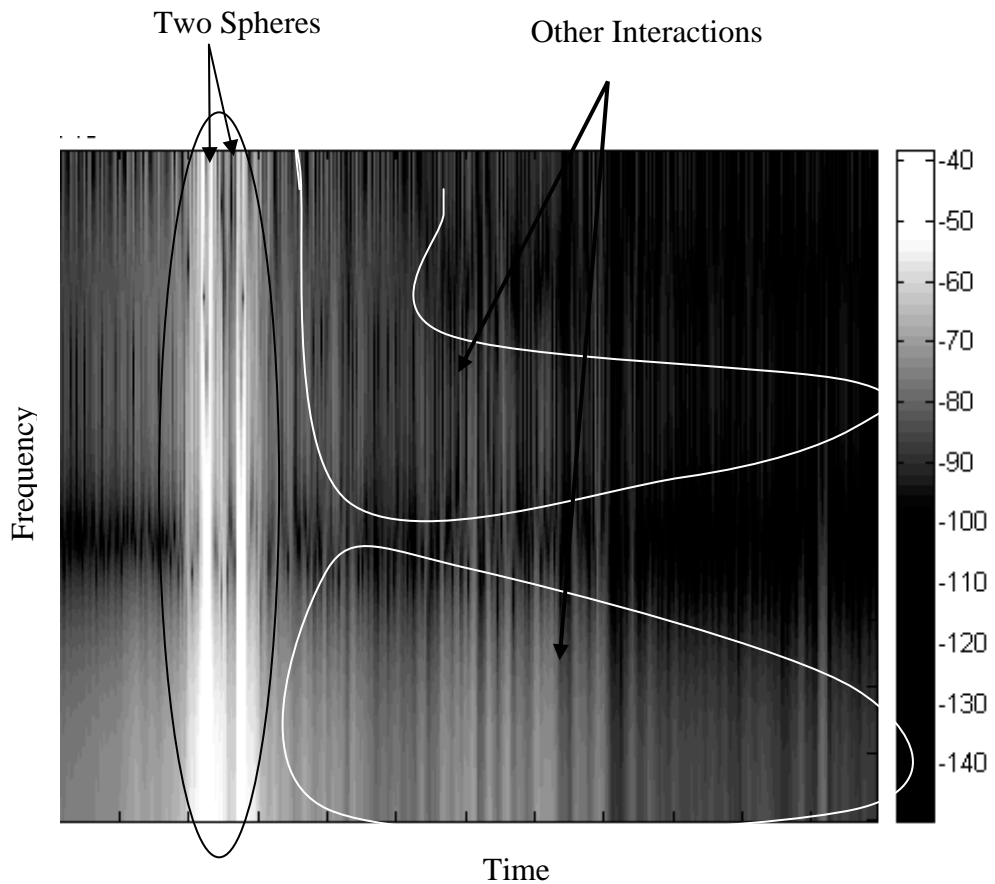


Figure 4.10 Time- Frequency Representation of Radar Returns for Setup 2 for an Azimuth of 0 degrees using STFT

As discussed in chapter 2, the main drawback of using STFT is that this method gives a fixed resolution. But it is desirable to have multi-resolution in order to separate different interactions in time. As a result of this, methods which are useful in obtaining multi-resolution are desired. Thus, wavelets have been used to obtain multi-resolution.

4.2.2 Wavelet Implementation Algorithm

As discussed in the previous section, wavelets can be used to obtain multi-resolution. Figure 4.11 explains the algorithm used to obtain multi-resolution of the frequency domain data.

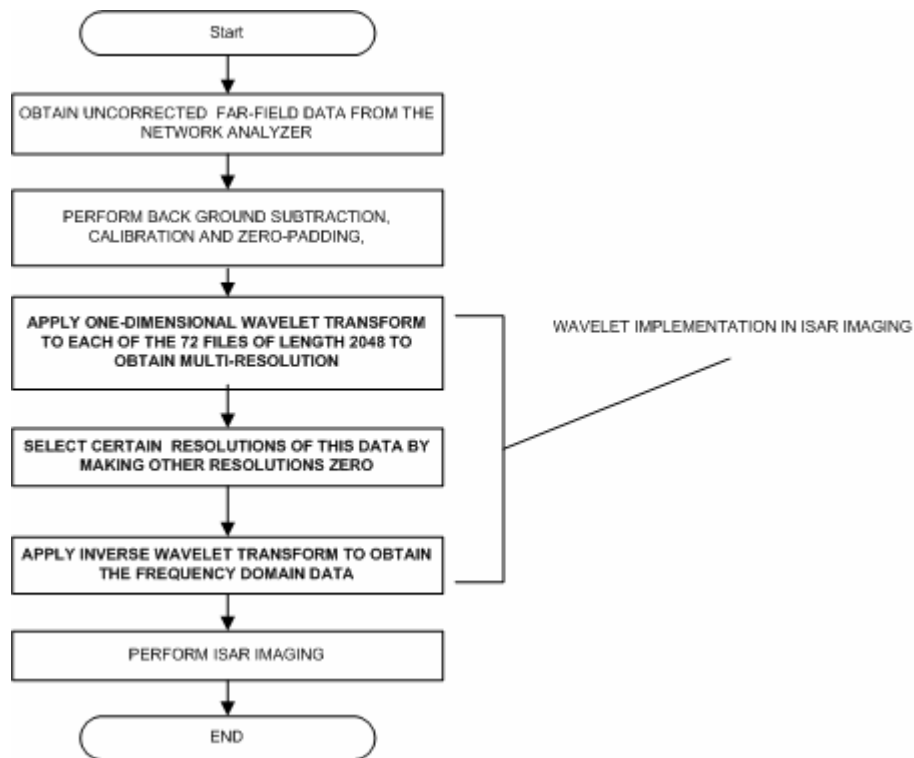


Figure 4.11 Wavelet Implementation Algorithm

Chapter 3 discussed the time-domain processing which is done to improve the signal to clutter ratio of the data. Now this data (after time-domain processing) is converted back into frequency domain and has dimensions of 72 x 2048. Now to obtain multi-resolution of this frequency domain data, a one-dimensional wavelet transform has to be performed on each of the 72 rows (representing 72 azimuth angles) each row having a length of 2048. After choosing a particular wavelet and performing wavelet transform, different resolutions of this frequency domain data are obtained. By choosing some of the lower resolutions, the direct path signals (corresponding to early arrival times) can be separated from signals coming from late arrivals which normally correspond to non-point interactions and clutter. To understand this better, consider a time-domain signal as shown in figure 4.12

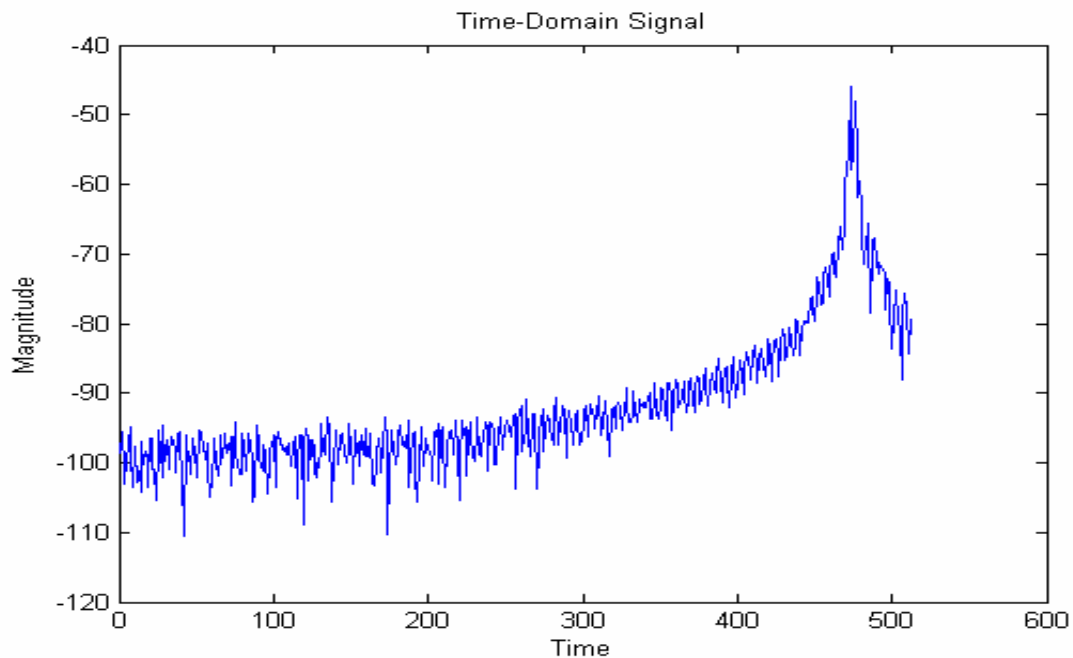


Figure 4.12 A Signal in Time Domain

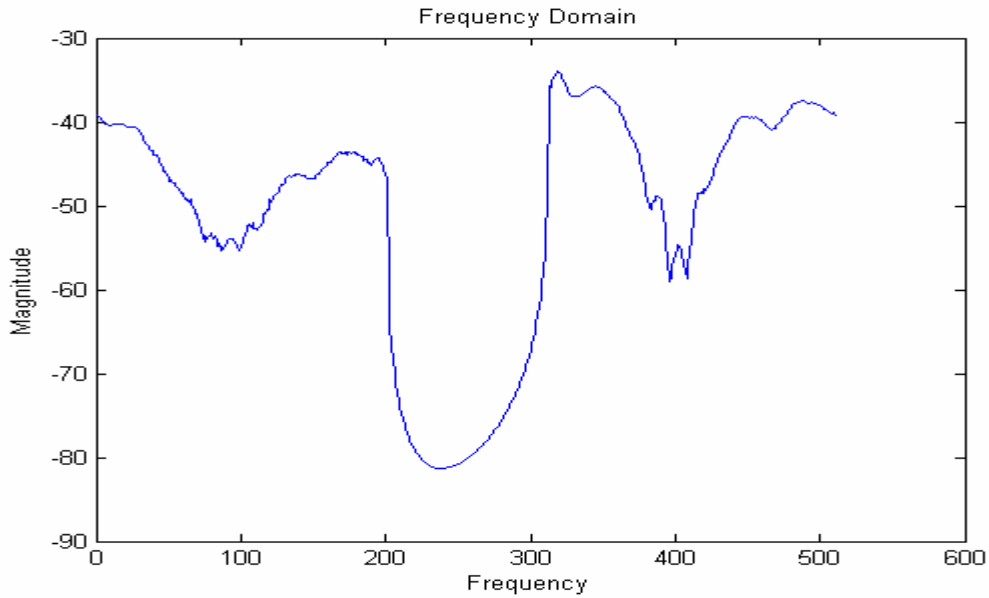


Figure 4.13 Frequency Response of the Time-Domain Signal

Figure 4.13 is the frequency information of the time-domain signal shown in figure 4.12 which is obtained by taking Fourier Transform. Now as discussed earlier, a multi-resolution this frequency domain signal is obtained using a filter bank approach (using Wavelets). For this case, the signal was resolved into four orthogonal resolutions H, LH, LLH and LLL respectively. Figures 4.14, 4.15, 4.16 and 4.17 show the time domain signal obtained by selecting resolution 1, 2, 3 and 4 of the frequency domain signal respectively. It can be clearly seen that each of these orthogonal resolutions in frequency domain correspond to orthogonal time bands in the time domain. Thus, this approach can be used to separate different interactions in time for the test sets 1-3 as explained later.

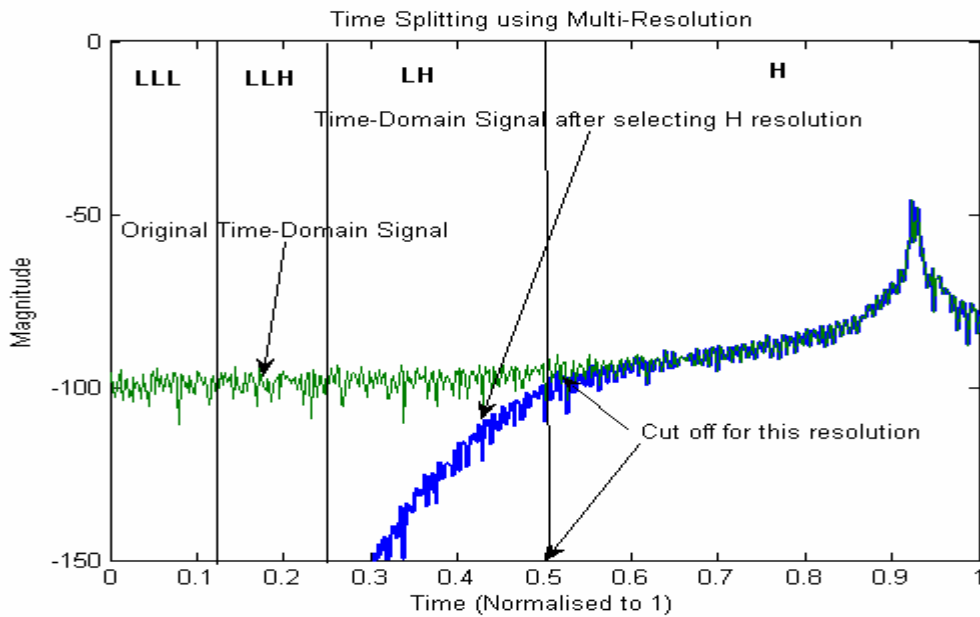


Figure 4.14 Time-Domain Signal obtained by Considering Resolution 1 (H) of the Frequency Domain Signal

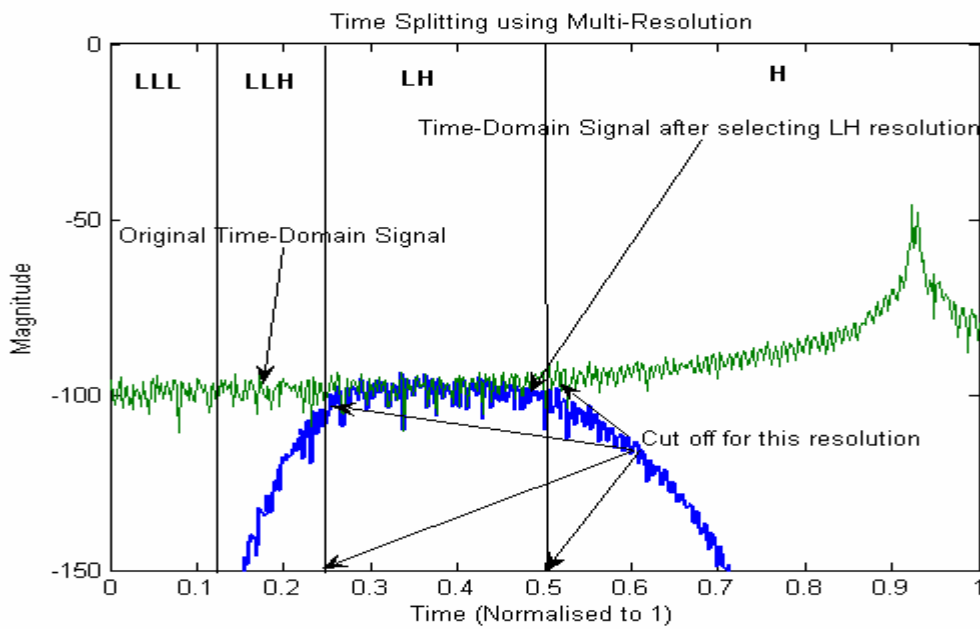


Figure 4.15 Time-Domain Signal obtained by Considering Resolution 2 (LH) of the Frequency Domain Signal

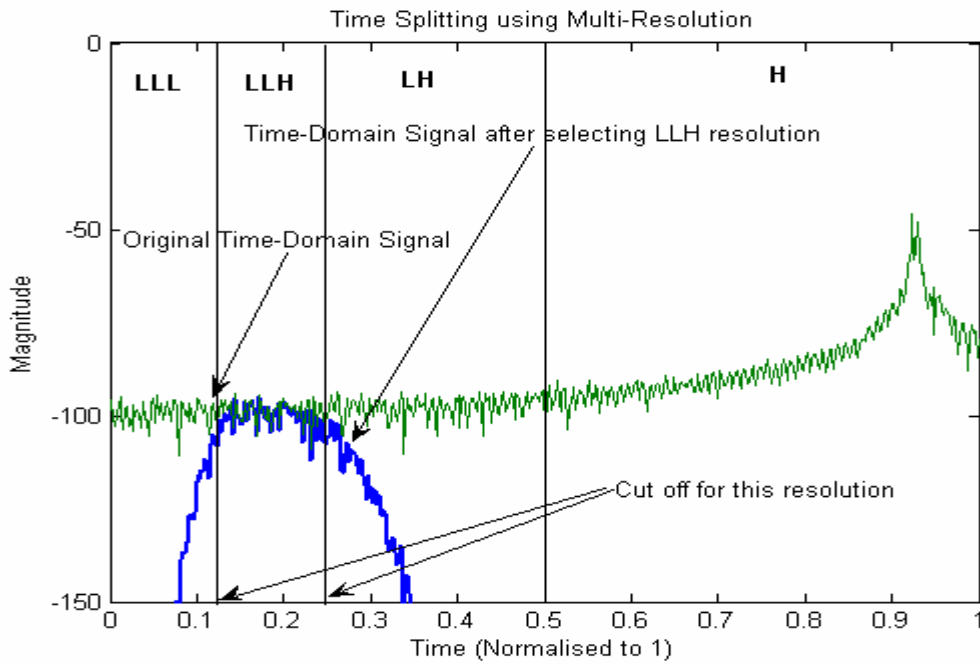


Figure 4.16 Time-Domain Signal obtained by Considering Resolution 3 (LLH) of the Frequency Domain Signal

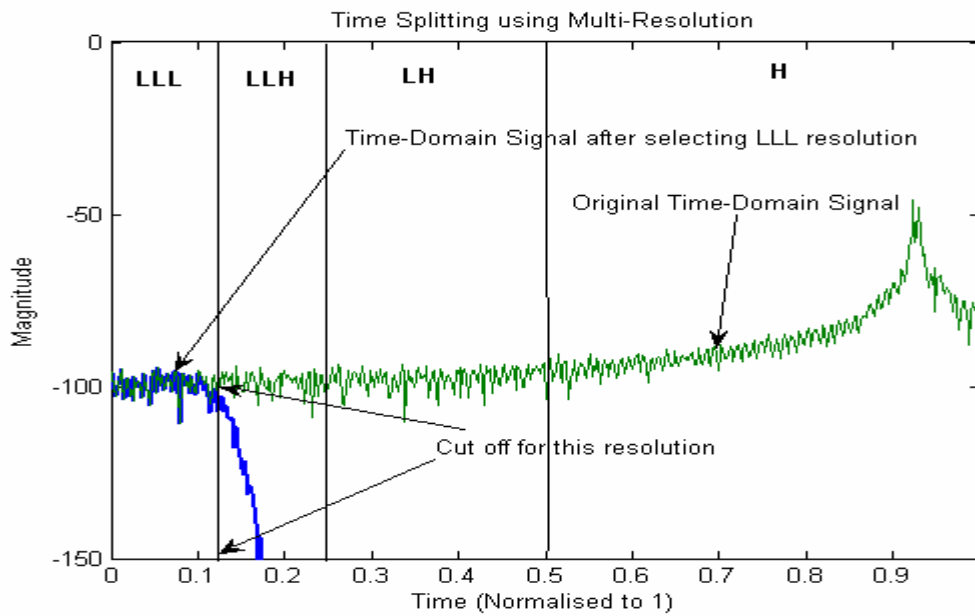


Figure 4.17 Time-Domain Signal obtained by Considering Resolution 4 (LLL) of Frequency Domain Signal

For test set 1, Daubechies (db2) wavelets were used for simplicity. Equation 4.3 is the transfer function of Daubechies 2(db2) filter.

$$db2(z) = \frac{1}{2}(-z + 4 - z^{-1}) \quad (4.3)$$

Solving the above quadratic equation, the coefficients of the Daubechies 2(db2) are obtained as shown in equation 4.4

$$db2(n) = [0.482963, 0.836516, 0.224144, -0.12941] \quad (4.4)$$

The frequency domain data was divided into 10 resolutions or details, the first being the most high frequency detail. Figure 4.18 shows a comparison of the original time-domain data and the time-domain data obtained after selecting lower resolutions (7-9) of the frequency domain data. This set of data is for an azimuth of 0 degrees. It can be clearly seen that the effect of clutter in the time-domain data has been reduced to quite an extent. This decrease in the clutter as compared to the original data is about 40 dB. Also it can be seen that there is no change in the magnitude of the data which corresponds to the target. The magnitude of the target response in the original time-domain data and that after wavelet application in frequency domain is same. Only the clutter is reduced to a great extent. This can be verified again from figure 4.19 which shows the same comparison for an azimuth of 50 degrees. Figure 4.20 and 4.21 show the effect of selecting higher resolutions (1-6) of the frequency domain data. It can be seen that the magnitude of clutter in the time-domain is same for the original data and that after wavelet application. Also, the magnitude of the target is reduced to quite an extent after wavelet application.

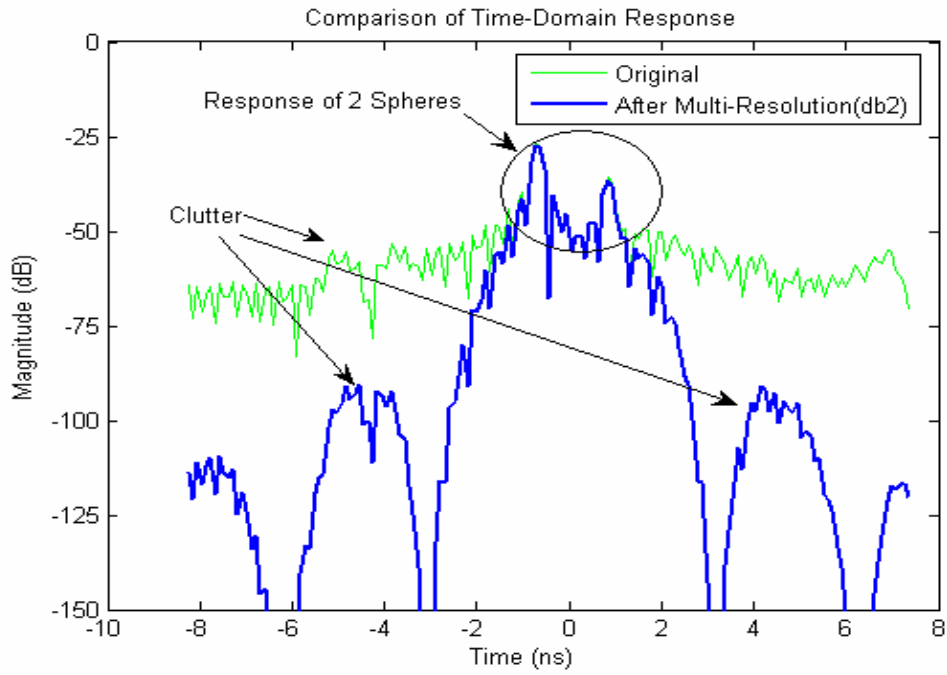


Figure 4.18 Time-Domain Response (azimuth of 0 degrees) for Test Set 1 after Considering Lower Resolutions (7-9) of Frequency Domain Data using db2

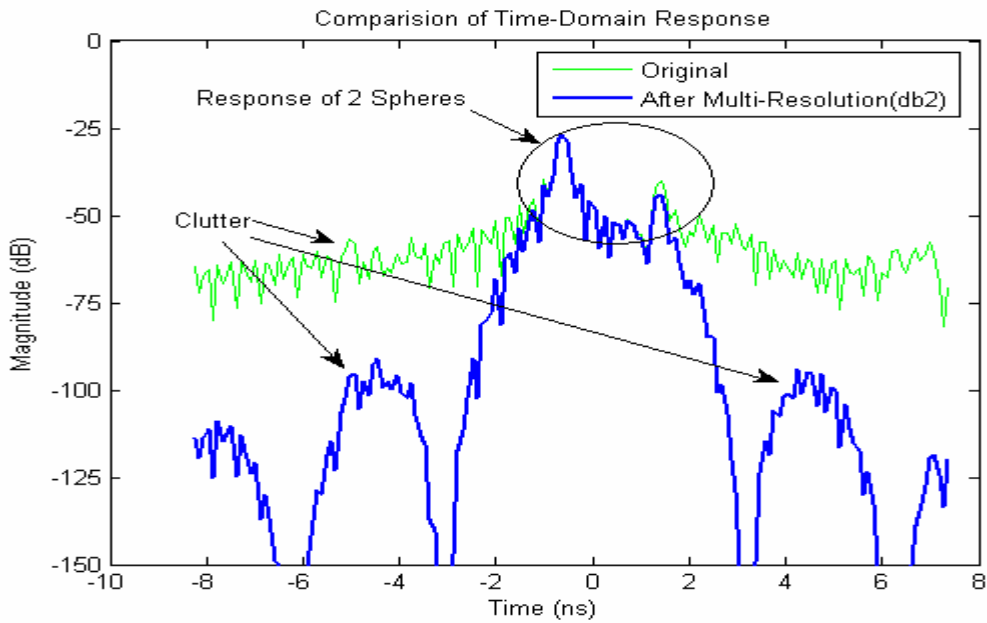


Figure 4.19 Time-Domain Response (azimuth of 50 degrees) for Test Set 1 after Considering Lower Resolutions (7-9) of Frequency Domain Data using db2

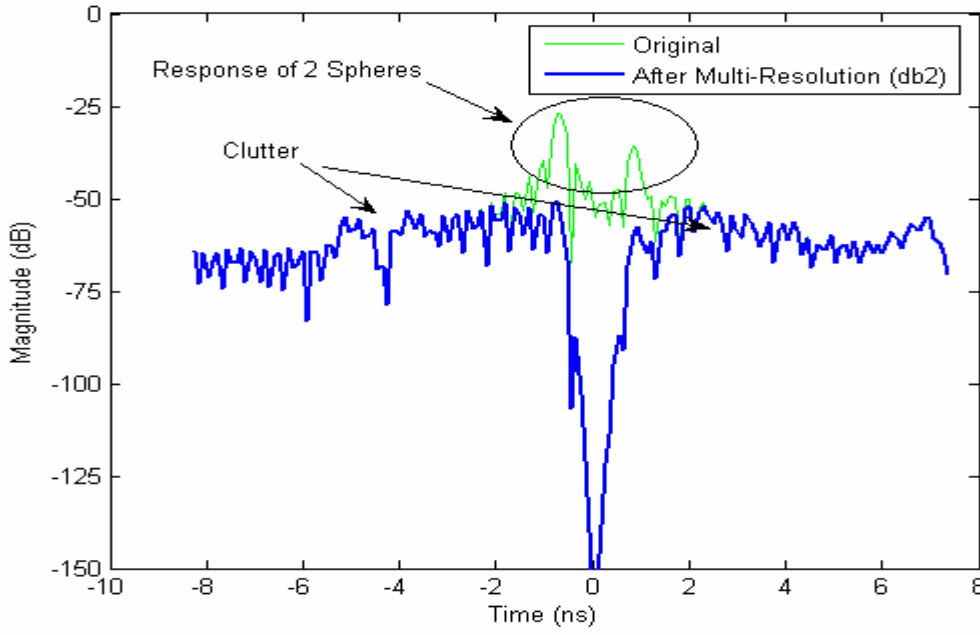


Figure 4.20 Time-Domain Response (azimuth of 0 degrees) for Test Set 1 after Considering Higher Resolutions (1-6) of Frequency Domain Data using db2

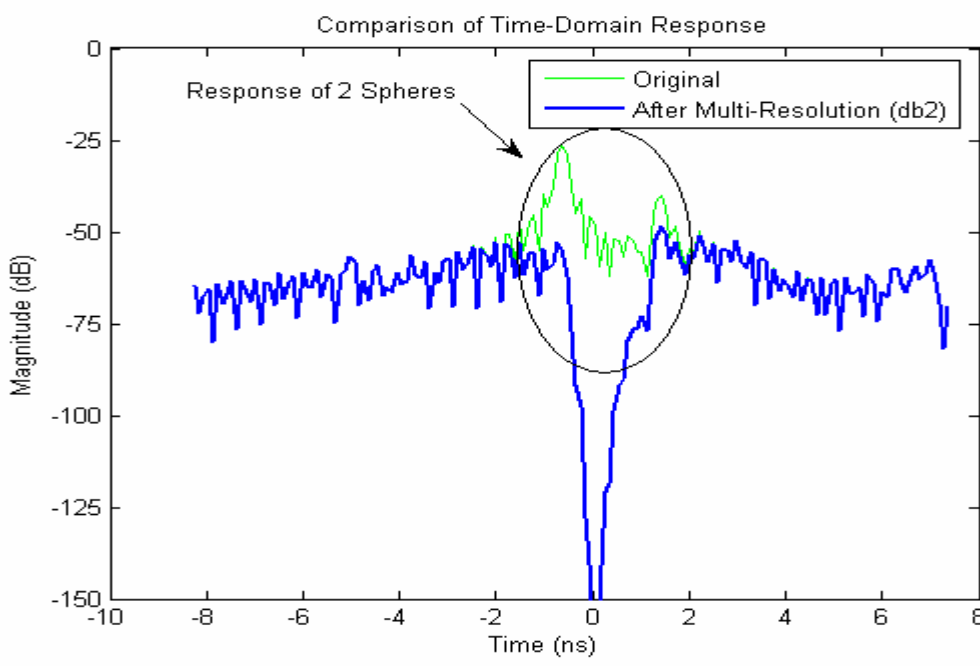


Figure 4.21 Time-Domain Response (azimuth of 50 degrees) for Test Set 1 after Considering Higher Resolutions (1-6) of Frequency Domain Data using db2

As shown before, figure 4.3 shows the generated image of the targets in test set-1 using ISAR imaging algorithm. The effects of different interactions can be clearly seen from this figure. From figures 4.20 and 4.21, it can be seen that the higher resolutions of the frequency domain data should correspond to late arrivals or non point returns. This can be verified from figure 4.22. Figure 4.22 shows the generated image of the targets in test case 1 after considering higher resolutions (1-6) of the frequency domain data.

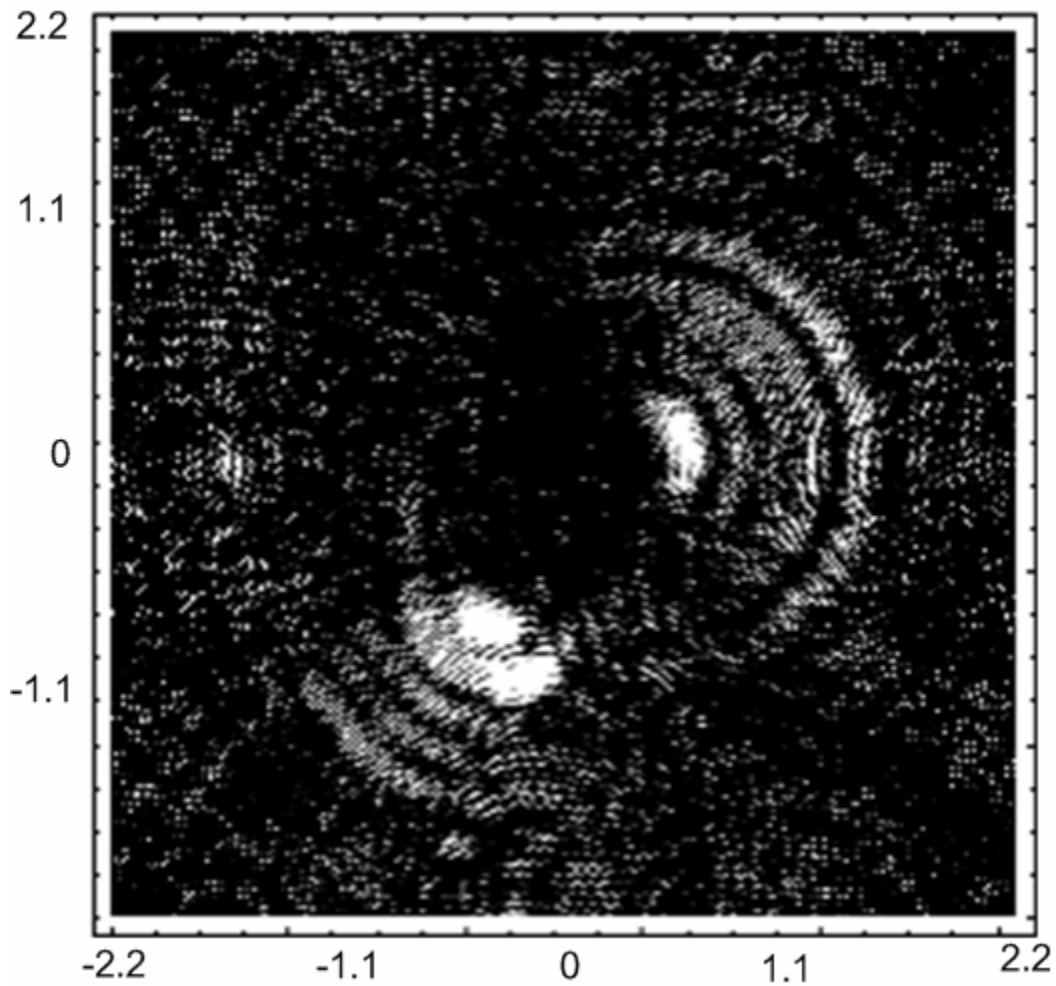


Figure 4.22 Generated ISAR Image of Test set 1 after Selecting Resolutions (1-6) of the Frequency Domain Data

It can be clearly seen from the above figure that higher resolutions correspond to late arrivals. Similarly, figure 4.23 shows the generated image for test set-1 after considering lower resolutions (7-9). From figures 4.18 and 4.19, it can be seen that these resolutions correspond to the target or early arrivals. Thus choosing only these resolutions will help to reduce the effect of other interactions and also clutter.

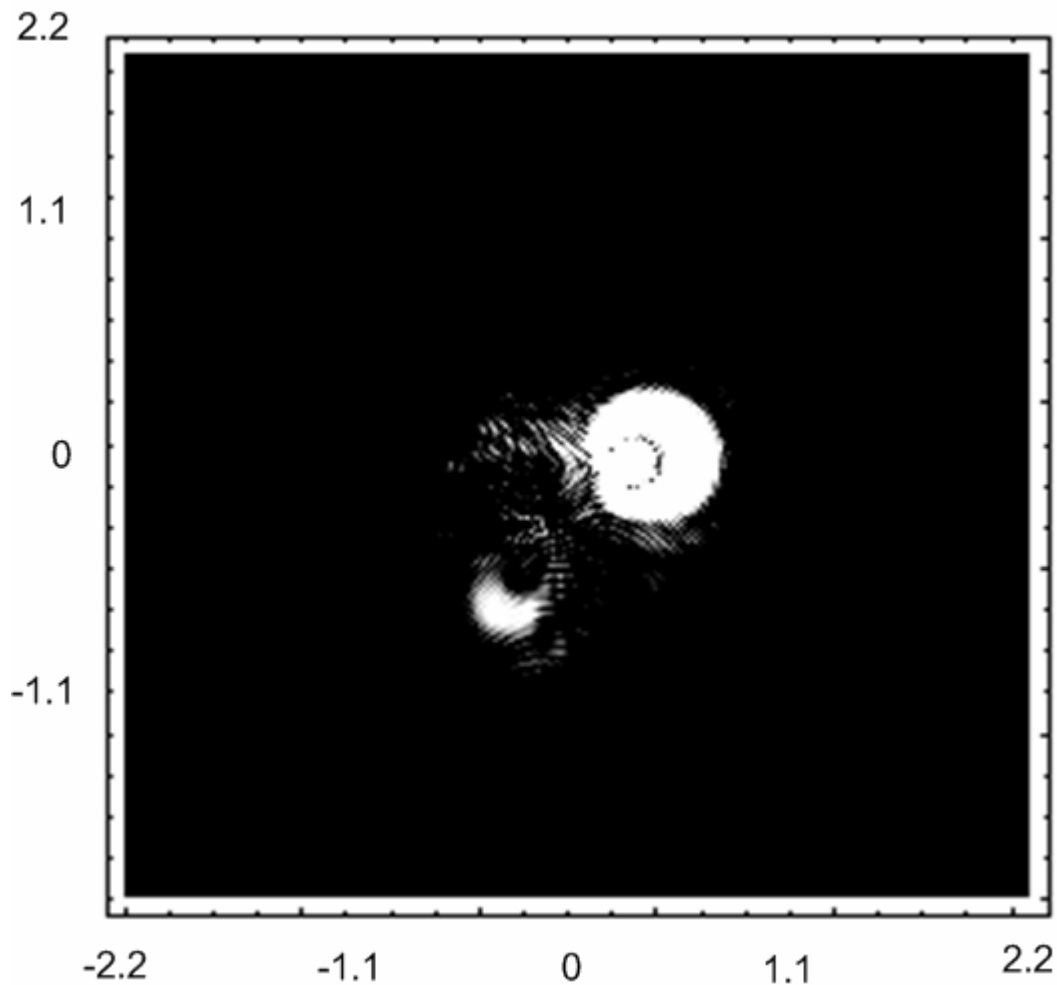


Figure 4.23 Generated ISAR Image of Test set 1 after Selecting Resolutions (7-9) of the Frequency Domain Data

For test set 2, Daubechies (db2) wavelets were used for simplicity. The frequency domain data was again divided into 10 resolutions or details, the first being the most high frequency detail. Figure 4.24 shows a comparison of the original time-domain data and the time-domain data obtained after selecting lower resolutions (7, 8) of the frequency domain data. This set of data is for an azimuth of 50 degrees. It can be clearly seen that the effect of clutter in the time-domain data has been reduced to quite

an extent. The minimum suppression of the clutter as compared to the original data is about 25 dB. It can also be seen that there is no change in the magnitude of the data which corresponds to the target. The magnitude of the target response in the original time-domain data and that after wavelet application in frequency domain is same. Again, only clutter is reduced to a great extent. This can be verified again from figure 4.25 which shows the same comparison for an azimuth of 70 degrees. Figures 4.26, 4.27 show the effect of selecting higher resolutions (1-6) of the frequency domain data (for azimuth angles of 50 and 70 degrees respectively). It can be seen that the magnitude of clutter in the time-domain is same for the original data and that after wavelet application. For these higher resolutions, the magnitude of the target is very low after wavelet application which shows that higher resolutions correspond to clutter and other interactions. Figures 4.28, 4.29 show the effect of selecting the lowest resolution (9) of the frequency domain data (for an azimuth of 50 and 70 degrees respectively). It can be seen that even this resolution does not correspond to the target and hence can be safely removed to obtain a better image. All the above mentioned figures have been truncated for better clarity and do not represent the whole time-domain signal. It has to be noted that the effect of different wavelets on the time domain data and the generated ISAR images is outside the scope of this chapter and will be discussed in detail in chapter 5.

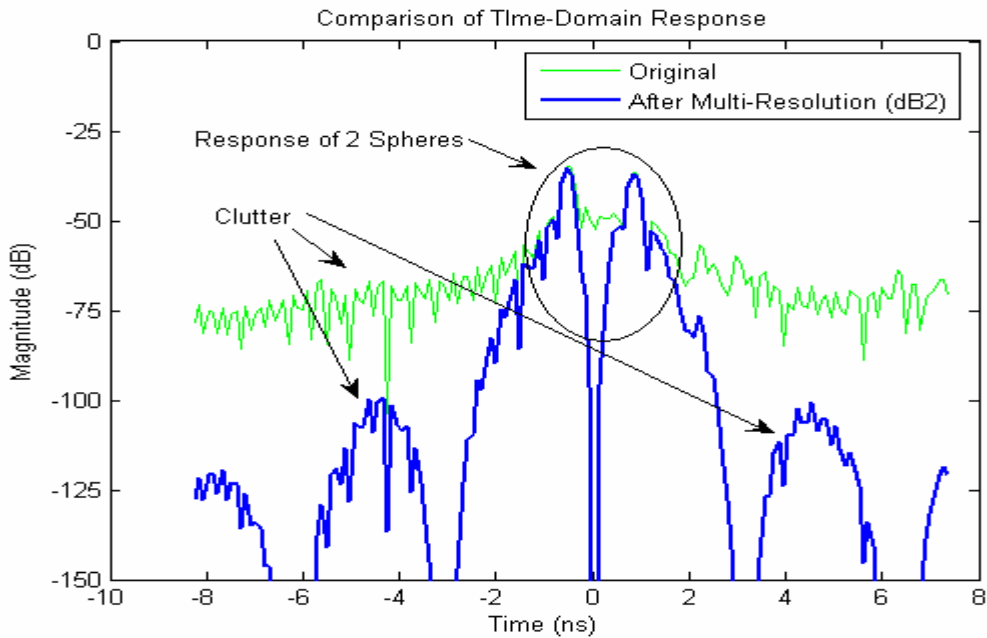


Figure 4.24 Time-Domain Response (azimuth of 50 degrees) for Test Set 2 after Considering Lower Resolutions (7, 8) of Frequency Domain Data using db2

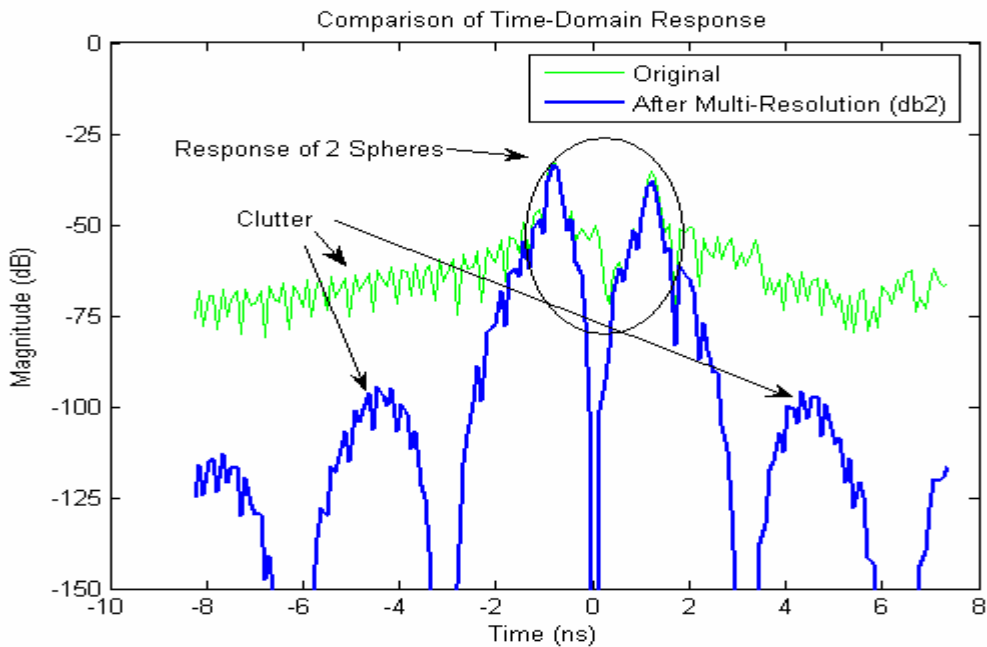


Figure 4.25 Time-Domain Response (azimuth of 70 degrees) for Test Set 2 after Considering Lower Resolutions (7, 8) of Frequency Domain Data using db2

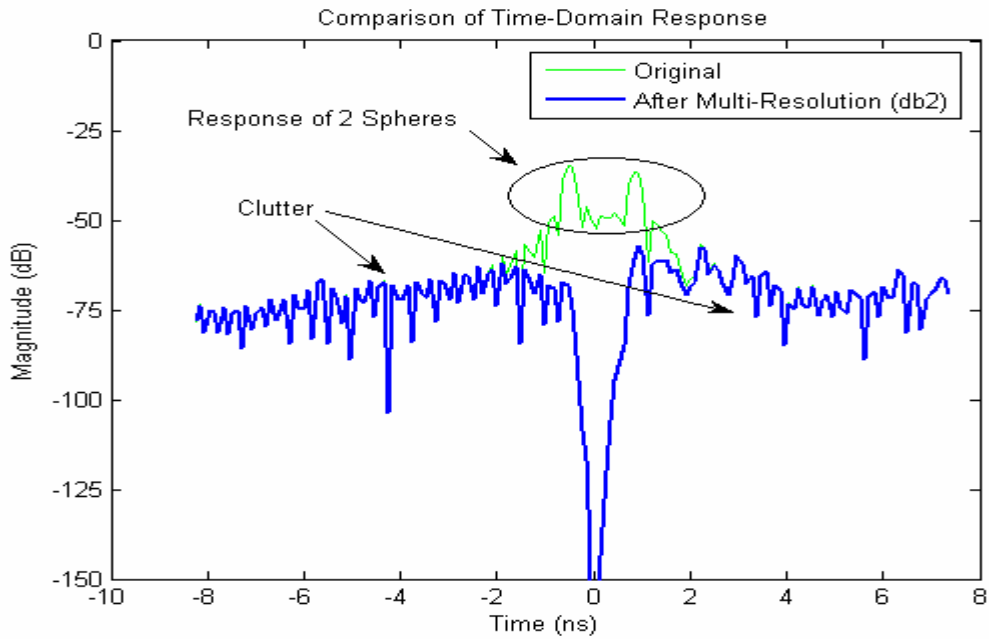


Figure 4.26 Time-Domain Response (azimuth of 50 degrees) for Test Set 2 after Considering Higher Resolutions (1-6) of Frequency Domain Data using db2

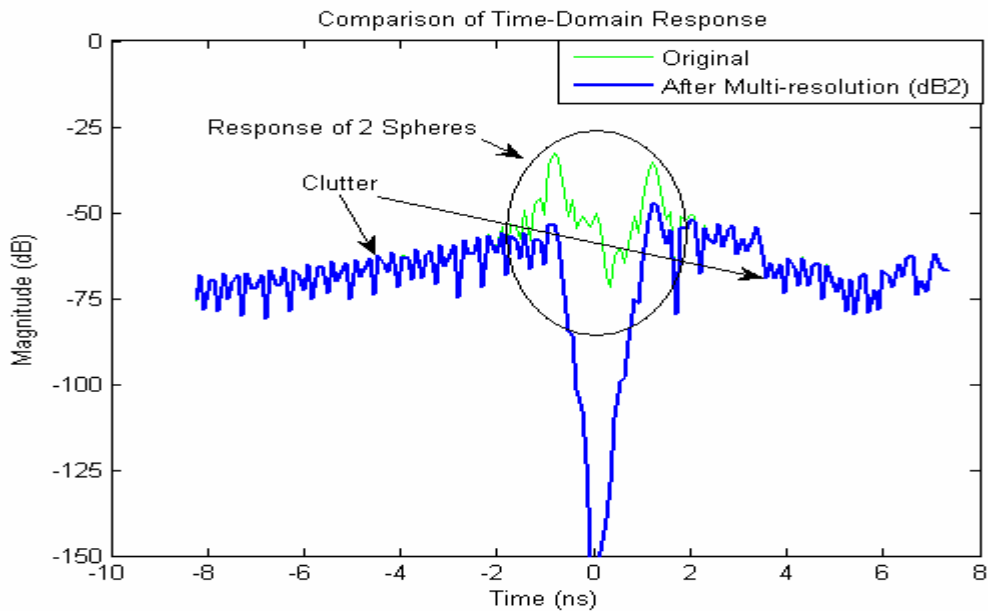


Figure 4.27 Time-Domain Response (azimuth of 70 degrees) for Test Set 2 after Considering Higher Resolutions (1-6) of Frequency Domain Data using db2

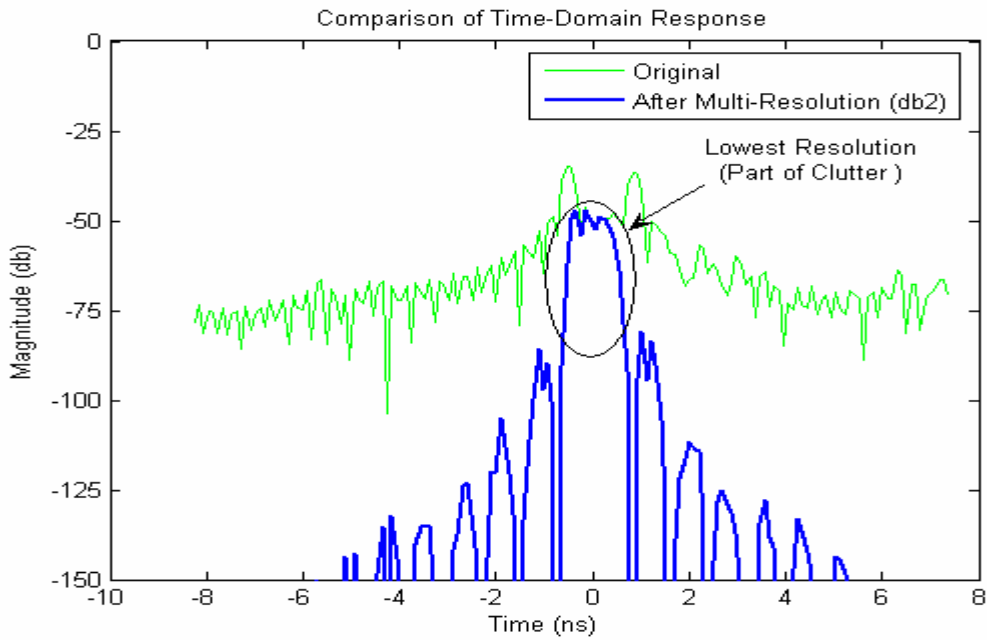


Figure 4.28 Time-Domain Response (azimuth of 50 degrees) for Test Set 2 after Considering Lowest Resolution (9) of Frequency Domain Data using db2

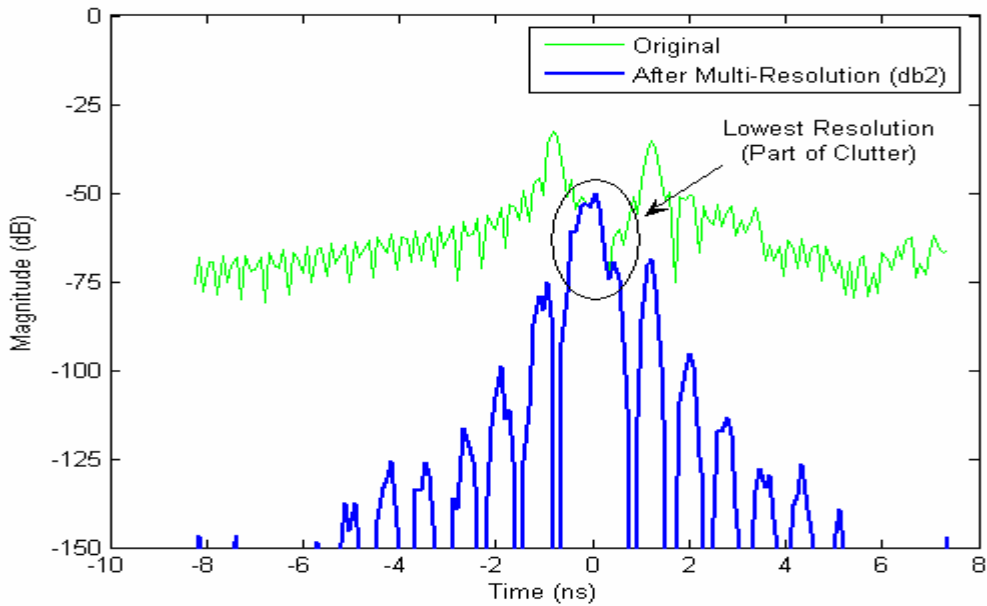


Figure 4.29 Time-Domain Response (azimuth of 70 degrees) for Test Set 2 after Considering Lowest Resolution or (9) of Frequency Domain Data using db2

As shown before, figure 4.4 shows the generated image of the target in test set 2 using ISAR imaging algorithm. The effects of different interactions can be clearly seen from this figure. From figures 4.26 and 4.27, it can be seen that these higher resolutions should correspond to late arrivals or non point returns. This can be verified from figure 4.30 which shows the generated image of the targets in test case 2 after considering higher resolutions (1-6) of the frequency domain data.

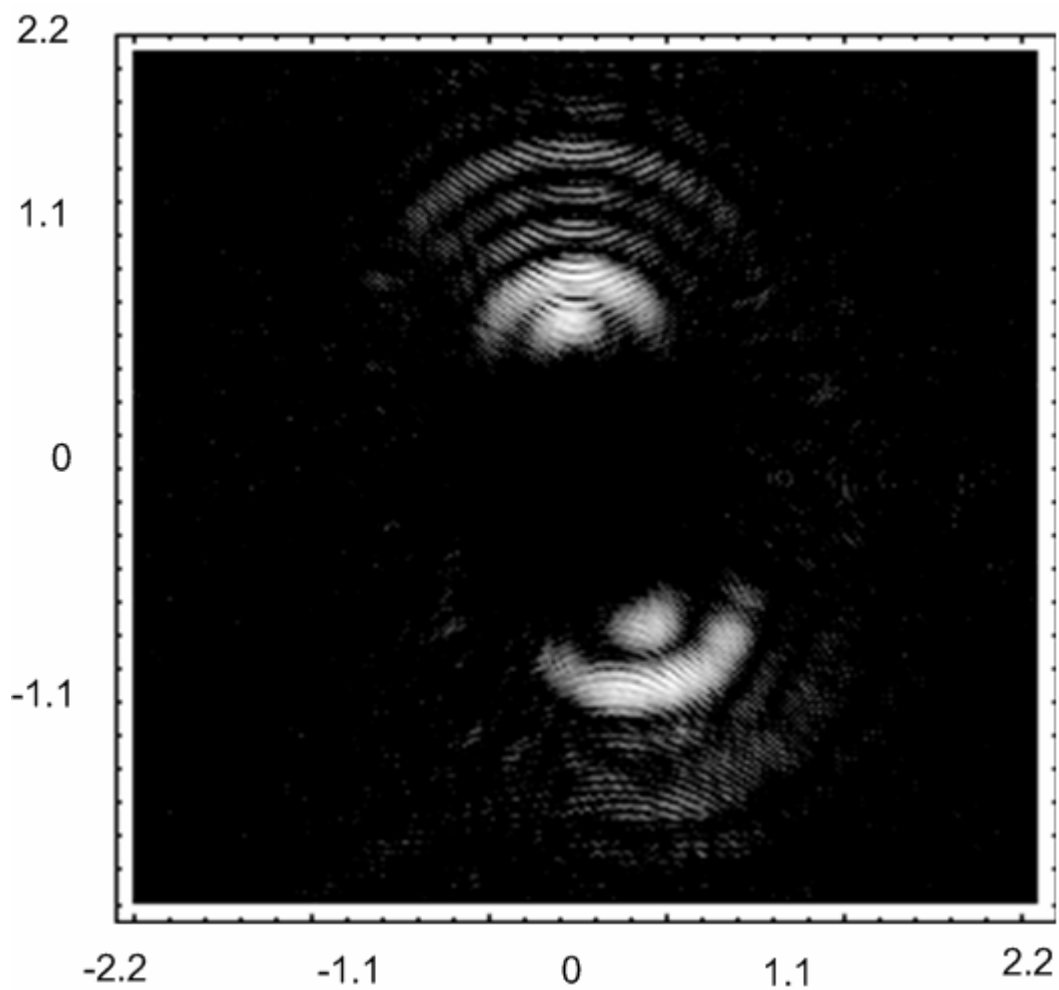


Figure 4.30 Generated ISAR Image of Test Set 2 after Selecting Resolutions (1-6) of the Frequency Domain Data

It can be clearly seen from the above figure that higher resolutions correspond to late arrivals. Similarly, figure 4.31 shows the generated ISAR image for test set 2 after considering lower resolutions (7, 8). From figures 4.24 and 4.25, it can be seen that these resolutions correspond to the target or early arrivals. Thus choosing only these resolutions will help to reduce the effect of other interactions and also clutter.

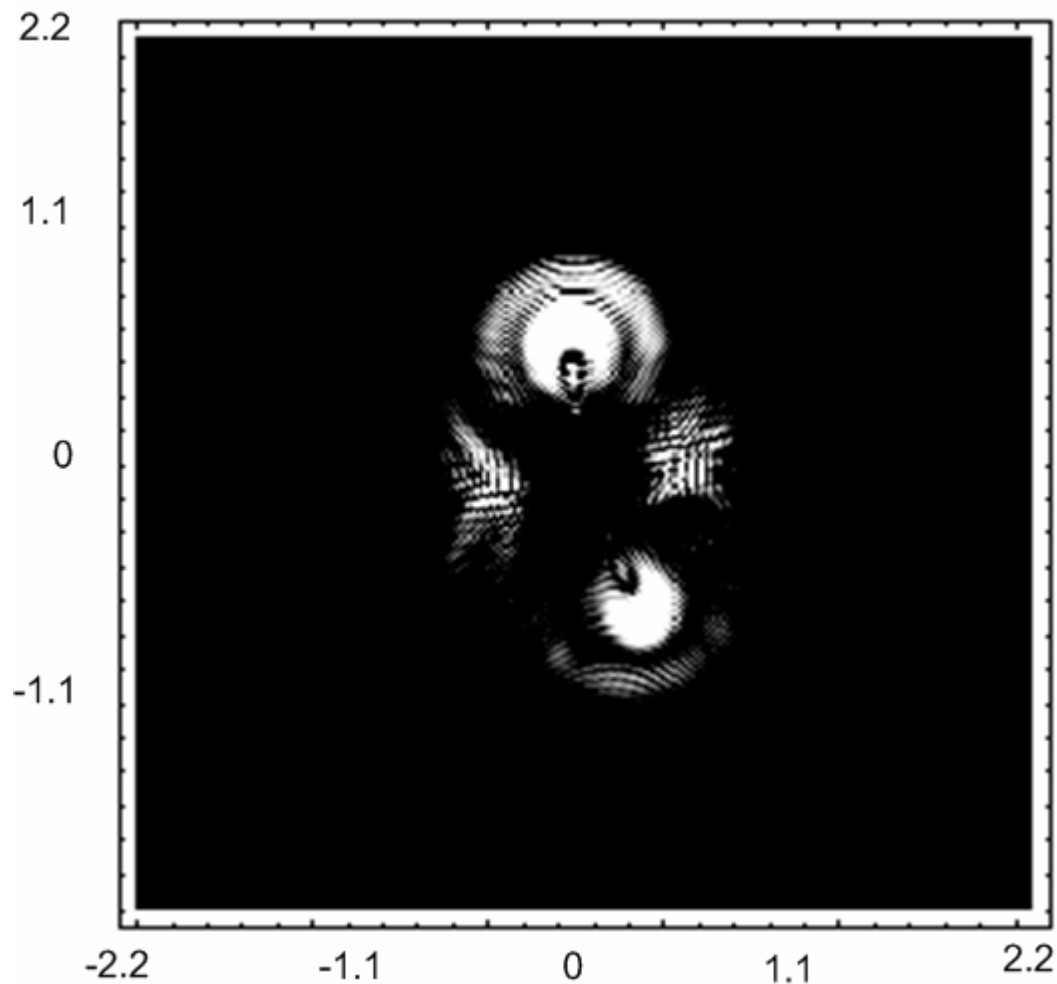


Figure 4.31 Generated ISAR Image of Test Set 2 after Selecting Resolutions (7, 8) of the Frequency Domain Data

Figure 4.32 is the generated image for test set 2 after considering the lowest resolution (9) of the frequency domain data. From figures 4.28 and 4.29, it can be seen that these resolutions correspond the clutter which occurs between the targets. This can be verified from figure 4.32 which shows this effect.

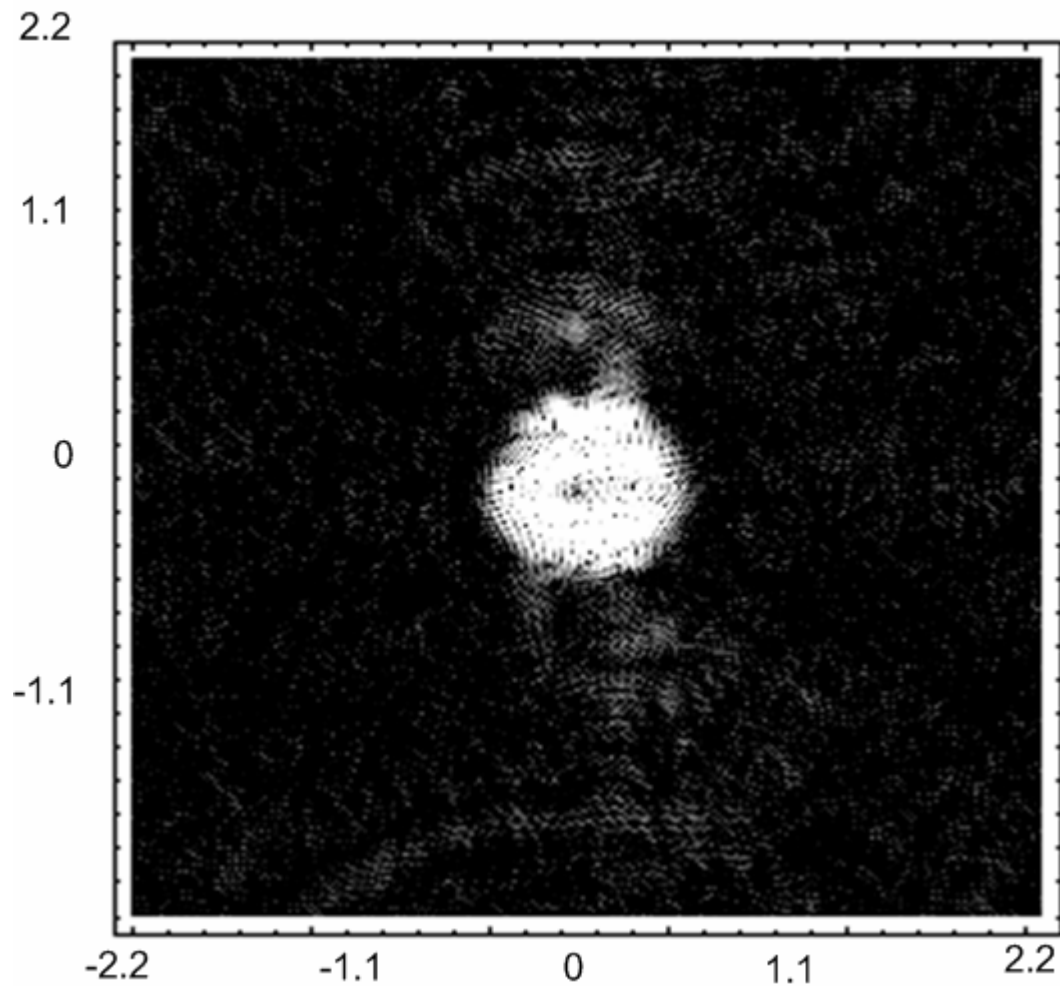


Figure 4.32 Generated ISAR Image of Test Set 2 after Selecting the Lowest Resolution (9) of the Frequency Domain Data

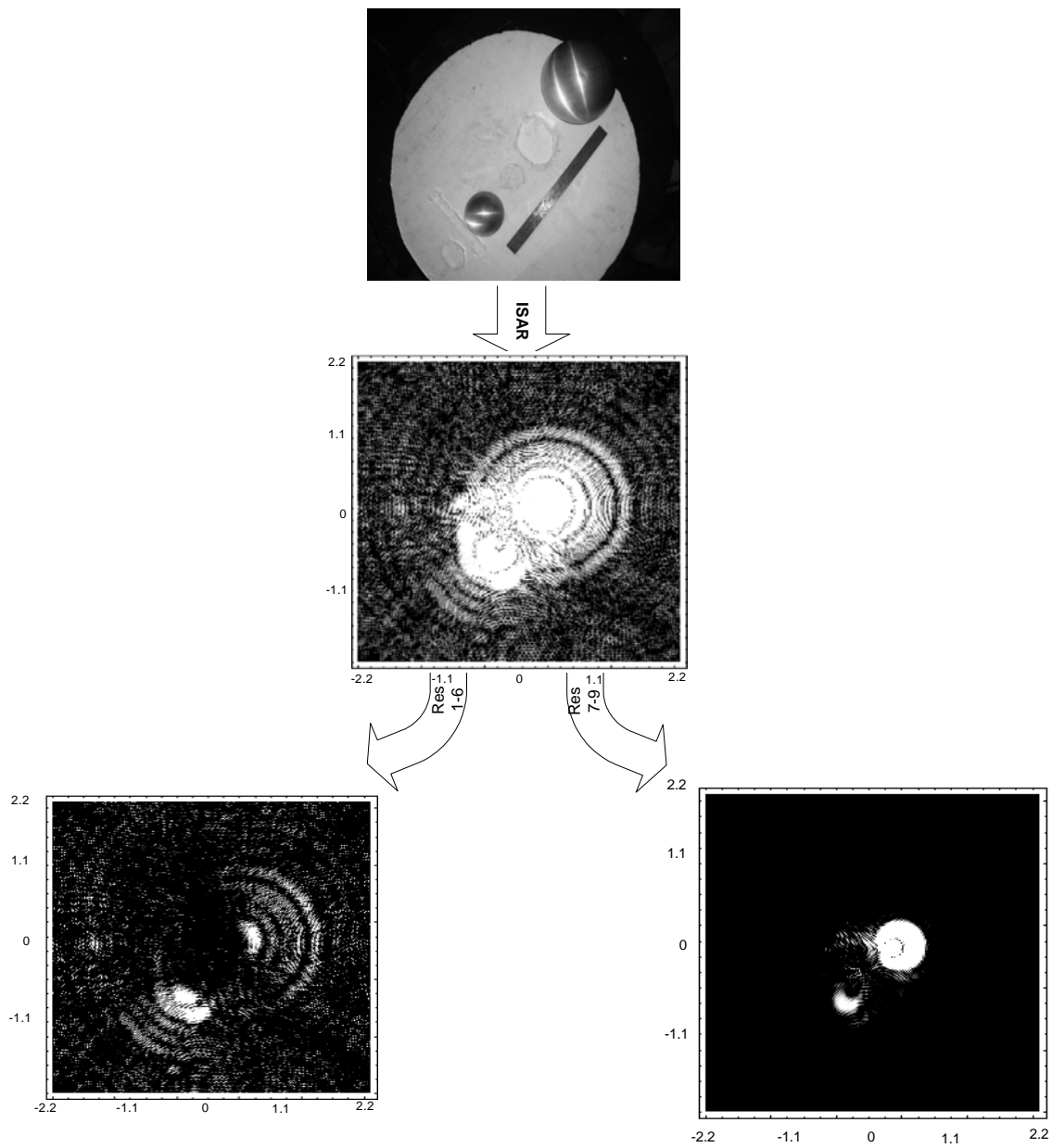


Figure 4.33 A Summary of Multi-Resolution Analysis for Test Set 1

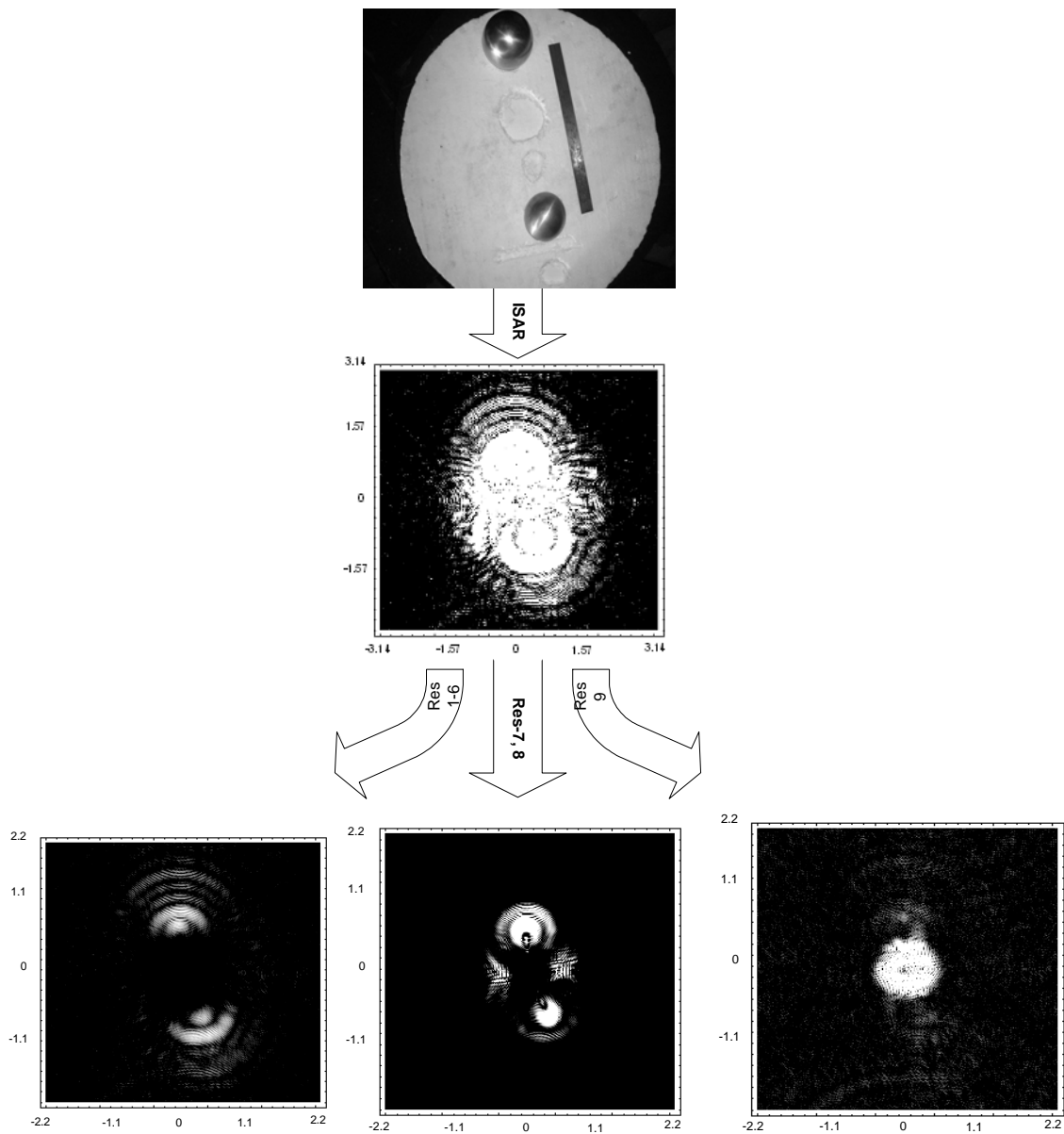


Figure 4.34 A Summary of Multi-Resolution Analysis for Test Set 2

Figures 4.33 and 4.34 give a summary of how multi-resolution can be used to separate different interactions in time. Multi-Resolution aided by wavelets can be used to reduce different interactions which are dispersive in nature and thereby increase the quality of the generated images.

CHAPTER 5

RESULTS AND DISCUSSIONS

Chapter 4 presented a detailed discussion on how wavelets can be used to achieve multi-resolution on frequency domain data and relate these different resolutions to different arrival times. This chapter presents a detailed discussion on the effect of support length of the wavelets used, the types of wavelets used and also cases where multi-resolution analysis can be used for other kinds of complex targets.

5.1 Effect of Wavelet Support Size

In this section, a discussion on the effect of the wavelet support size on multi-resolution analysis is presented. In chapter 4, Daubechies (db2) wavelets were used for simplicity. It is known in the signal processing community that increasing the length of the filter can give a smoother transition band or a comparatively lower sideband power. Even in the case of multi-resolution using wavelets, it can be said from intuition that increasing the support length of a wavelet can result in sidebands (clutter) with comparatively lower power or in other words a better suppression of clutter. This hypothesis is supported by experimental results. We use side lobe suppression as a metric to evaluate the performance this multi-resolution analysis which can be defined as follows:

$$\begin{aligned} \text{Sidelobe Suppression}(SP) = & \text{abs} (\text{Mag of Mainlobe (in dB)} \\ & - \text{Mag of First Sidelobe (in dB)}) \quad (5.1) \end{aligned}$$

5.1.1 Results for Test Set 1

Figure 5.1 shows the response of the original time-domain data and the data obtained by selecting resolutions 7-9 of the frequency domain data. Daubechies 1 (db1) wavelets were used to obtain multi-resolution. It can be seen that the side lobe suppression using db1 (filter length of 2) is 60 dB.

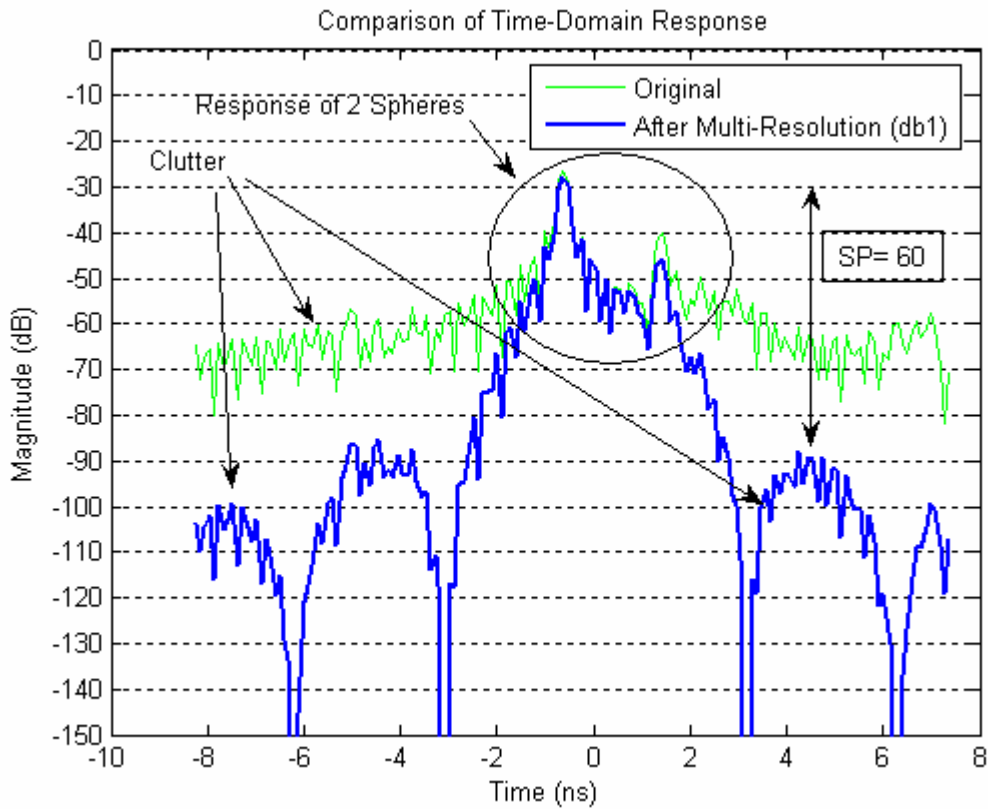


Figure 5.1 Time-Domain Response Comparison using db1

Figure 5.2 shows the response of the original time-domain data and the data obtained by selecting resolutions 7-9 of the frequency domain data. Daubechies 3 (db3) wavelets were used to obtain multi-resolution. It can be seen that the side lobe suppression using db3 (filter length of 6) is 70 dB.

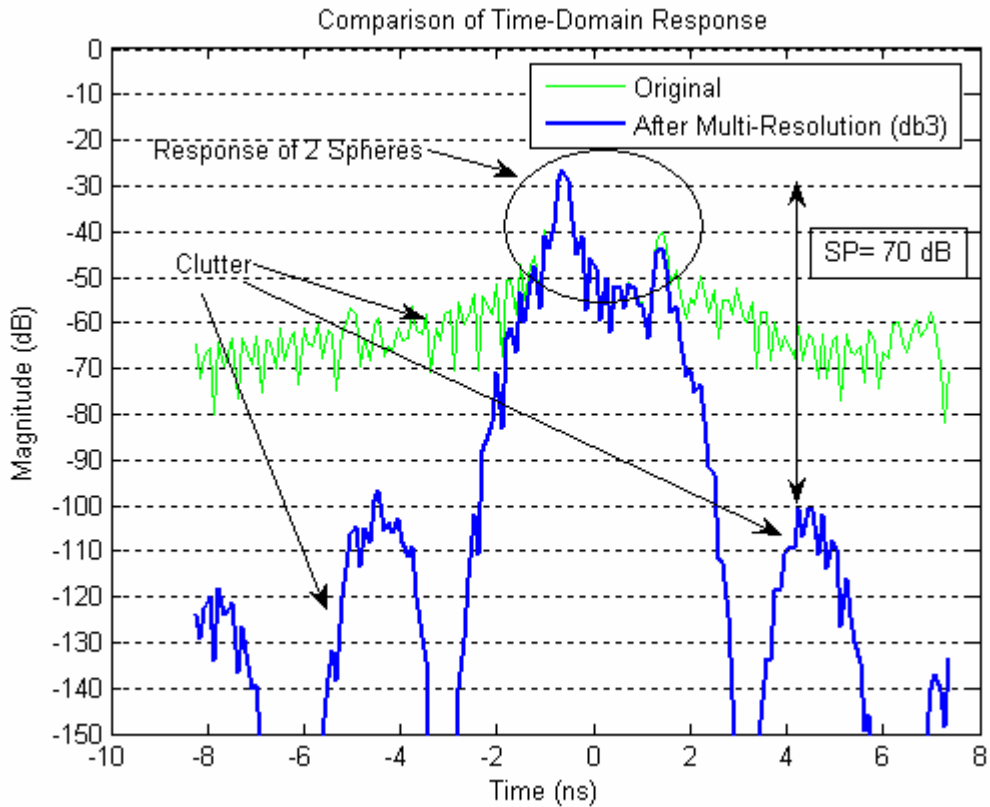


Figure 5.2 Time-Domain Response Comparison using db3

Figure 5.3 shows the response of the original time-domain data and the time-domain data obtained by selecting resolutions 7-9 of the frequency domain data. Daubechies 6 (db6) wavelets were used to obtain multi-resolution. It can be seen that the side lobe suppression using db6 (filter length of 12) is 90 dB. From figures 5.1-5.3, it can be that increasing the support length increases the suppression ratio.

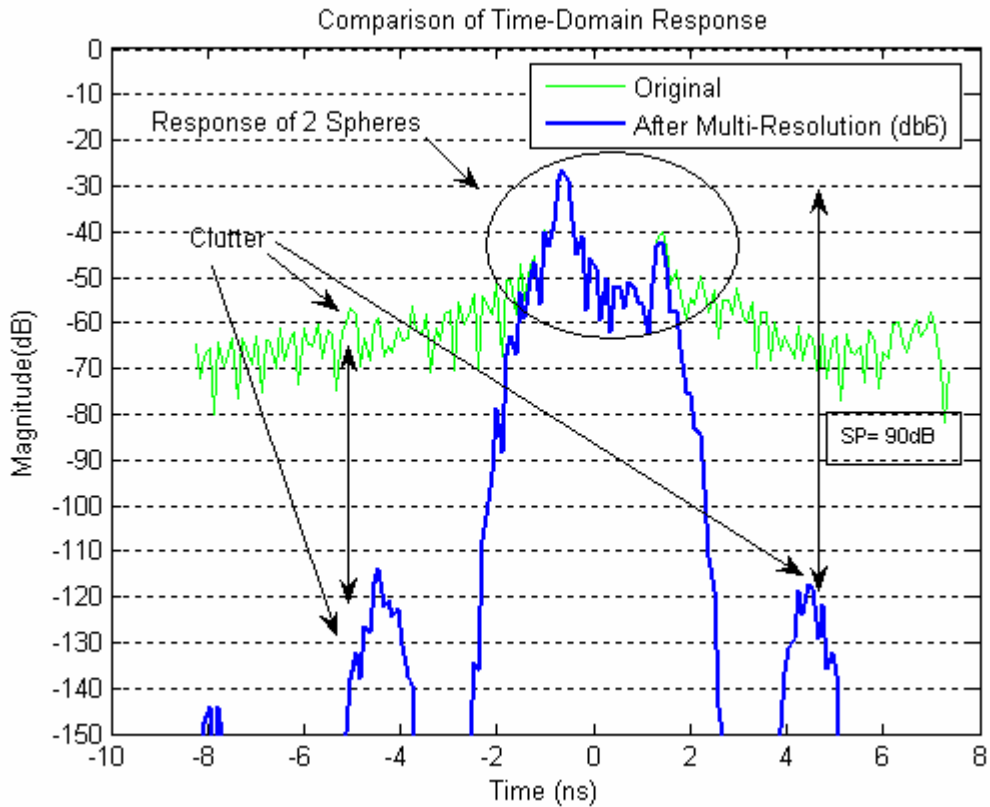


Figure 5.3 Time-Domain Response Comparison using db6

Figure 5.4 shows the time-domain response using Daubechies wavelets with different support sizes. From figures 5.1-5.4, it can be seen that as the wavelet support size increases, the magnitude of the side lobe decreases so does the width of the main lobe both of which are good from the clutter suppression point of view.

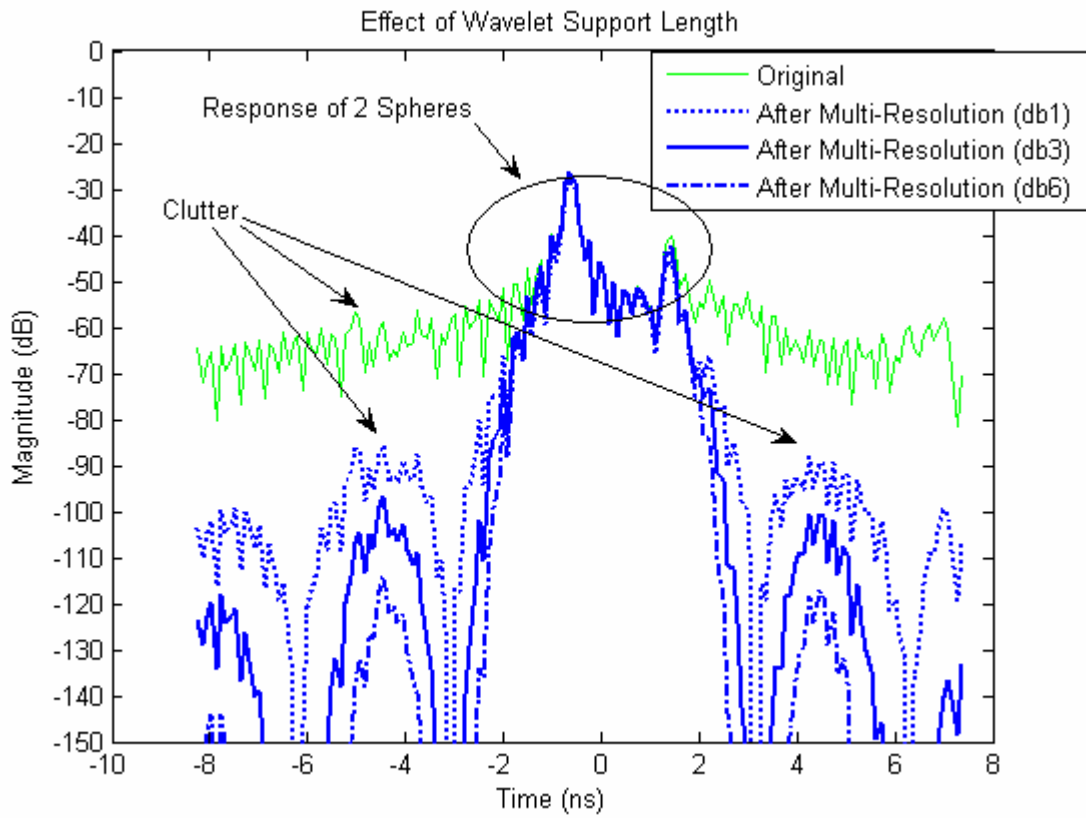


Figure 5.4 Time-Domain Response Comparison of different Wavelet Support Lengths for Daubechies Wavelets

Figure 5.5 shows the response of the original time-domain data and the data obtained by selecting resolutions 7-9 of the frequency domain data. Coif-lets 1 (Coif1) wavelets were used to obtain multi-resolution. It can be seen that the side lobe suppression using Coif1 (filter length of 6) is 65 dB.

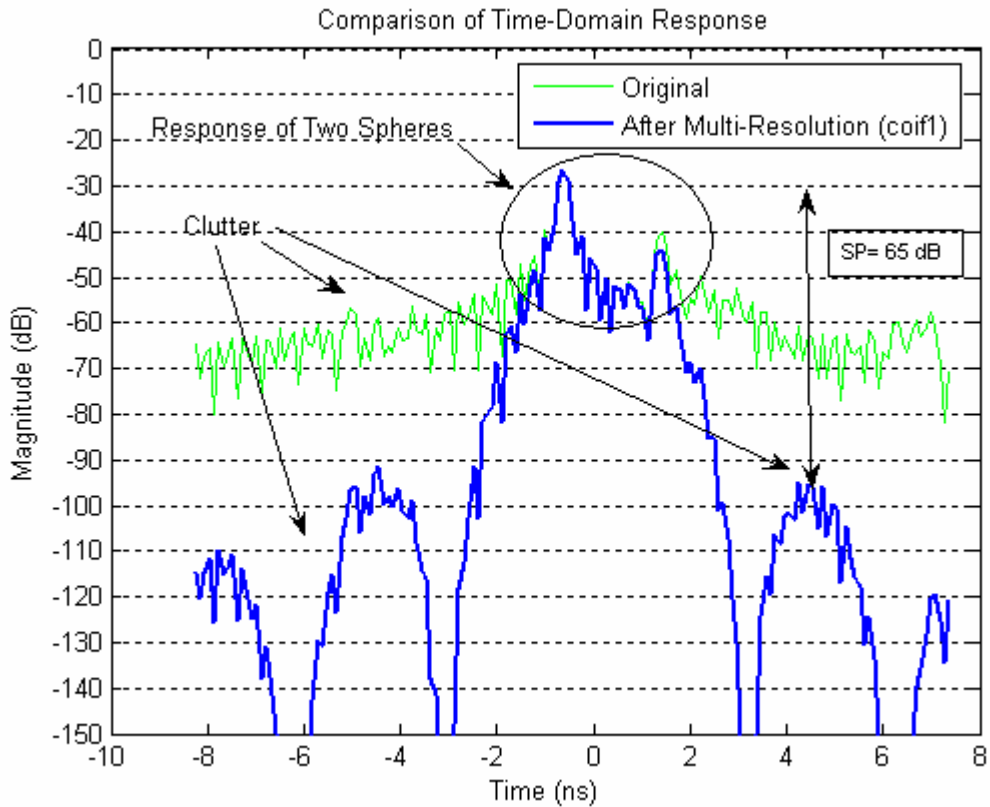


Figure 5.5: Time-Domain Response Comparison using Coif 1

Figure 5.6 shows the response of the original time-domain data and the data obtained by selecting resolutions 7-9 of the frequency domain data. Coif-lets 2 (Coif2) wavelets were used to obtain multi-resolution. It can be seen that the side lobe suppression using Coif2 (filter length of 12) is 80 dB. From figures 5.5 and 5.6, it can again be seen that increasing the support length gives a better clutter suppression factor.

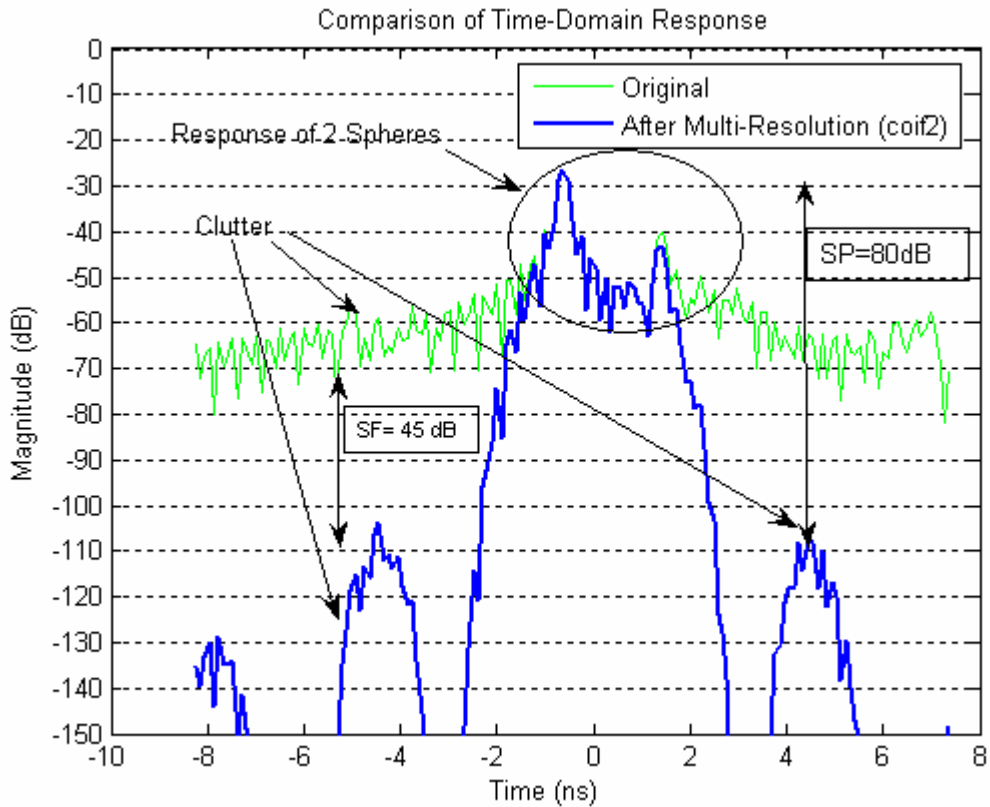


Figure 5.6 Time-Domain Response Comparison using Coif 2

Figure 5.7 shows the time-domain response using Coiflets with different support sizes. From figures 5.5-5.7, it can be again seen that as the wavelet support size increases, the magnitude of the side lobe decreases. Also, the width of the main lobe decreases with the support length which is good from clutter suppression point of view.

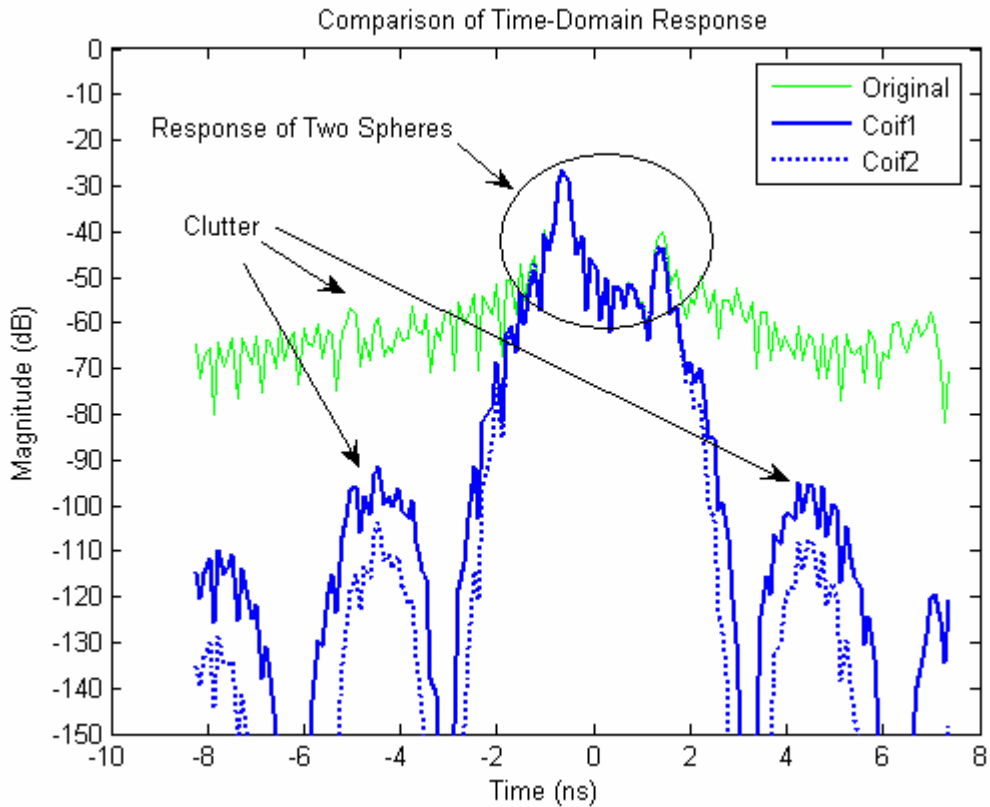


Figure 5.7 Time-Domain Response Comparison of different Wavelet Support Lengths for Coiflets

Table 5.1 shows the variation of side lobe suppression (SP) with the wavelet support size or the filter length. It can be consistently seen that this factor increases with increase in the filter length. The same fact can be verified from figure 5.8 which shows the variation of the suppression factor as a function of filter length.

Table 5.1 Side Lobe Suppression (SP) Variation with Filter Length

Wavelet Type	Filter Length	Suppression Factor (dB)
Daubechies (db1)	2	55
Daubechies (db2)	4	60
Daubechies (db3)	6	70
Daubechies (db4)	8	80
Daubechies (db6)	12	90
Daubechies (db8)	16	100
Daubechies (db10)	20	110
Coiflets (Coif1)	6	65
Coiflets (Coif2)	12	80

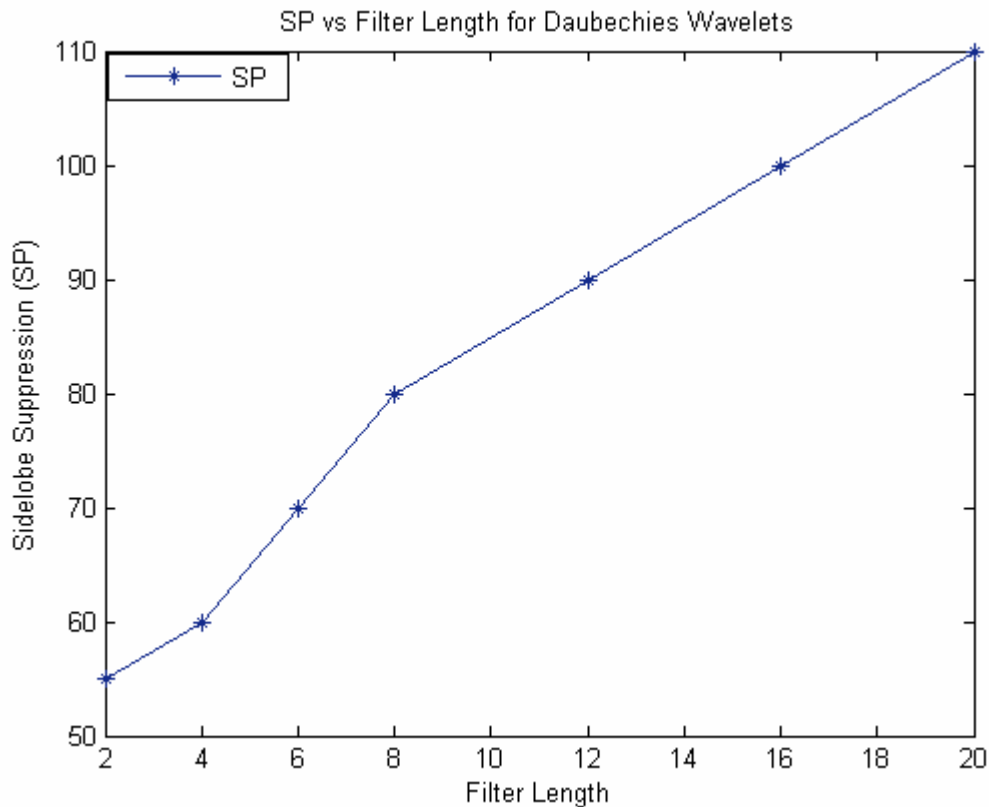


Figure 5.8 Variation of Side Lobe Suppression (SP) as a Function of Filter Length

5.2 Effect of Wavelet Type

This section presents results discussing the effect of wavelet type on the suppression ratio. To make a fair comparison, the filter length of the wavelets to be compared is kept constant. For this study, Daubechies and Coiflets were used for comparison. It has to be noted that the filter length of Coiflets of order N has thrice the filter length of Daubechies wavelets of order N . In other words, it can be said that Coiflets of order N have the same filter length of Daubechies of order $3N$. Figure 5.9 shows the time-domain response using Coiflets 1 (Coif1) and Daubechies 3 (db3).

It can be seen that the performance of these wavelets is almost same except for the fact that Daubechies has a slightly higher suppression factor as compared to

Coiflets. This fact can be verified again from Figure 5.10 which shows the comparison of the time-domain response using Daubechies 6 (db6) and Coiflets 2 (Coif2).

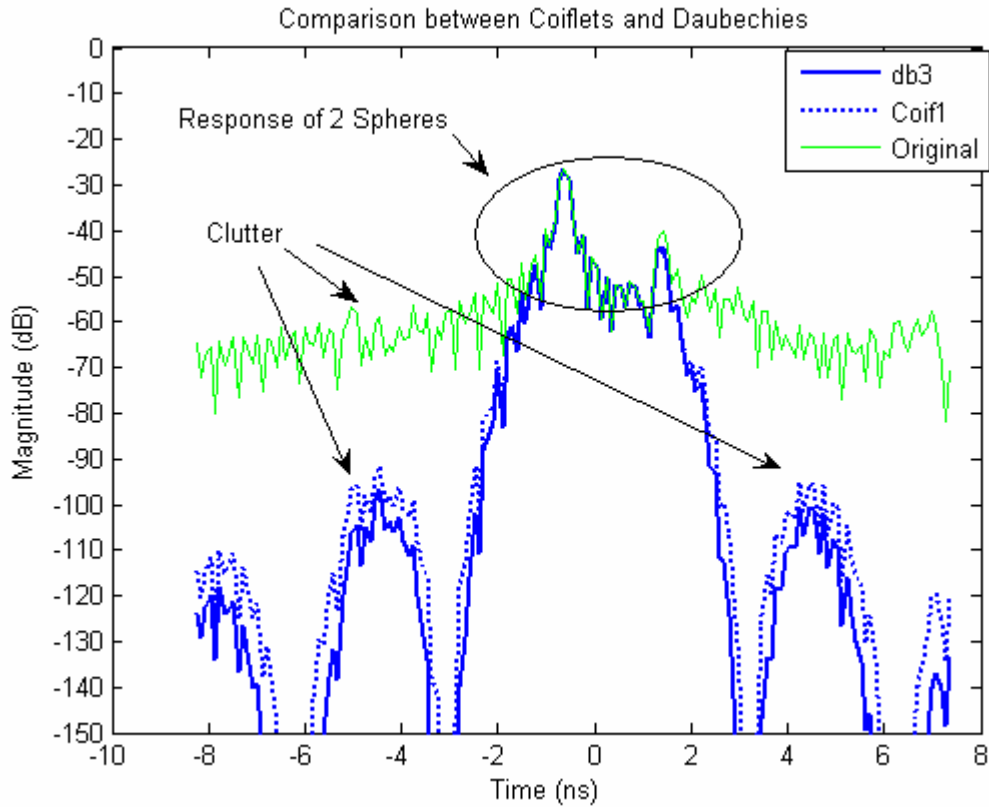


Figure 5.9 Comparison of Time-Domain Response of Daubechies (db3) and Coiflets (Coif1)

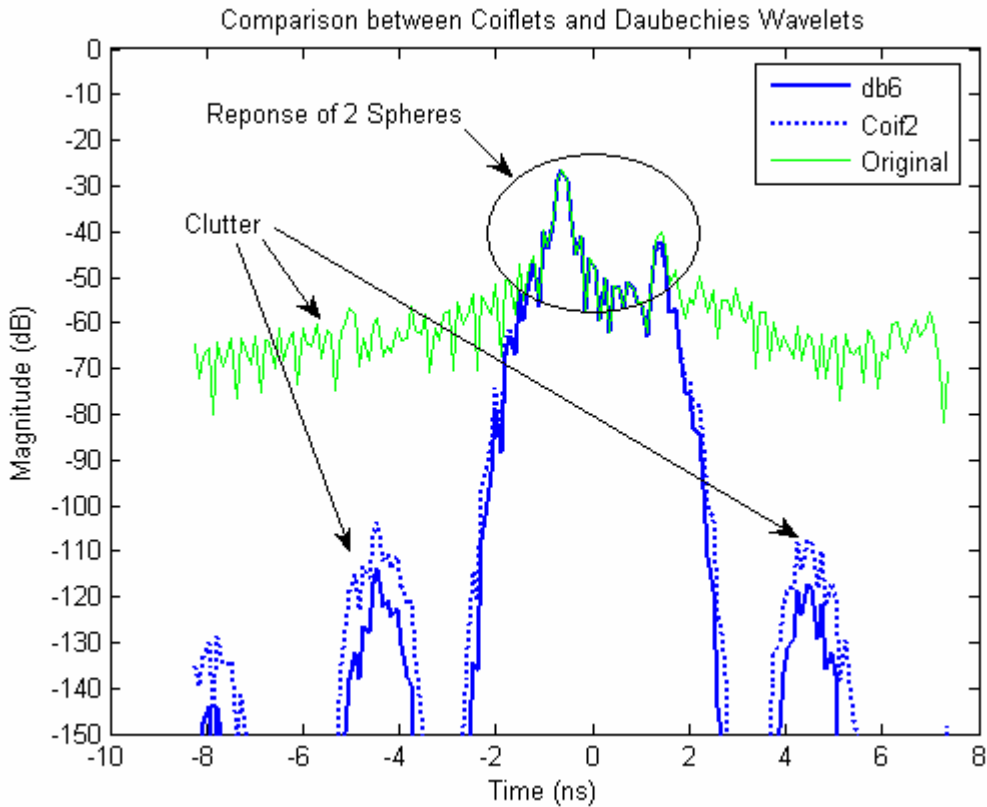


Figure 5.10 Comparison of Time-Domain Response of Daubechies (db6) and Coiflets (Coif2)

5.3 Analysis of Other Complex Targets

In this section, the multi-resolution analysis approach is used on some complex targets. In set up 3, a combination of three 6 inch rods is used to form a triangle shape and then buried inside sand. This is a case of sub-surface imaging where the target is buried inside soil, sand or other stuff. Figure 5.11 shows the time-domain response of the target for an azimuth of 50 degrees. The response of the target occurs at around 1.5 – 2.0 ns. The response after 2 ns till 8 ns is due to the plastic tub used in the experiment. It can be seen that in the magnitude of the response corresponding to the target is less comparable to that from the tub and in fact this magnitude is less than that

corresponding to the tub. This is a typical situation in the case of sub-surface imaging where the signal level of the target is pretty much same as that of the clutter. In other words the signal to clutter ratio for test set 3 is less as compared to that in test set 1 and 2. From intuition, it can be said that the generated image of this target setup will show the effect of clutter to quite an extent.

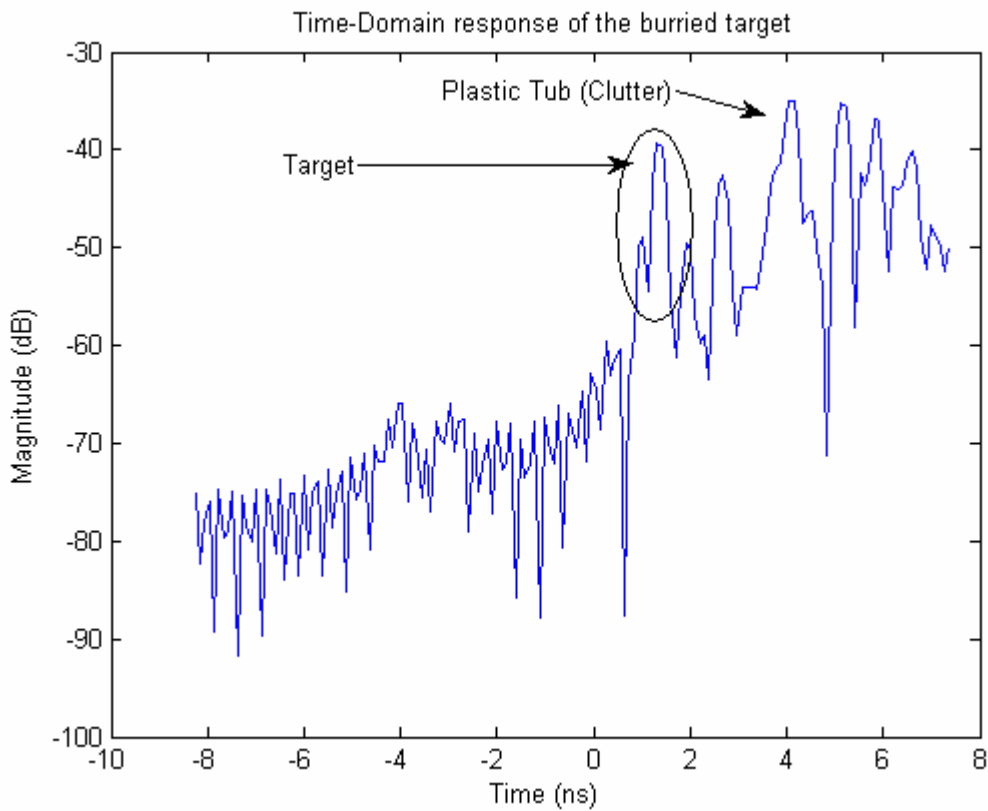


Figure 5.11 Range Profile (Time-Domain response) of Target in Setup 3 for an Azimuth of 50 degrees

Figure 5.12 shows the generated image of this target set up using ISAR imaging algorithm as discussed in chapter 4. It can be seen that there is quite a lot of clutter in the reproduced image and the intensity of this clutter is very high and comparable to

that of the target which is expected. As a result of this, target identification becomes a challenging task.

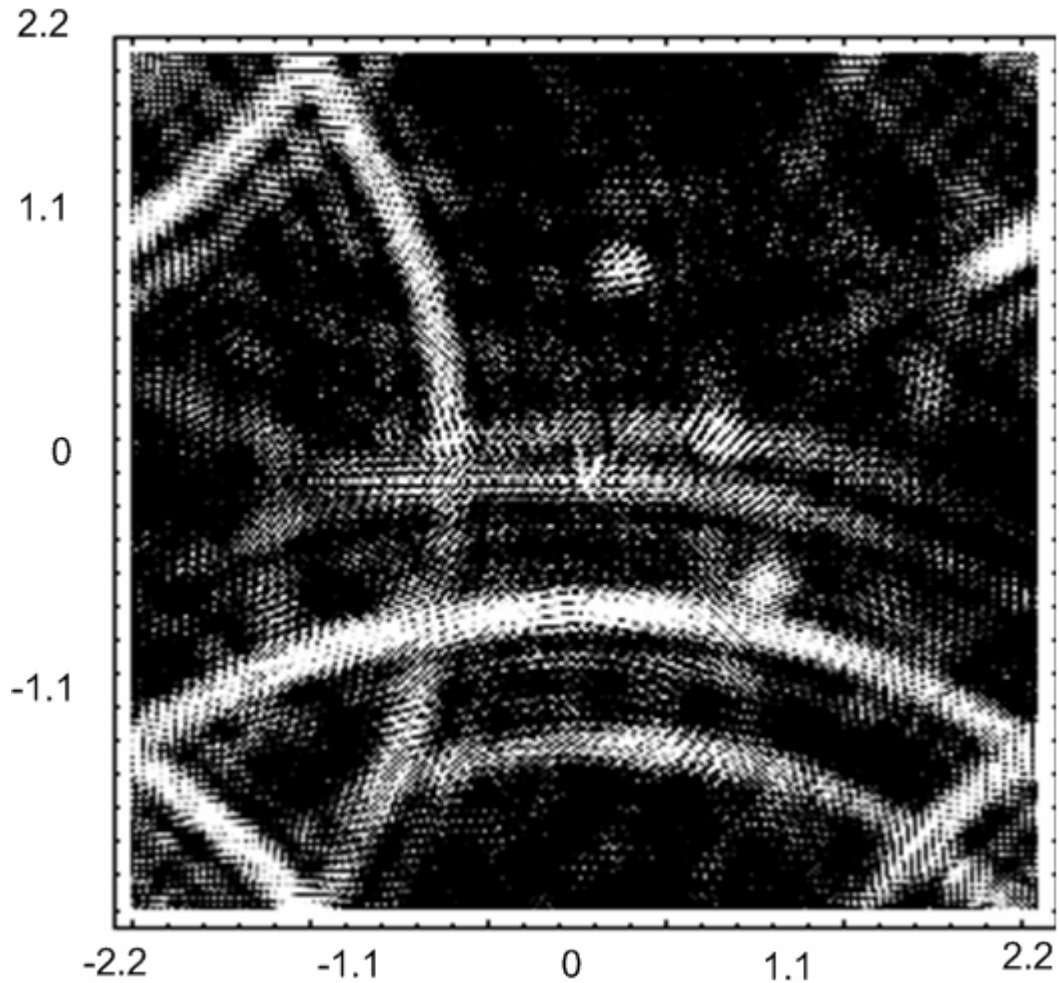


Figure 5.12 Generated ISAR Image of the Buried Target in Test Set 3 (3 rods arranged as triangle)

The effect of filter length on suppression of clutter was presented in section 5.1 and it was concluded that a higher filter length gave a better clutter suppression. Considering this fact into account, Daubechies 12 (db12) wavelets were used for this test set. The frequency domain data was divided into 8 resolutions or details, the first being the most high frequency detail. Figure 5.13 shows a comparison of the original

time-domain data and the time-domain data obtained after selecting higher resolutions (1-6) of the frequency domain data. This set of data is for an azimuth of 50 degrees. It can be clearly seen that this data corresponds to clutter since the target is located at around 1.5 ns. Thus resolutions 1-6 correspond to clutter in the time-domain response. Figure 5.14 shows the generated image by considering resolutions 1-6 of the frequency domain data. This image shows the effect of clutter.

Figure 5.15 shows a comparison of the original time-domain data and the time-domain data obtained after selecting lower resolutions (7-9) of the frequency domain data. This set of data is for an azimuth of 50 degrees. It can be clearly seen that for these resolutions the magnitude of the clutter corresponding to the plastic tub has been reduced by more than 70 dB. Thus the generated image of the target considering these resolutions should have negligible effect of the plastic tub. This can be verified from figure 5.16 which is the generated image after considering the above mentioned resolutions. This image still shows some interactions between the three rods. This can be attributed to the clutter which is present from -1ns to 1ns. Figure 5.17 is the time-domain response by considering resolutions 8, 9. It can be seen from the figure that this resolution corresponds to clutter which is present from -1ns to 1ns. Thus to get a better image of the target under consideration, these resolutions should also be ignored for imaging. Figure 5.18 shows the time-domain response obtained by considering only resolution 7. It can be seen that this resolution corresponds to that of the target. Thus, only resolution 7 is used to obtain the ISAR image of the target under consideration. Figure 5.19 is the image obtained after considering resolution 7 only. It can be seen that

the interactions occurring between the targets have been reduced in this image as compared to that of figure 5.16.

From the above results and discussions, it can be concluded that multi-resolution analysis can be used to separate different interactions in time. By using multi-resolution in frequency domain, a time resolution of 0.39 ns (for the test parameters used in this thesis) can be achieved.

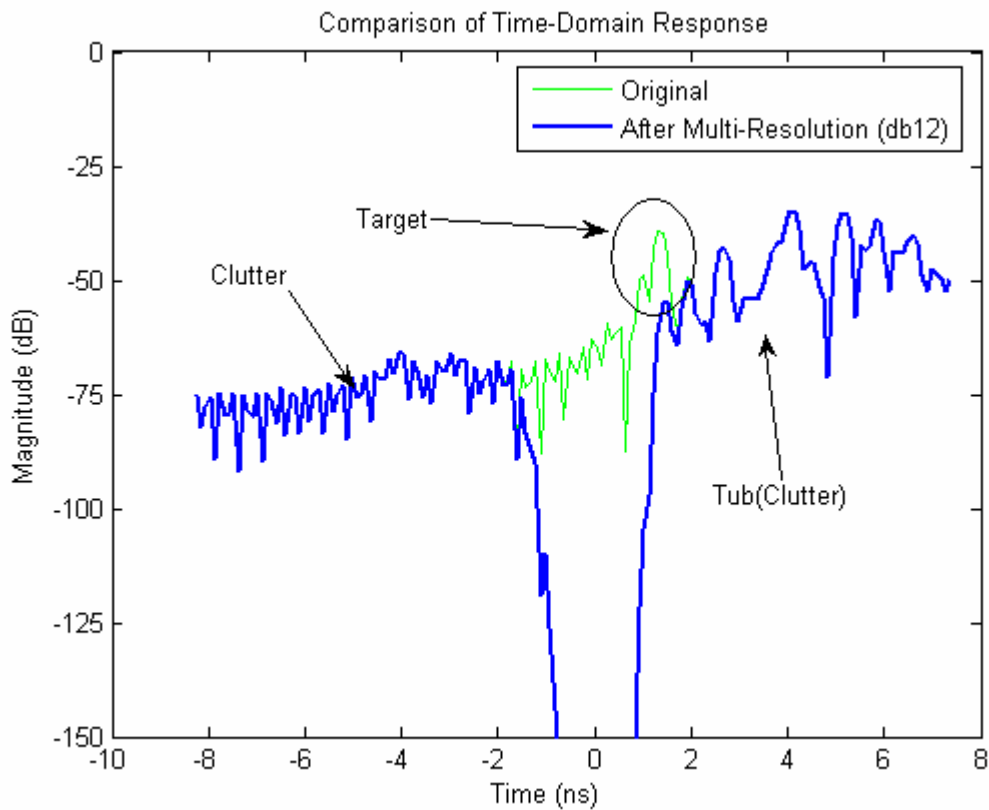


Figure 5.13 Time-Domain Response (azimuth of 50 degrees) for Test Set 3 after Considering Higher Resolutions (1-6) of Frequency Domain Data using db12

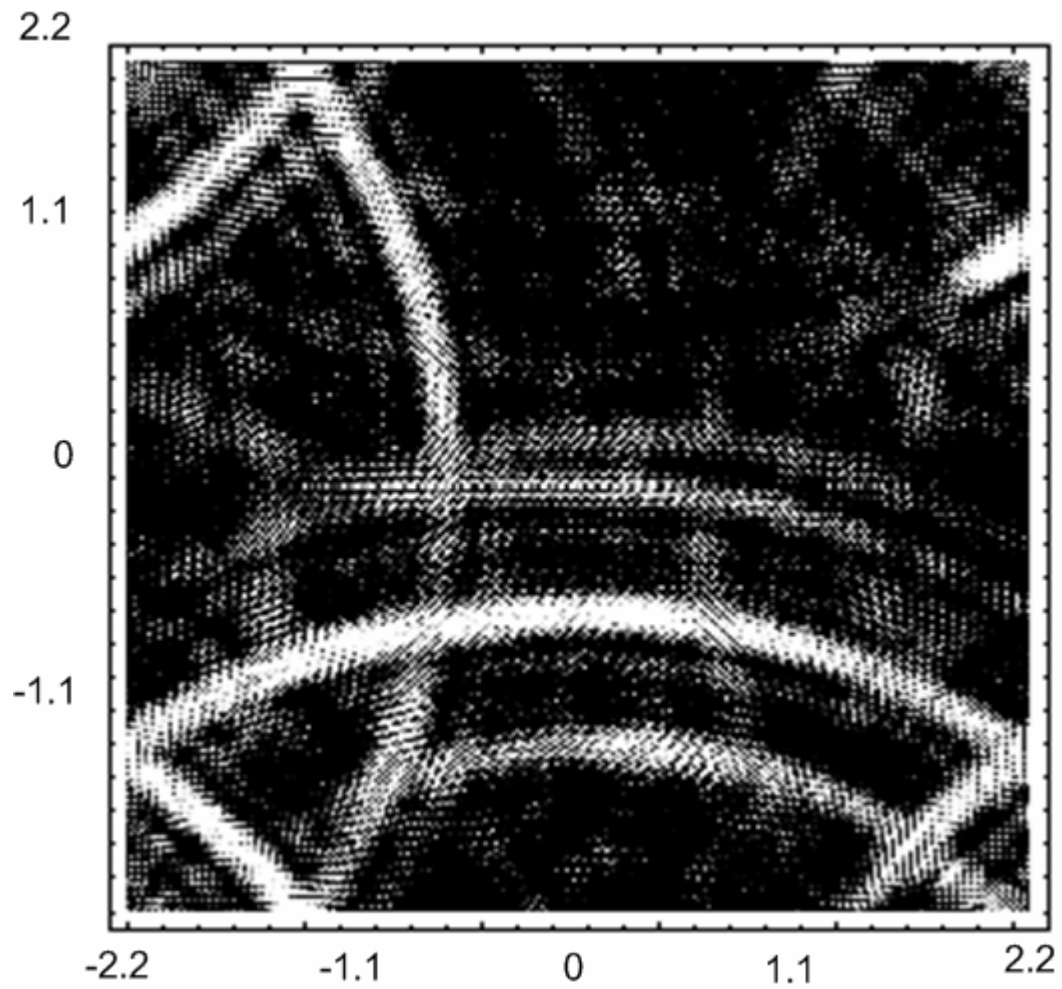


Figure 5.14 Generated ISAR Image of the Buried Target in Test Set 3 after Considering Resolutions 1-6 of the Frequency Domain Data (using db12)

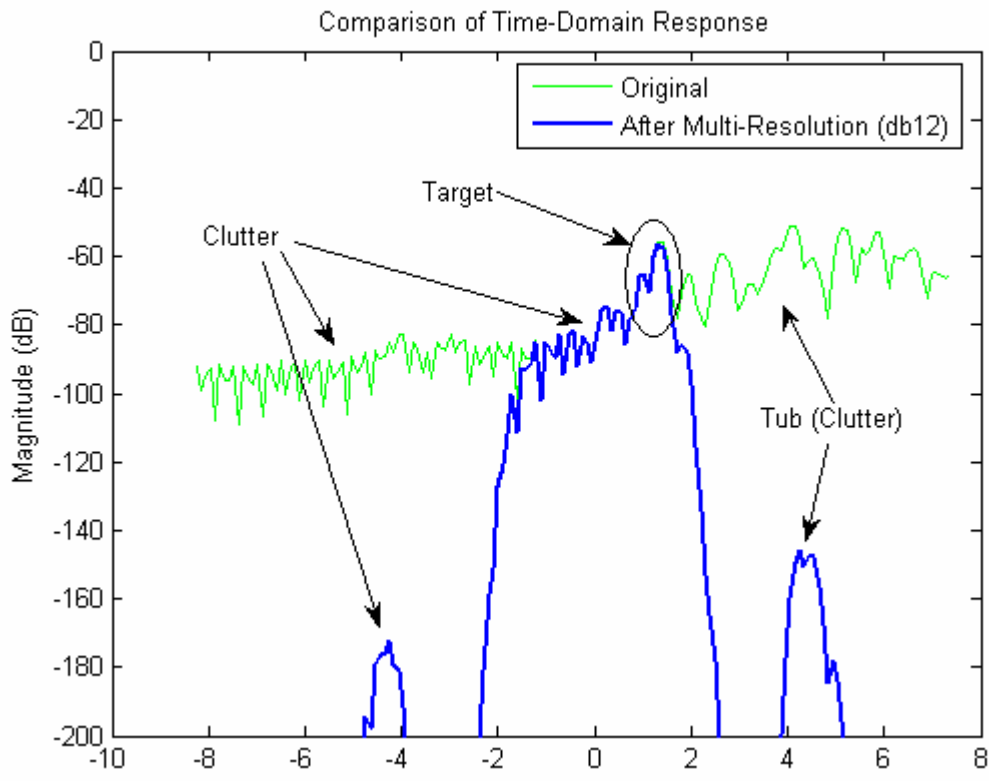


Figure 5.15 Time-Domain Response (azimuth of 50 degrees) for Test Set 3 after Considering Lower Resolutions (7-9) of Frequency Domain Data using db12

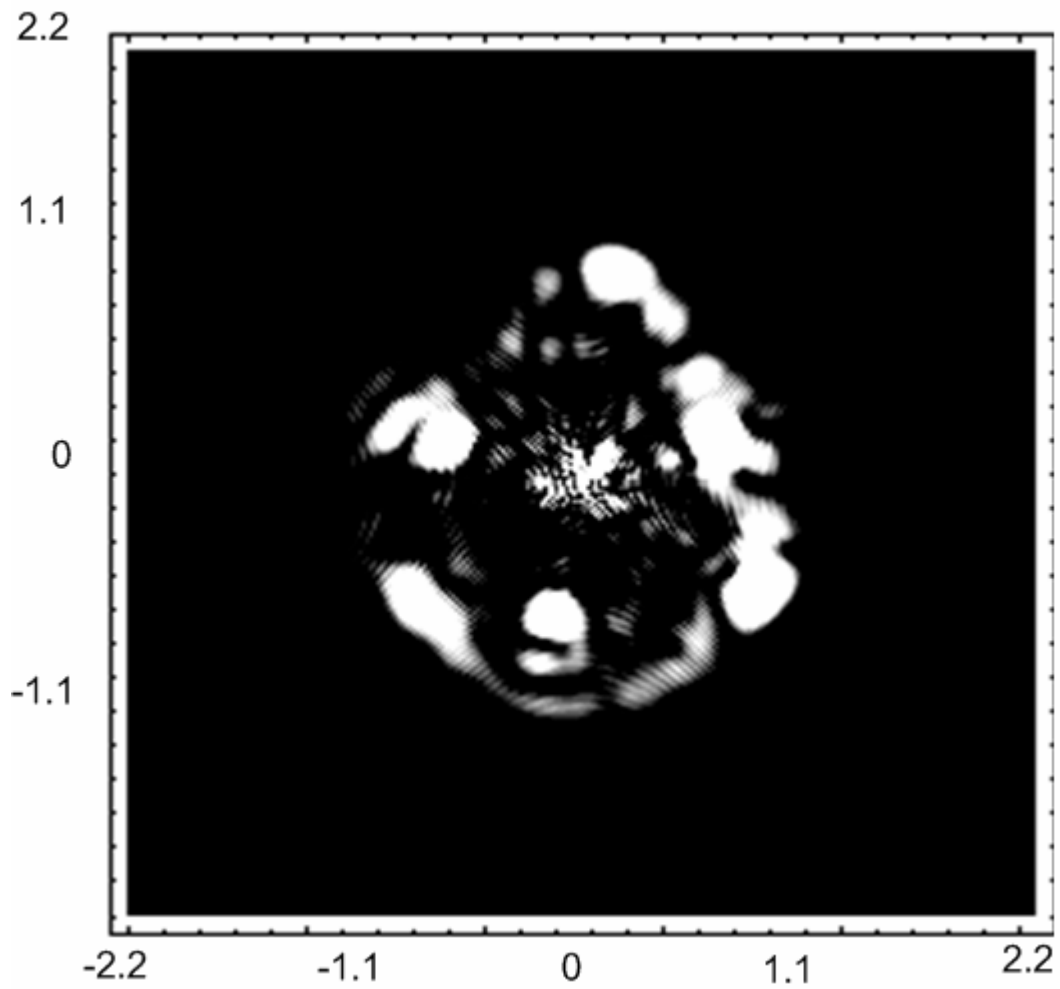


Figure 5.16 Generated ISAR Image of the Buried Target in Test Set 3 after Considering Resolutions 7-9 of the Frequency Domain Data (using db12)

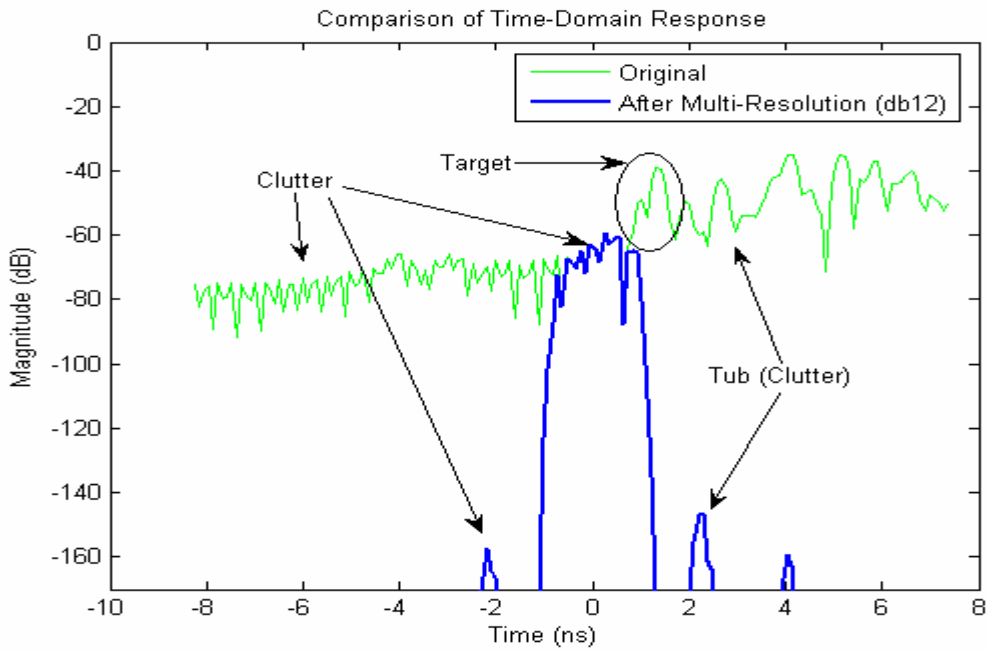


Figure 5.17 Time-Domain Response (azimuth of 50 degrees) for Test Set 3 after Considering Lower Resolutions (8-9) of Frequency Domain Data using db12

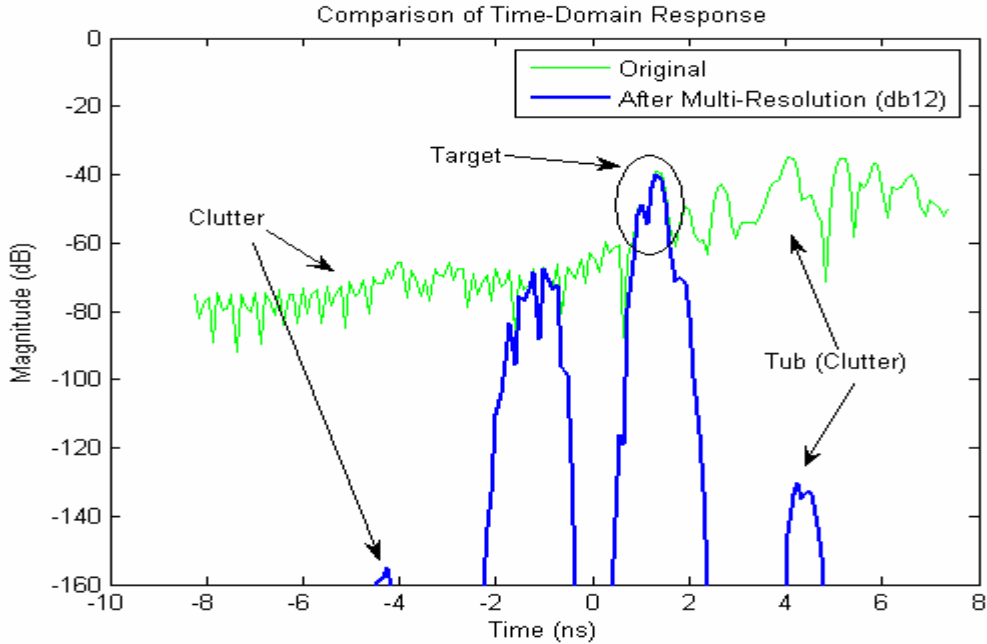


Figure 5.18 Time-Domain Response (azimuth of 50 degrees) for Test Set 3 after Considering Resolution 7 of the Frequency Domain Data using db12

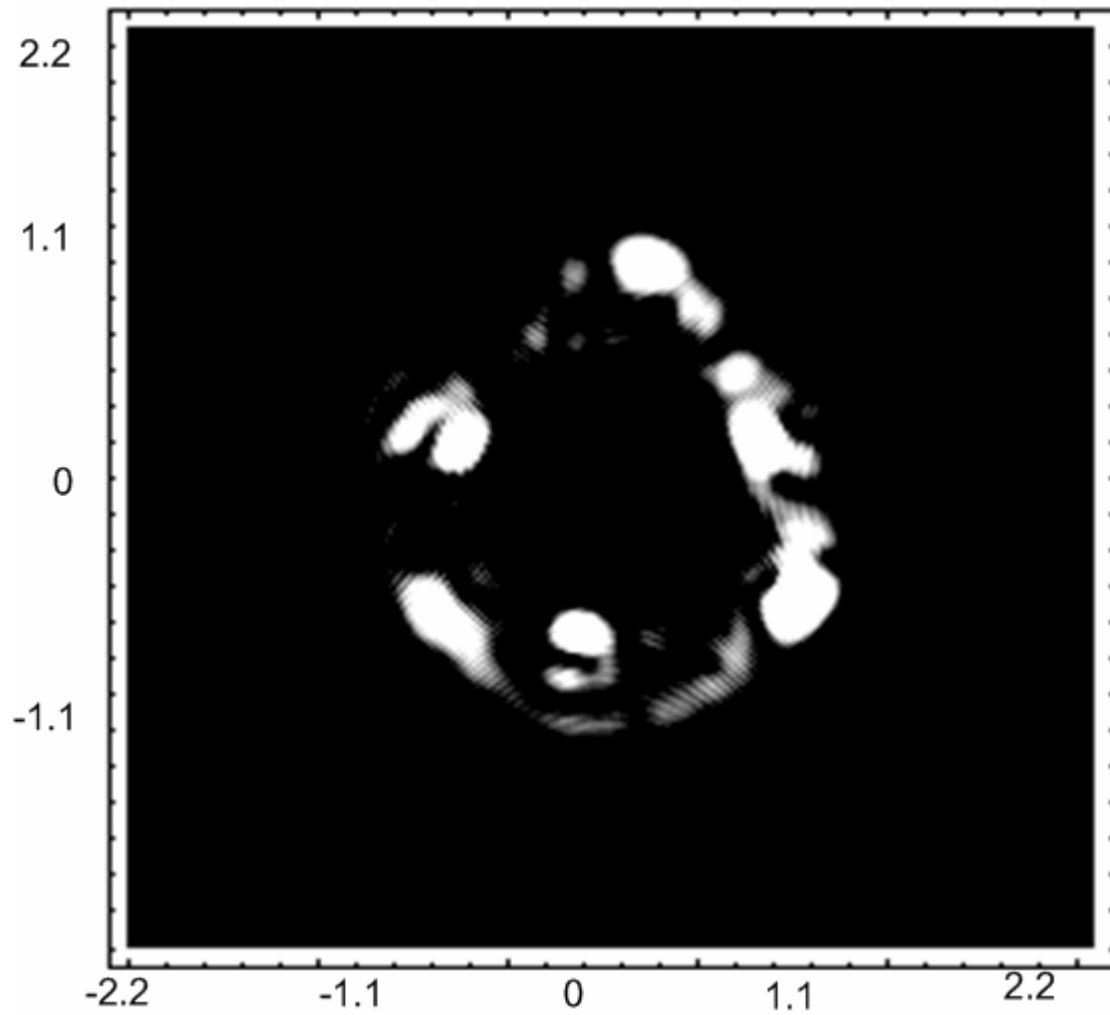


Figure 5.19 Generated ISAR Image of Buried Target in Test Set 3 after Considering Resolution 7 of Frequency Domain Data (using db12)

CHAPTER 6

CONCLUSIONS

ISAR imaging is being used in a wide range of applications. ISAR imaging assumes every return received at the receiver antenna to be a part of the target surface currents. This causes a lot of artifacts to appear in the generated ISAR images. These artifacts are produced due to the presence of many non-point interactions. This thesis was initiated with a motive to study the physics behind such interactions and resolve them to obtain better images. The fact that most of the non-point interactions are dispersive in nature where as the direct returns are discrete events in time opens door for the concept of time-frequency analysis which is introduced in chapter 2.

An experimental study has been implemented in this thesis to support the hypothesis that multi-resolution of the frequency domain data can be used to separate different interactions depending upon their arrival time. The system hardware, lab set up, data acquisition hardware and software was discussed in detail in chapter 3. The process of background subtraction, calibration and time gating was presented in chapter 3. To show the effect of multiple interactions in the presence of two or more targets, the setups as shown in figures 3.4-3.6 were used. Chapter 4 introduced the concept of ISAR imaging and results obtained by this algorithm were presented. It was seen in all the test cases that the effect of multiple interactions was very evident from the generated images. In section 4.2, the concept of multi-resolution using wavelets was introduced.

Figure 4.8 describes the meaning of different resolutions of the frequency domain data and its relation to the time domain gating. A detailed discussion on multi-resolution analysis was presented in section 4.2. Figures showing comparison of the time-domain data before and after multi-resolution analysis were presented for setup 1 and setup 2. Daubechies 2 (db2) wavelets were used to obtain multi-resolution. Figures 4.18, 4.19 for setup1 and 4.24, 4.25 for setup 2 showed how lower resolutions of the frequency domain data corresponded to early arrival times and hence the target information. Similarly figures 4.20, 4.21 for setup 1 and 4.25, 4.26 showed how higher resolutions of the frequency domain data corresponded to the clutter. The images obtained after selecting higher and lower resolutions were presented in Figures 4.22, 4.23 for setup 1 and Figures 4.29, 4.30 for setup 2 respectively. Thus it was concluded that different interactions can be separated using multi-resolution analysis.

The effect of the wavelet support size and the type of wavelets on the multi-resolution analysis and the effect of this length on clutter reduction capability were discussed in chapter 5. Results showed that increasing the filter length of the wavelet or in other words increasing the wavelet support size increased the clutter reduction capability of the wavelets. Daubechies wavelets and Coiflets with different support sizes were used to prove the above mentioned statement. The effect of different wavelets on the clutter reduction capability of the wavelets was presented in section 5.2. From Figures 5.9 and 5.10 it was concluded that Daubechies seemed to perform better as compared to Coiflets. Finally a test setup consisting of a complex target set was used to test the ability of multi-resolution analysis to separate different interactions in time and

there by improve the quality of generated images. Test set 3 consisted of three metal rods placed in a triangle shape and buried inside soil. Figure 5.11 showed how the magnitude of clutter and target were comparable to each other. The results of ISAR imaging on this target were presented. Figure 5.19 showed how multi-resolution was used to separate different clutters present and there by producing a much cleaner image of the target. Thus again these experimental results proved how the concept of multi-resolution can be used to separate different interactions in time.

Although the method presented in this thesis gave good results, it has many limitations. The lengths of different windows in time corresponding to different resolutions of the frequency domain data was presented in chapter 4 (refer Table 4.1). It can be seen that at high resolution can be achieved only at lower times. This is due to the dyadic nature of the wavelet resolutions. To obtain good resolution through out the entire time domain, wavelet packets can be used. On the other hand, the windows generated in time-domain can made to slide through the entire time period. This functionality may help in obtaining better results at all times. In chapter 5, it was concluded that Daubechies filters seemed to perform better than Coiflets (side lobe suppression and width of main lobe) for the same filter length. But a further investigation is need before generalizing this result. The effect of wavelet shape on the different targets can be studied in detail for making concrete suggestions. In this thesis a constant set of resolutions were used on the frequency domain data for all azimuths. Use of different resolutions for different azimuths might yield even better results

The next step in investigating the use of multi-resolution to separate different interactions can be extended to cases where non-metallic targets are used. Separating interactions in such cases where the signal to clutter ratio is very low will be more challenging.

APPENDIX A

MATLAB PRAGRAM FOR WAVELET PROCESSING

```
% % % % % % % % % % % WAVELET PROCESSING PROGRAM % % % % % %
```

```
% 1. THE DATA OBTAINED FROM THE NETWORK ANALYZER IS IN "*.dat"  
FORMAT, FOR  
% EXAMPLE 1.dat, 2.dat...72.dat.  
% 2. THIS DATA IS READ BY MATLAB FUNCTION "datread.m" AND THEN  
CONVERTED  
% INTO A 73X801 (COMPLEX) MATRIX.  
% 3. THIS DATA IS USED BY THIS MAIN MATLAB PROGRAM FOR  
PROCESSING LIKE BACK  
% GROUND SUBTRACTION, CALIBRATION AND WAVELET  
DECOMPOSITION. THIS DATA  
% TO BE INTERPOLATED(FOR ISAR IMAGING) IS THEN WRITTEN INTO THE  
COMPUTER  
% HARD DISK ("real.dat", "imag.dat").  
% THSES TWO FILES ARE THEN BY THE ISAR IMAGING PROGRAM  
(MATHEMATICA)  
% 4. MATHEMATICA PROGRAM ("generate_isar")THEN READS THIS DATA,  
DOES THE  
% INTERPOLATION AND THEN PRODUCES AN ISAR IMAGE OF THE  
TARGET.  
% % % % % % % % % % % % % % % % % % % % % % % % % % % % % %  
% % % % % % %
```

```
% DEFINING SOME CONSTANTS
```

```
fftsize= 2048;  
deg2ra= pi/180;  
rad2deg= 180/pi;  
c= 299792458; % speed of light
```

```
% INPUTS FROM USER
```

```
theta= input('ENTER THE VALUE OF ANTENNA ELEVATION, THETA ');  
freq_start= input('ENTER THE VALUE START FREQUENCY ');  
freq_stop= input('ENTER THE VALUE STOP FREQUENCY ');  
num_fsp= input('ENTER THE NUMBER OF FREQUENCY POINTS ');
```

```
% SOME CALCULATIONS FROM INPUTS
```

```
center_pt= (num_fsp+1)/2;
```

```

freq_inc= (freq_stop-freq_start)/(num_fsp-1);
time_range= 1/freq_inc;
time_inc= time_range/fftsize;

% READING DATA FROM THE HARD DISK WHICH IS IN ".dat" FORMAT
% "datread" IS A FUNCTION WHICH CONVERTS THE DATA FROM NETWORK
ANALYZER TO
% A FORMAT REQUIRED FOR THE PROGRAM

data= zeros(73,801);
[data,bgrnd]= datread();

% TAKING REAL AND IMAGINARY PARTS OF THE DATA AND
BACKGROUND

datare= real(data);
dataim= imag(data);
bgre= real(bgrnd);
bgim= imag(bgrnd);

% % % % % % % % % % % % % % BACK GROUND SUBTRACTION % % % % % %
% % % % % %

datare_sub= datare-bgre;
dataim_sub= dataim-bgim;
data_sub= complex(datare_sub,dataim_sub);

% NEXT STEP IS TO DO CALIBRATION OF THIS DATA. TO DO THIS,
THEORETICAL RCS
% OF SPHERE, MEASURED RCS OF SPHERE ARE REQUIRED FOR SAME
DIAMETER.
% THIS FILE('sp4th.dat') IS THE OUPUTPUT FILE OF A FORTRAN PROGRAM (BY
JERSAK)
% WHICH CALCULATES THE THEORETICAL RESPONSE OF THE SPHERE.

sp6th1= dlmread('sp6th1.dat');
sp6thre= sp6th1(:,1); % Making the dimension 1x801.

```

```

sp6thim= sp6th1(:,2);
sp6th= complex(sp6thre,sp6thim);

```

```

% THIS PART OF THE PROGRAM READS THE MEASURED RESPONSE OF
THE SPHERE

```

```

spbg1= dlmread('spbg.dat'); % Sphere Background
sp6_msrd= dlmread('sp6.dat'); % Measured for 6 inch
sp6msrd_sub_re= sp6_msrd(:,1)-spbg1(:,1)'; % PERFORM BCKGRND SUB ON
SPHERE
sp6msrd_sub_im= sp6_msrd(:,2)-spbg1(:,2)';
sp6msrd_sub= complex(sp6msrd_sub_re,sp6msrd_sub_im);

```

```

% % % % % % % % % % % % % % % CALIBRATION PROCESS % % % % % % % %

```

```

% CALIBRATED= (RAW -BCKGRND)*THEORETICAL SPHERE/(MSRD
SPHERE-BGRND SPHERE)

```

```

for index1= 1:72
    temp= data_sub(index1,:);
    calib_dat_abs= abs(temp).*(abs(sp6th)./abs(sp6msrd_sub));
    calib_dat_ang= angle(temp)+(angle(sp6th)-angle(sp6msrd_sub));
    calib_dat_re(index1,:)= calib_dat_abs.*cos(calib_dat_ang);
    calib_dat_im(index1,:)= calib_dat_abs.*sin(calib_dat_ang);
end;
calib_data= complex(calib_dat_re,calib_dat_im);

```

```

% ZERO PADDING OF THIS DATA TO MAKE THE SIZE EQUAL TO FFT SIZE
% ZERO PADDING INCREASES THE NUMBER OF DATA POINTS IN THE
TIME-DOMAIN DATA

```

```

num_zeros= fftsize-num_fsp;
zpcalib_data= zeros(72,fftsize);

```

```

zpcalib_data(:,1:(center_pt-1))= calib_data(:,center_pt:(num_fsp-1));
zpcalib_data(:,center_pt)= calib_data(:,num_fsp);
zpcalib_data(:,(center_pt+num_zeros+1):fftsize)= calib_data(:,1:(center_pt-1));

```

```

% TAKING THE REAL AND IMAGINARY PART OF THIS FREQUENCY
DOMAIN DATA TO BE
% USED FOR WAVELET PROCESSING

data_real= real(zpcalib_data);
data_imag= imag(zpcalib_data);

% WAVELET APPLICATION

% NUMBER OF RESOLUTIONS
resn_dpth= input('ENTER THE NUMBER OF RESOLUTIONS REQUIRED')

for index9= 1:72
    data_realwv(:, :, index9)= swt(data_real(index9,:), resn_dpth, 'db2');
    data_imagwv(:, :, index9)= swt(data_imag(index9,:), resn_dpth, 'db2');
end;

% MAKING SOME RESOLUTIONS ZERO.
% THESE RESOLUTIONS ARE FROM 1 TO RESOLUTIONDEPTH, HIGH TO
LOW LAST BEING
% THE APPROXIMATION COEFFICIENTS.

data_realwv(1, :, :)= zeros(fftsize, 72);
% data_realwv(2, :, :)= zeros(fftsize, 72);
% data_realwv(3, :, :)= zeros(fftsize, 72);
% data_realwv(4, :, :)= zeros(fftsize, 72);
% data_realwv(5, :, :)= zeros(fftsize, 72);
% data_realwv(6, :, :)= zeros(fftsize, 72);
% data_realwv(7, :, :)= zeros(fftsize, 72);
% data_realwv(8, :, :)= zeros(fftsize, 72);
% data_realwv(9, :, :)= zeros(fftsize, 72);

data_imagwv(1, :, :)= zeros(fftsize, 72);
% data_imagwv(2, :, :)= zeros(fftsize, 72);
% data_imagwv(3, :, :)= zeros(fftsize, 72);
% data_imagwv(4, :, :)= zeros(fftsize, 72);
% data_imagwv(5, :, :)= zeros(fftsize, 72);
% data_imagwv(6, :, :)= zeros(fftsize, 72);
% data_imagwv(7, :, :)= zeros(fftsize, 72);

```

```

% data_imagwv(8,,:) = zeros(fftsize,72);
% data_imagwv(9,,:) = zeros(fftsize,72);

% RECONSTRUCTION OF THE REAL AND IMAGINARY TIME GATED DATA
FROM THESE
% RESOLUTIONS
for index10= 1:72
    data_real1(index10,:)= iswt(data_realwv(:, :,index10),'db2');
    data_imag1(index10,:)= iswt(data_imagwv(:, :,index10),'db2');
end;

% PHASE WRAPPING AROUND 0 AND 360 DEGREES FOR REAL AND
IMAGINARY DATA

temp= data_real1(1,:);
data_real= [data_real1;temp];

temp= data_imag1(1,:);
data_imag= [data_imag1;temp];

% THIS DATA "data_real" and "data_imag" IS WRITTEN INTO THE HARD DISK
FOR
% FURTHER PROCESSING.

dlmwrite('real.dat',data_real);
dlmwrite('imag.dat',data_imag);

```


APPENDIX B

MATHEMATICA PROGRAM FOR ISAR IMAGING

PROGRAM TO GENERATE ISAR IMAGES

* CALLING PACKAGES NEEDED FOR THE PROGRAM*

Clear All;

Needs["LinearAlgebra`MatrixManipulation`"];

Needs["Statistics`DataManipulation`"];

Needs["Wavelets`Wavelets`"];

Needs["Graphics`Graphics`"];

Needs["Graphics`MultipleListPlot`"];

(* DEFINING SOME CONSTANTS WHICH WILL BE USED IN THE PROGRAM*)

Clear All;

c=299792458;

theta=45*Pi/180;

freqStart=4*10^9;

freqStop=8*10^9;

numPhiPts=72;

numFreqPts=801;

freqInc=(freqStop-freqStart)/(numFreqPts-1);

phiInc=2*Pi/numPhiPts;

SetDirectory["E:\\Anil\\Thesis\\Wavelets\\sphere-roc\\mar05_2sps\\"];

resubDat=Import["real.dat","CSV"];

imsubDat=Import["imag.dat","CSV"];

(***** K- SPACE INTERPOLATION *****)

Clear All;

reDatApprox= ListInterpolation[resubDat,{{0.0,360},{freqStart,freqStop}}];

imDatApprox= ListInterpolation[imsubDat,{{0.0,360},{freqStart,freqStop}}];

kConst= N[2*Pi*Sin[theta]/c];

kmin= kConst*freqStart;

kmax= kConst*freqStop;

If[kmin>kmax,Print["STOP! kmin is greater than kmax"]];

nk= Floor[N[numFreqPts*Cos[Pi/4.0]]];

dk= 1.0;

rad2deg= 180.0/Pi;

(* IF THE INTERPOLATED DATA IS OUT OF RANGE i.e LESS THAN KMIN OR GREATER THAN KMAX THEN THIS INTERPOLATED DATA IS SET TO ZERO. cxDatTable GENERATES A TABLE OF INTERPOLATED VALUES BY VARYING KX,KY IN A LINEAR RANGE FROM -Kmax TO Kmax. THE PHI AND FREQ CORRESPONDING TO EACH VALUE OF Kx AND Ky IS CALCULATED AND THEN DATA IS INTERPOLATED TO THIS VALUE OF PHI AND FREQ *)

```

cxDatTable= Table[
  If[Sqrt[kx^2+ky^2]>kmin,
    If[Sqrt[kx^2+ky^2]<kmax,
      Which[
        kx<0.0,
          (phipt= 180.0+ArcTan[ky/kx]*rad2deg; freqpt= Sqrt[kx^2+ky^2]/kConst;
            reDatApprox[phipt,freqpt]+I*imDatApprox[phipt,freqpt]),
        kx>0.0&&ky>0.0,(phipt= ArcTan[ky/kx]*rad2deg;
freqpt= Sqrt[kx^2+ky^2]/kConst;
          reDatApprox[phipt,freqpt]+I*imDatApprox[phipt,freqpt]),
        kx>0.0&&ky<0.0,(phipt= 360.0+ArcTan[ky/kx]*rad2deg;
freqpt= Sqrt[kx^2+ky^2]/kConst;
          reDatApprox[phipt,freqpt]+I*imDatApprox[phipt,freqpt])],
    Complex[0.0,0.0]],
  Complex[0.0,0.0]],
  {ky,-kmax,kmax,dk},{kx,-kmax,kmax,dk}];

```

```
ListDensityPlot[Abs[cxDatTable],Mesh False];
```

(*MAIN ISAR PROGRAM *)

(* SELECTING THE DIMENSIONS OF THE FINAL IMAGE. THE IMAGE IS UPSCALED BY ZERO-PADDING THE INTERPOLATED DATA *)

```

Clear All;
nlo= Dimensions[cxDatTable][[1]];
imageDim= 256;
nZero= Floor[(imageDim-nlo)*0.5] ;

n1= nZero*2+nlo;
patch1= Table[Complex[0.,0.],{i,1,nZero},{j,1,nlo}];
patch2= Table[Complex[0.,0.],{i,1,n1},{j,1,nZero}];

```

```

tempM1= AppendColumns[patch1,cxDatTable];
tempM2= AppendColumns[tempM1,patch1];
tempM3= AppendRows[patch2,tempM2];
pData2D= AppendRows[tempM3,patch2]; (* INTERPOLATED DATA WITH ZERO
PADDING *)

```

```

(* REARRANGING DATA FOR IFFT. THIS IS SIMILAR TO IFFTSHIFT
FUNCTION IN MATLAB. THIS IS DONE TO ARRANGE DATA FROM 0-2Pi
FORMAT WHICH IS USED IN COMPUTATION AS OPPOSED TO -Pi - Pi
FORMAT*)

```

```

Dimensions[zpData2D];
half= Floor[(n1-1)/2.0];
halfPlusOne= half +1;
sub1 = TakeColumns[Take[zpData2D,-halfPlusOne],-halfPlusOne];
sub2 = TakeColumns[Take[zpData2D,-halfPlusOne],half];
sub3 = TakeColumns[Take[zpData2D,half],half];
sub4 = TakeColumns[Take[zpData2D,half],-halfPlusOne];
subColumn1 = AppendColumns[sub1, sub4];
subColumn2 = AppendColumns[sub2, sub3];
zpMusicImage= AppendRows[subColumn1,subColumn2];

```

```

(* TAKE THE IFFT OF THIS RE-ARRANGED DATA AND THEN ARRANGE IT
BACK TO THE PREVIOUS FORMAT*)

```

```

objectImage=InverseFourier[zpMusicImage];
(* rearrange the positions of DFT results *)
sub1 = TakeColumns[Take[objectImage,halfPlusOne],halfPlusOne];
sub2 = TakeColumns[Take[objectImage,halfPlusOne],-half];
sub3 = TakeColumns[Take[objectImage,-half],-half];
sub4 = TakeColumns[Take[objectImage,-half],halfPlusOne];
subColumn1 = AppendColumns[sub4, sub1];
subColumn2 = AppendColumns[sub3, sub2];
objectImage = AppendRows[subColumn2, subColumn1];
ListDensityPlot[10.*Log[10,Abs[objectImage]],Mesh False]

```

REFERENCES

- [1] Ruck, G.T., D.E. Barrick and W.D. Stuart, *Radar Cross Section Handbook, Vol.1*, edited by G.T. Ruck, Plenum Press, New York, 1970.
- [2] Stratton, J.A. and C.J. Chu, "Diffraction theory of electromagnetic waves," *Physical Review*, Vol.56, pp. 99-107, July 1939.
- [3] Lewis, R.M., "Physical optics inverse diffraction," *IEEE Trans. On Antennas and Propagation*, Vol. AP-17, No.3, pp.308-314, May 1969.
- [4] Bennett, C.L., "Time domain inverse scattering," *IEEE Trans. On Antennas and Propagation*, Vol. AP-, No.3, pp.213-219, March 1981.
- [5] Mittra, R., "Integral equation methods for transient scattering," Chapter 2 in *Transient Electromagnetic Fields*, edited by L.B. Felsen, Springer-Verlag, New York, NY, 1980.
- [6] Bojarski, N.N., "A survey of the physical optics inverse scattering identity", *IEEE Trans. On Antennas and Propagation*, Vol. AP-30, No. 5, pp. 980-989, September 1982.
- [7] Shen Yuhshyen, "Dynamic Microwave Imaging", PhD Dissertation, University of Pennsylvania, Philadelphia, 1987.
- [8] H.J. Li, "Microwave image understanding and its application to application to Radar cross section management ", Ph.D. Dissertation, University of Pennsylvania, Philadelphia, 1987.

- [9] Jersak, .D. “Time Domain Analysis of Measured Frequency Domain Radar Cross-Section Data,” Masters Thesis, *University of Texas at Arlington*, 1988.
- [10] Jersak, .D. “Bistatic Fully Polarimetric Radar Cross-Section Calibration Techniques and Measurement Error Analysis,” PhD Dissertation, *University of Texas at Arlington*, 1993.
- [11] A. Achim¹, A. Bezerianos¹ and P. Tsakalides, “SAR image de-noising: a multi-scale robust statistical approach”, Proc.14th Int'l Conf. Digital Sig. Proc (DSP 2002) II (2002), 1235{1238).
- [12] Victor C Chen, Hao Ling, *Time-Frequency Transforms for radar imaging and signal analysis*, Artech House Inc.2002.
- [13] Mensa D.L, *High Resolution Radar Cross Section Imaging*, Artech House, Boston, London.
- [14] Roger J. Sullivan, *Radar Foundations for Imaging and Advanced Concepts*, SciTech Publishing,Inc.
- [15] Stephen Mallat, *A Wavelet Tour of Signal Processing*, Academic Press 1999.
- [16] Ingrid Daubechies, *Ten Lectures on Wavelets*, SIAM, Philadelphia 1992.
- [17] Gilbert Strang and Truong Nguyen, *Wavelets and Filter Banks*, Wellesley-Cambridge Press,Wellesley MA,1996.
- [18] Dolaty, .M. “Inverse Synthetic Aperture Radar Imaging Techniques,” Masters Thesis, *University of Texas at Arlington*, 1989.

[19] Martin Vetterli and Jelena Kovacevic, *Wavelets and Subband Coding*, Prentice Hall PTR, Englewood Cliffs NJ, 1995.

[20] A.N. Akansu and R.A. Haddad, *Multiresolution Signal Decomposition Transforms, Subbands, Wavelets*, Academic Press, NY, 1994

[21] A. Abbate, C.M. DeCusatis and P.K. Das, *Wavelets and Subbands Fundamentals and Applications*, Birkhauser, Boston, 2002.

BIOGRAPHICAL INFORMATION

Anil Kumar Kollipara was born in Andhra Pradesh, India in 1981. He completed his Bachelor of Engineering in Electronics from Mumbai University, India in May 2002 and is currently pursuing Masters in Electrical Engineering from The University of Texas at Arlington. He has been working as a Graduate Research Assistant at the Wave Scattering Research Center, UTA since August 2003. He also has been a Graduate Teaching Assistant for various undergraduate level courses. His current research interests are in the areas Signal Processing, Radar Imaging and Wireless Communications.